

Thesis for the Degree

of Doctor

Production of Υ and χ_c in $d + Au$ and

$p + p$ collisions at $\sqrt{s_{NN}} = 200$ GeV

by

Kwangbok Lee

Department of Physics

Graduate School

Korea University

December 2010

洪炳軾 教授指導
博士學位論文

**Production of Υ and χ_c in $d + Au$ and
 $p+p$ collisions at $\sqrt{s_{NN}} = 200$ GeV**

이 論文을 理學 博士學位 論文으로 提出함

2010年 12月 8日

高麗大學校大學院
物理學科
李光馥

李光馥의 博士學位論文 審查를 完了함

2010年 12月 8日

委員長 홍 병식 (印)

委員 심 광숙 (印)

委員 윤 진희 (印)

委員 강 주석 (印)

委員 李 政 日 (印)

Abstract

This thesis includes data reconstruction and simulation to measure $\Upsilon \rightarrow \mu^+ + \mu^-$ at forward and backward rapidities with the Muon arms, which cover rapidity, $|y| \in [1.2, 2.2]$. The physical backgrounds of Drell Yan, correlated open bottom, and correlated open charm are estimated and full simulations are done. So σ_{Υ}/dy and R_{dAu}^{Υ} from the Run6 pp dataset and Run8 dAu dataset are extracted. Comparisons with theoretical predictions for the σ_{Υ}/dy are also shown. And $\chi_c \rightarrow \mu^+ + \mu^- + \gamma$ at forward and backward rapidities is simulated and reconstructed with the Muon arms and Muon Piston Calorimeters(MPCs), which cover rapidity, $|y| \in [3.1, 3.8]$. σ_{χ_c}/dy and R_{χ_c} from the Run8 pp dataset and Run8 dAu dataset are surveyed.

Contents

1	Introduction	1
1.1	Motivation	1
1.2	Collision geometry and nuclear modification factor	3
1.2.1	Collision geometry	3
1.2.2	Nuclear Modification Factor	4
1.3	Phenomena of nuclear collisions	5
1.3.1	Color screening	5
1.3.2	Jet quenching	6
1.3.3	Elliptic flow	7
1.3.4	Charmonium suppression	10
1.4	Cold Nuclear Matter effect and quarkonia measurement	14
1.4.1	Nuclear Shadowing	14
1.4.2	Nuclear absorption cross section	14
1.4.3	Cronin effect	18
1.5	Quarkonia system	18
1.6	Quarkonia measurement as probes of production mechanism	21
1.7	Υ and χ_c measurement from another experiments	22
2	Experimental Setup	25
2.1	RHIC and PHENIX detector	25
2.1.1	LINAC	25
2.1.2	Booster	25
2.1.3	AGS	25

2.1.4	RHIC	26
2.1.5	PHENIX	27
2.2	PHENIX Central Arm	27
2.3	PHENIX Muon arms	28
2.3.1	The muon tracker detector	28
2.3.2	The muon identifier detector	29
2.4	Global Detectors	32
2.5	PHENIX MPCs	34
2.5.1	General	34
2.5.2	MPC cell	34
3	Data Analysis 1 - Υ measurement at $p + p$ and $d + \text{Au}$ Collisions	37
3.1	Data set, Quality Assurance Good Run list	37
3.1.1	Quality Assurance, Good Runlist and Data Set	37
3.1.2	Cut conditions	38
3.2	Data Analysis	39
3.2.1	Analysis code and output	39
3.2.2	Combinatorial background subtraction	39
3.2.3	Residual background estimation	42
3.3	Υ simulation	44
3.3.1	Simulation setup and procedure	44
3.3.2	Υ mass resolution	46
3.3.3	Composition of Υ family	46
3.4	Acceptance \times efficiency calculation	50
3.4.1	Run6pp Acceptance \times efficiency calculation	50
3.4.2	Run8dAu Acceptance \times efficiency calculation	51
3.5	Drell Yan, Open Bottom and Open Charm estimation	54
3.5.1	Drell Yan estimation	54
3.5.2	Open bottom estimation	55
3.5.3	Open Charm estimation	60
3.6	Fitting real data	61

3.6.1	Fitting parameters and options	61
3.6.2	Fitting Run6pp and Run8dAu	63
3.7	Systematic uncertainties	66
3.7.1	Fitting Function	66
3.7.2	MUID, MUTR, BBC, Acceptance \times Efficiency.	67
3.7.3	Summary of the systematic uncertainties	68
3.8	Results	70
3.8.1	Invariant yield and cross section	70
3.8.2	Nuclear modification factor	73
3.9	Updates with NLO Drell Yan calculation	75
3.9.1	NLO Drell Yan calculation	75
3.9.2	Updated result	75
4	Data Analysis 2 - χ_c measurement at $p + p$ and $d + \text{Au}$ Collisions	78
4.1	Data set, Quality Assurance Good Run list	78
4.1.1	Quality Assurance, Good Runlist and Data Set	78
4.1.2	Cut conditions	79
4.1.3	MPC ϕ angle distribution	79
4.2	Data Analysis	83
4.2.1	Analysis code and output	83
4.3	χ_c simulation	87
4.3.1	Single χ_c simulation	87
4.3.2	Embedded χ_c simulation	91
4.3.3	Kinematic Cut Study	100
4.4	Fitting real data	103
4.4.1	Fitting parameters and options	103
4.4.2	Fitting Run6pp and Run8dAu	103
4.5	Systematic uncertainties	106
4.5.1	determining of the Normalization	106
4.5.2	Embedding efficiency	106
4.5.3	MPC photon energy cut	106

4.5.4	Fitting Function	109
4.5.5	MUID, MUTR, BBC, Acceptance \times Efficiency.	114
4.6	Summary of the systematic uncertainties	114
4.7	Results	116
4.7.1	Invariant yield and cross section	116
5	Conclusions	119
A	Run8dAu QA	125
A.1	QA table	125

List of Figures

1.1	Entropy density	2
1.2	Schematic phase diagram of QCD matter	2
1.3	A cartoon of centrality	3
1.4	A cartoon of collision	4
1.5	Comparision of nucleon and nuclear collision	6
1.6	Nuclear modification of π^0	7
1.7	Particle correlation	8
1.8	Almond shape of created matter	9
1.9	v_2 measurements of PHENIX and STAR	9
1.10	v_2/n of PHENIX and STAR	10
1.11	J/ψ v_2 measurement at PHENIX	11
1.12	J/ψ suppression	13
1.13	Gluon modification factor vs. momentum fraction	15
1.14	Nuclear partion distribution functions	15
1.15	PHENIX J/ψ R_{dAu}	16
1.16	PHENIX J/ψ R_{CuCu}	17
1.17	PHENIX J/ψ R_{dAu}	17
1.18	PHENIX J/ψ R_{cp}	18
1.19	Charmonium map	19
1.20	Bottomonium map	20
1.21	Quarkonia spectra	21
1.22	Υ cross section vs. beam energy	23
1.23	Υ cross section of Star $d + Au$ collision	23

1.24	R_{chi_c} of various beam energy	24
1.25	Υ R_{AuAu} in PHENIX	24
2.1	Experiments at RHIC	26
2.2	View of PHENIX detectors	27
2.3	Drawing of PHENIX Muon arm	29
2.4	MuTR stations	30
2.5	Locations of absorbers and active layers of the Muon Arm	31
2.6	Iarocci tubes	32
2.7	Schematic view of a MuID layer	33
2.8	View of MPCs	34
2.9	MPC Tower Assembly	35
2.10	MPC crystal	35
3.1	Likesign event over scaled mixed event	40
3.2	Invariant mass distribution by likesign subtraction	41
3.3	Invariant mass distribution by scaled mixed event subtraction	43
3.4	Simulated three states of Υ	47
3.5	Simulated Υ_{Family}	48
3.6	Generated Υ	50
3.7	Acceptance \times Efficiency of Υ	51
3.8	Generated Drell Yan	55
3.9	Reconstructed Drell Yan	56
3.10	Reconstructed bottom correlation	58
3.11	p_T distribution of bottom	59
3.12	Uncorrelated bottom	59
3.13	Reconstructed charm correlation	60
3.14	Υ fitting of Run6pp	63
3.15	Υ fitting of Run8dAu	64
3.16	Comparision of Υ cross sections	72
3.17	Υ cross sections vs. rapidity	73
3.18	R_{dAu}^{Υ} with Run8dAu/Run6pp	74

3.19	NLO Drell Yan calculations	75
3.20	Υ fitting with NLO calculation	76
3.21	R_{dAu}^{Υ} with Run8dAu/Run6pp	77
4.1	χ_c ϕ distribution and MPC hit distribution of single χ_c	81
4.2	χ_c ϕ distribution and MPC hit distribution of embedded χ_c	82
4.3	χ_c invariant mass of Run8pp North	84
4.4	χ_c invariant mass of Run8pp South	85
4.5	χ_c invariant mass of Run8dAu North	86
4.6	The decay J/ψ of generated χ_{c1}	89
4.7	The decay γ of generated χ_{c1}	89
4.8	The decay J/ψ of generated χ_{c2}	90
4.9	The decay γ of generated χ_{c2}	90
4.10	The energy distribution of χ_{c1} decay γ	91
4.11	The energy distribution of χ_{c2} decay γ	92
4.12	The reconstructed mass difference between χ_{c1} and J/ψ by single simulation of Run8pp	92
4.13	The reconstructed mass difference between χ_{c2} and J/ψ by single simulation of Run8pp	93
4.14	The reconstructed mass difference between χ_{c1} and J/ψ by single simulation of Run8dAu	94
4.15	The reconstructed mass difference between χ_{c2} and J/ψ by single simulation of Run8dAu	95
4.16	The reconstructed mass difference between χ_{c1} and J/ψ by embedding simulation of Run8pp	96
4.17	The reconstructed mass difference between χ_{c2} and J/ψ by embedding simulation of Run8pp	97
4.18	The reconstructed mass difference between χ_{c1} and J/ψ by embedding simulation of Run8dAu	98
4.19	The reconstructed mass difference between χ_{c2} and J/ψ by embedding simulation of Run8dAu	99
4.20	MPC photon energy vs. angle of J/ψ and photon of χ_c	101
4.21	MPC photon energy vs. rapidity of J/ψ	102
4.22	χ_c fitting of Run8pp data	104

4.23	χ_c fitting of Run8dAu data	105
4.24	$\text{BR} \times \chi_c$ cross section of Run8pp	118

List of Tables

1.1	χ_c and J/ψ	20
1.2	Quarkonia properties	21
2.1	Characters of MPC crystal	36
3.1	Number of MB events and Luminosity	38
3.2	Cut conditions for Run6pp and Run8dAu	38
3.3	Simulation parameters for Υ generation	45
3.4	Simulated Υ mass resolution	46
3.5	Composition of Υ family	48
3.6	Run6pp Acceptance \times Efficiency	52
3.7	Run8dAu Acceptnace \times Efficiency	53
3.8	Simulation parameter for Drell Yan	54
3.9	Simulation parameter for bottom	57
3.10	Fitting parameters for real data Υ	62
3.11	Integral of each component of Run6pp	64
3.12	Integral of each component of Run8dAu	65
3.13	Systematic uncertainties from Υ mass resolutions	66
3.14	Systematic uncertainties from Drell Yan	67
3.15	Systematic uncertainties from open bottom	68
3.16	Total statistical and systematic uncertainty of Υ	69
3.17	Υ invariant yield and cross section	70
3.18	Branching ratio of Υ	71
3.19	Υ cross section	71

3.20 Υ cross section and R_{dAu} comparison of preliminary and updated result	76
4.1 BBC MB Event and Luminosity	79
4.2 Cut conditions of Muon arm	79
4.3 Cut conditions of MPC	80
4.4 Simulation parameters for χ_c generation	88
4.5 Acceptance \times Efficiency of χ_{c1}	100
4.6 Acceptance \times Efficiency values of χ_{c2}	100
4.7 Fitting parameters of χ_c	103
4.8 Systematic uncertainties from Normalization method	106
4.9 Systematic uncertainties from Normalization mass window	107
4.10 Systematic uncertainties from χ_c photon cut level of Run8pp North arm .	107
4.11 Systematic uncertainties from χ_c photon cut level of Run8pp South arm .	108
4.12 Systematic uncertainties from χ_c photon cut level of Run8dAu North arm	108
4.13 Systematic uncertainties from χ_c peak width of Run8pp North arm	109
4.14 Systematic uncertainties from χ_c peak width of Run8pp South arm	110
4.15 Systematic uncertainties from χ_c peak width of Run8dAu North arm	110
4.16 Systematic uncertainties from χ_c ratio of Run8pp North arm	111
4.17 Systematic uncertainties from χ_c ratio of Run8pp South arm	112
4.18 Systematic uncertainties from χ_c ratio of Run8dAu North arm	113
4.19 Systematic uncertainties from MPC geometrical acceptance	113
4.20 Total statistical and systematic uncertainty of χ_c	115
4.21 χ_c decay J/ψ invariant yield	116
4.22 $\chi_c \rightarrow \mu^+ \mu^- \gamma$ branching ratios	117
4.23 Extrapolated χ_c cross section	117
A.1 QA of Run8dAu Part 1	126
A.2 QA of Run8dAu Part 2	127

Chapter 1

Introduction

1.1 Motivation

According to lattice QCD calculations [1], when heavy ion reaches sufficiently high energy densities it should undergo a phase transition to a plasma of deconfined quarks and gluons which is called Quark-Gluon Plasma (QGP). And they predict that the phase transition to the QGP state occurs at a critical temperature, T_c , of $150 - 200$ MeV. Figure 1.1 shows the calculated results of the entropy density s/T^3 as a function of temperature T . The entropy density increases in stepwise at $T_c \sim 200$ MeV due to the increase of the degree of freedom by deconfinement. A schematic phase diagram of hadronic matter including QGP is shown in Figure 1.2. The horizontal axis is the baryon density normalized to the density of the normal nuclear matter (~ 0.15 GeV/fm 3) and the vertical axis is the temperature. QGP is also considered to have existed in high temperature circumstances of the early universe, a few micro second after the Big Bang.

The main goal of the Relativistic Heavy Ion Collider (RHIC) is to create, identify, and study the QGP. The RHIC at Brookhaven National Laboratory (BNL) is the first colliding-type accelerator which can collide heavy nuclei up to gold (^{197}Au) at the center of mass energy per nucleon pair of $\sqrt{s_{NN}} = 200$ GeV and started its operation in 2000. The energy density achieved by the collisions at RHIC is expected to be well above the critical temperature. Considerable efforts are currently being invested in the study of high-energy heavy-ion collisions to reveal the existence of this phase transition and to study the properties of the new phase [27]. Besides the nuclear matter, RHIC has collided deuteron beam and gold beam ($d + \text{Au}$) to study the property of the cold nuclear matter. When the deuteron beam and gold beam collide, they are expected to create no hot and no dense medium. So the matter, that is created in $d + \text{Au}$ collision, is called cold nuclear matter(CNM). The CNM is an interesting matter itself and also can provide the quantitative comparison to the measurement of $A + A$ collision to provide a better understanding of the effects beyond CNM from hot and dense nuclear matter.

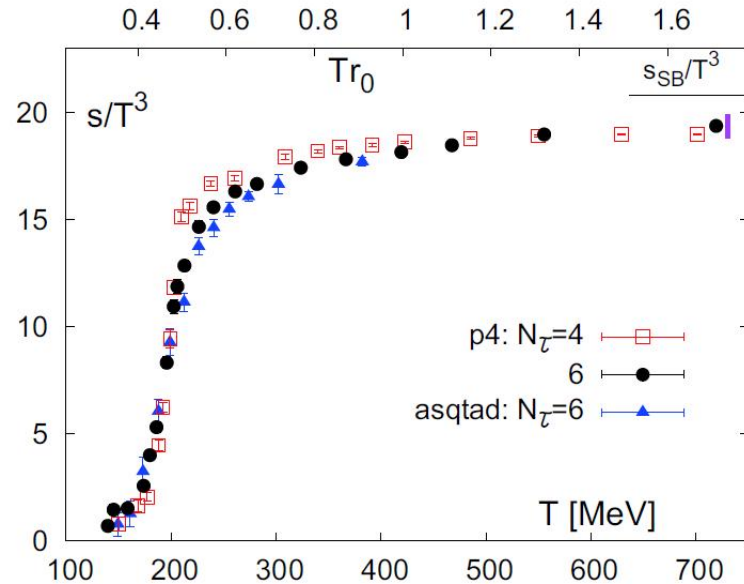


Figure 1.1: The entropy density ($s = \varepsilon + p$) in units of T^3 as a function of T calculated with lattice QCD [2].

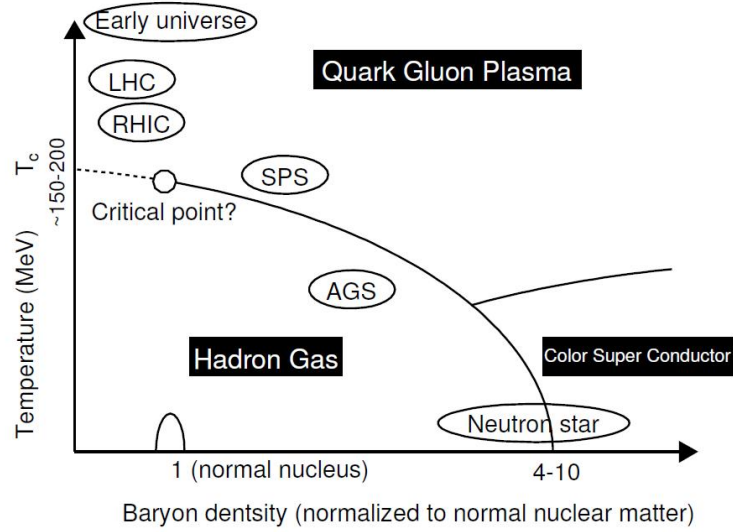


Figure 1.2: A schematic phase diagram of QCD matter.

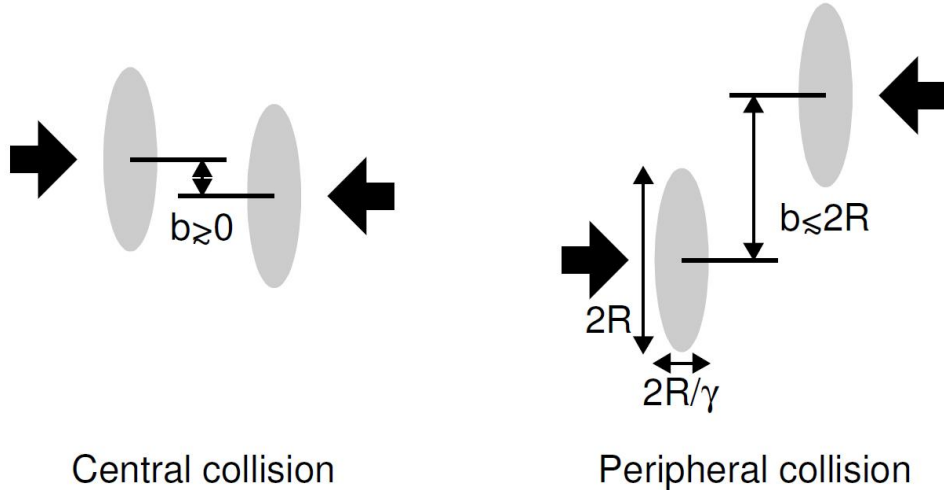


Figure 1.3: A cartoon of central (left) and peripheral (right) collisions.

1.2 Collision geometry and nuclear modification factor

1.2.1 Collision geometry

The geometric aspects of high-energy heavy-ion collisions play an important role in collision dynamics. Since the de Broglie wavelength of the nucleons in high-energy heavy nucleus-nucleus collision is much smaller than the size of the nucleus, the collision is described by the impact parameter, b , of the colliding nuclei. Figure 1.3 illustrates a central collision and a peripheral collision of nuclei with radii of R . As illustrated in Figure 1.4, the nucleons in high-energy heavy-ion collisions are classified into two groups, the participants and the spectators. The impact parameter b determines the sizes of participants and spectators. Since the spectators keep those longitudinal momenta and emerge at nearly zero degrees in the collision, it is easy to experimentally separate the spectators and the participants. Information about the impact parameter b is obtained by measuring the sizes of the spectators and/or the participants. The relation among impact parameter (b), the number of binary nucleon-nucleon collisions (N_{coll}) and the number of participants (N_{part}) can be evaluated using the Glauber model [3]. The Glauber model describes the heavy-ion collisions based on the participant-spectator model, the nuclear density distribution and the interaction between constituent nucleons. The total inelastic cross section of collisions of a nucleus A and a nucleus B is calculated from the nucleon-nucleon inelastic cross section, σ times the numbers of nucleons in the nucleus A and the nucleus B (Equation 1.1).

$$\sigma_{AB} = \sigma \times A \times B, \quad (1.1)$$

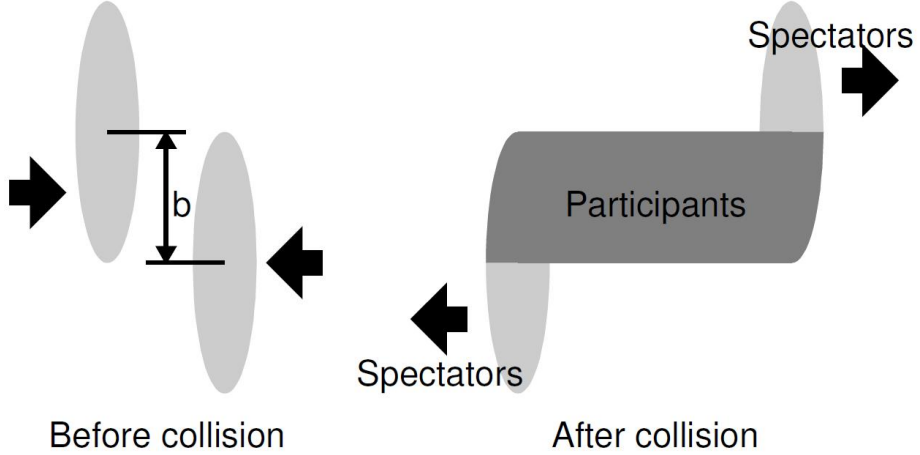


Figure 1.4: A cartoon of before and after a collision of nuclei.

The nucleons in each colliding nucleus are assumed to be distributed according to the Woods-Saxon distribution,

$$\rho(r) = \frac{\rho_0}{1 + \exp(\frac{r-R}{d})}, \quad (1.2)$$

where ρ_0 stands for the normal nuclear density, R is the radius and d is the diffuseness parameter.

1.2.2 Nuclear Modification Factor

Suppression or enhancement of nuclear collision comparing to $p + p$ collision can be parameterized by nuclear modification factors of R_{AA} , R_{CP} . R_{AA} is defined as

$$R_{AA}^i = \frac{dN_{AA}^i/dy_i \langle N_{coll}^{AA} \rangle}{dN_{pp}^i/dy_i \langle N_{coll}^{pp} \rangle}, \quad (1.3)$$

i stands for the kind of quarkonia or meson, dN_{AA}^i is the invariant yield of the particle, i and dy_i means rapidity or p_T bin. $\langle N_{coll}^{AA} \rangle$ is the number of binary collision of the nuclear collision system which is calculated by Glauber model. As two nuclei collide more centrally, the number of N_{coll}^{AA} increases. $\langle N_{coll}^{pp} \rangle$ is the number of binary collision of the $p + p$ collision and has 1. And dN_{pp}^i is the invariant yield of the particle, i . Since nuclear collision system is scaled by the number of binary collisions, R_{AA} become 1 if there is no nuclear effect comparing to $p + p$ collision. But if there is suppression, the value becomes less than 1 and if there is enhancement, the value becomes more than 1. So by this parameter, the characteristic of nuclear matter can be quantitified for the

specific bins of kinematics or geometry. R_{CP} is defined as

$$R_{CP}^i = \frac{dN_{AA0-20\%}^i/dy_i \langle N_{coll0-20\%}^{AA} \rangle}{dN_{AA60-88\%}^i/dy_i \langle N_{coll60-88\%}^{AA} \rangle}, \quad (1.4)$$

R_{CP} use peripheral collision instead of $p + p$ collision as the reference. $N_{colli-j\%}^{AA}$ is the number of binary collision of the nuclear collision system of $i - j\%$ centrality. $dN_{AAi-j\%}^i$ is the invariant yield of the particle, i of $i - j\%$ centrality. For R_{CP} , peripheral collision is assumed to have no nuclear matter effects. R_{CP} gives the benefits to cancel out the systematic uncertainties since one use same system of AA collision. But, one should be careful that even the peripheral collision might have more or less nuclear effect.

1.3 Phenomena of nuclear collisions

1.3.1 Color screening

In 1986 Matsui and Satz predicted that the color screening of a $c\bar{c}$ would be a signature of Quark-Gluon Plasma (QGP) formation [8]. While others hinted at similar effects [4], this publication was the first quantitative study. They proposed that if a QGP is formed in a nucleus-nucleus collision, then any $c\bar{c}$ pair that would have normally evolved into bound charmonium would be color screened from one another. Instead of a final state of bound charm, the c and \bar{c} would instead pair up with the more abundant lighter quarks to form charmed mesons at the hadronization. In a QGP where other quarks and gluons are in close proximity to the $c\bar{c}$ pair, their color charge will screen one charm quark from seeing the anti-charm quark. This type of screening is called Debye screening analogous to the electric charge screening in Quantum Electrodynamics. And it is parametrized by the Debye screening radius, λ_D , the radius at which the effective charge of a particle is reduced by a factor of $1/e$. Outside the medium, $c\bar{c}$ states can be reasonably represented by a potential model, with the potential energy

$$|V|(r) = \kappa r - \frac{\alpha_{eff}}{r} \quad (1.5)$$

Inside the QGP, however, the linear term will disappear as T approaches the critical temperature and a screening factor will be introduced to the Coulombic term, giving rise to the modified potential

$$V(r) = -\frac{\alpha_{eff} e^{-r/\lambda_D}}{r} \quad (1.6)$$

where λ_D is determined by the temperature of the medium. For a quark gluon plasma with three flavors of quarks evaluated from the lowest order perturbative QCD, the screening length is given by

$$\lambda_D = \sqrt{\frac{2}{3g^2}} \frac{1}{T} \quad (1.7)$$

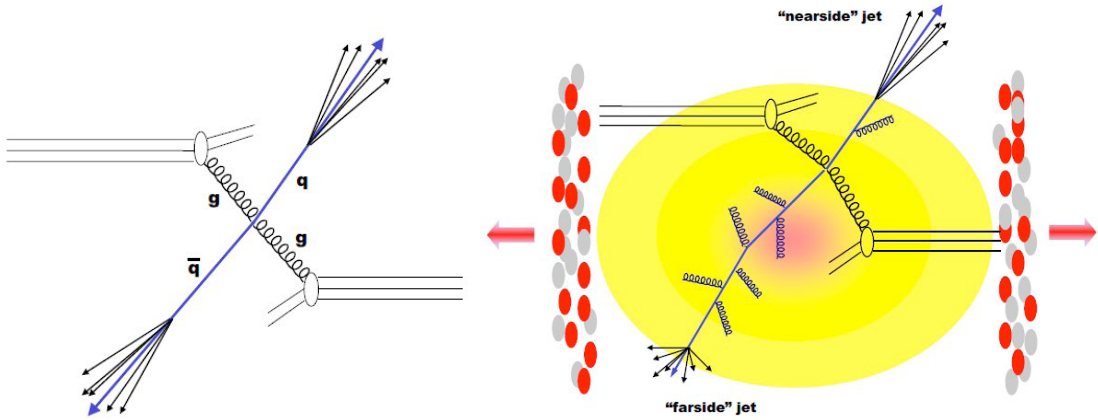


Figure 1.5: A production of a pair of jets in a nucleon-nucleon collision (Left). An illustration of the associated pair of jets traveling through the dense deconfined medium created as a result of the collision of two heavy ions (Right).

If the screening length is less than the $q\bar{q}$ Bohr radius of a given quarkonium state, then no bound quarkonium of that state can exist in the QGP.

1.3.2 Jet quenching

Jet production is considered to be one of the best theoretical and experimental tools for studying the properties of the QGP matter. Jets are initially produced in the hard scatterings ($Q > 2$ GeV) of incoming partons which usually results in the subsequent creation of pairs of outgoing high p_T partons. Each of these high p_T partons later fragment into a leading energetic hadron and large number of other hadrons concentrated in the nearby cone, providing a very clear experimental pattern as shown in Figure 1.5. Because of the associated large energy scale, the initial production and later hadronization of jets can be precisely calculated within the perturbative QCD (pQCD) framework. Hard scatterings are essentially point-like processes occurring in a very short time scale ($\tau \sim 1/p_T \sim 0.1\text{fm}/c$). Therefore, the initial production cross section of the high p_T jet partons in $A + A$ collisions is expected to scale with the production cross section measured in $p + p$ collisions. However, unlike in $p + p$ collisions, these high p_T partons encounter the created deconfined medium, and subsequently will suffer energy loss due to medium-induced gluon bremsstrahlung and the collisions with abundant in-medium partons. Consequently, as illustrated in Figure 1.5 the jets produced near the medium surface in the out-of-medium direction, nearside-jets, will suffer much smaller energy loss, as opposed to the farside-jets that have to travel through the most of the medium. PHENIX measurements show a large suppression (by a factor of 4 - 5) of high p_T hadron

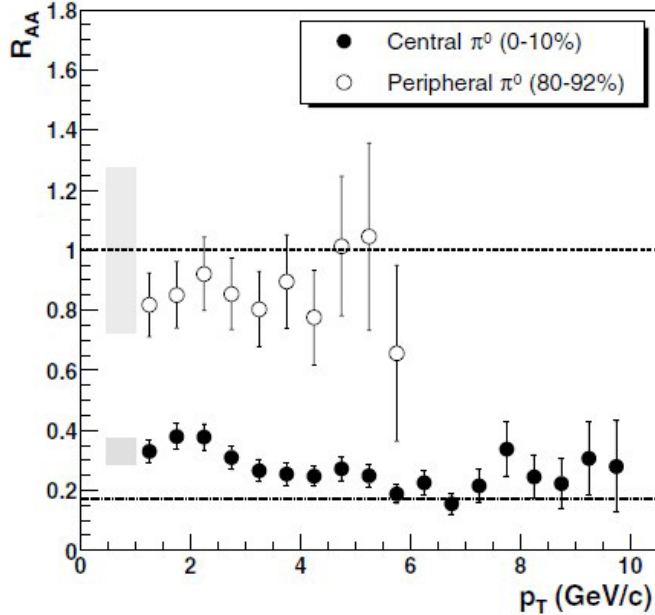


Figure 1.6: The PHENIX measurement of the nuclear modification factor for π^0 production in the most central and peripheral Au+Au collisions [15]

production in the most central (0 - 10%) Au+Au collisions as compared to $p + p$ and $d + \text{Au}$ data, as shown in Figure 1.6. Separately, the measurement of the correlated dijets by the STAR experiment, shown in Figure 1.7, reveal that in the central Au+Au collisions the high p_T component of the signal from away-side jets is completely vanished, in contrast to what has been observed either in $p + p$ or $d + \text{Au}$ collisions. These results from the two experiments are clearly suggestive of rather remarkable in-medium effects that can be caused only by the presence of a very dense and strongly interacting medium.

1.3.3 Elliptic flow

Another striking feature observed in heavy ion collisions, totally absent in $p + p$ collisions, is the spatial anisotropy of the produced multiplicities of the various hadron species. This effect was most profound in non-central collisions ($b \neq 0$). In this case, due to the specific overlap, the incoming nuclei initially creates matter with an almond like asymmetric shape, as illustrated in Figure 1.8. Now, if the QGP is a gas-like state of matter of weakly interacting partons, the created spatial asymmetry should quickly disappear due to the rapid thermal expansion, resulting in a nearly spherically symmetric expansion. Conversely, if the partons inside the medium experience much stronger interactions between each other than was originally presumed, the multiple rescatterings

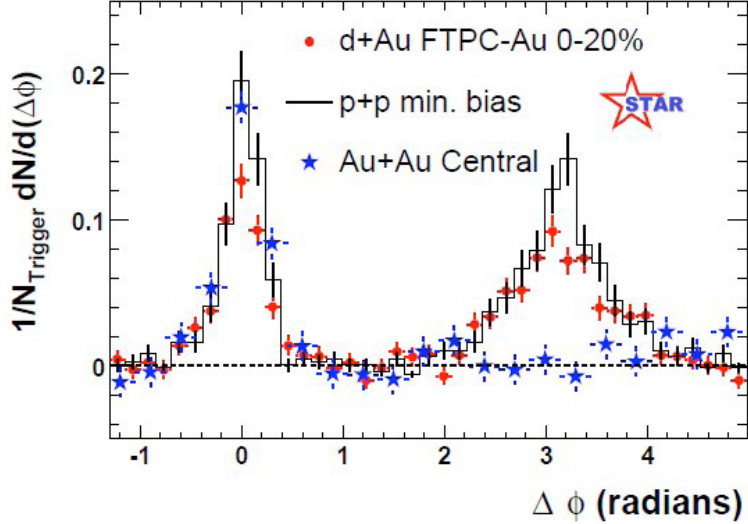


Figure 1.7: The comparison of the correlated two-particle azimuthal distributions observed in most central Au+Au collisions to those seen in p+p and d+Au collisions, measured by the STAR experiment [16]

occurring in the system will develop pressure gradients directed outwards, with the largest ones along the x-axis in the reaction plane, Φ_R , which is the smallest of the almond axes. Consequently, as illustrated in Figure 1.8, the spatial anisotropy of the bulk turns into a momentum anisotropy referred to as elliptic flow of the partons. Finally, once the system hadronizes, particles are emitted asymmetrically in azimuth. The magnitude of the elliptic flow is quantified by the second Fourier coefficient, v_2 , of the azimuthal expansion of single semi-inclusive hadron spectra with respect to the reaction plane:

$$E \frac{d^3 N}{d^3 p} = \frac{1}{2\pi p_T} \frac{d^2 N}{dp_T dy} (1 + 2\sum_{n=1}^{\infty} v_n \cos[n(\phi - \Phi_R)]) \quad (1.8)$$

Shown in Figure 1.9 is the elliptic flow of the various hadron species measured by the PHENIX and STAR experiments compared to the corresponding hydrodynamical model predictions. A substantial v_2 is measured over a wide p_T range, indicating the strong collectivity of the bulk matter in the initial phases of the collisions. It is important to note that in the kinematic range of $p_T \leq 2$ GeV, where the vast majority of the bulk particles are produced, the data is in good agreement with the hydrodynamical model prediction, which uses very short thermalization times (≤ 0.6 fm/c) as an input parameter, and assumes a strongly interacting liquid of a small viscosity to entropy ratio.

Figure 1.10 shows the same data, but this time the measured elliptic flow for each hadron species is scaled with the number of the corresponding constituent quarks, v_2/n . Quite

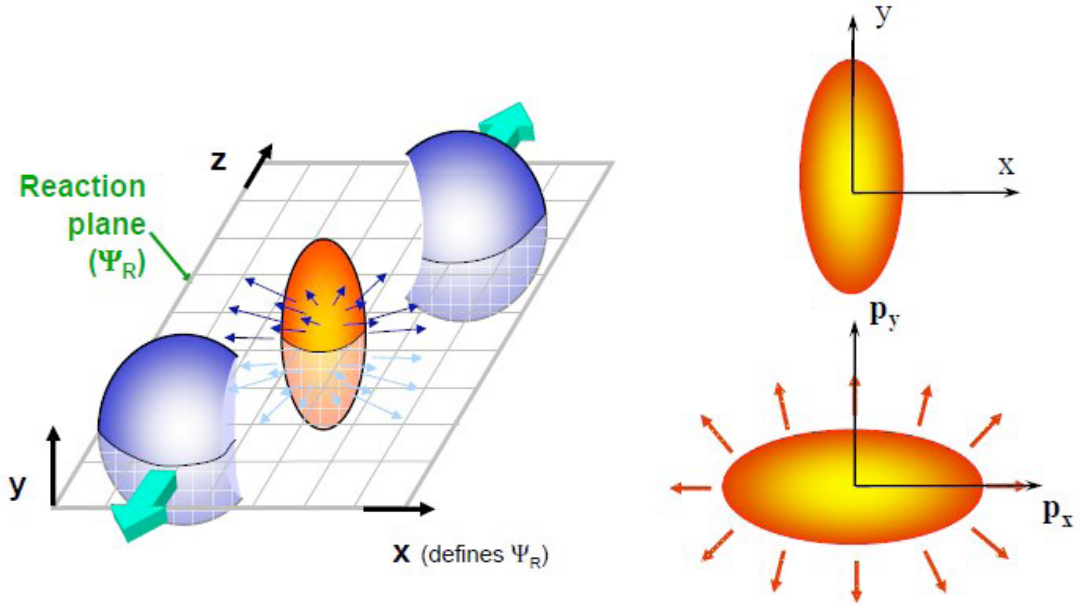


Figure 1.8: Illustration of the almond shaped matter created as the result of a non-central collision of heavy nuclei moving along the reaction plane and z-axis.

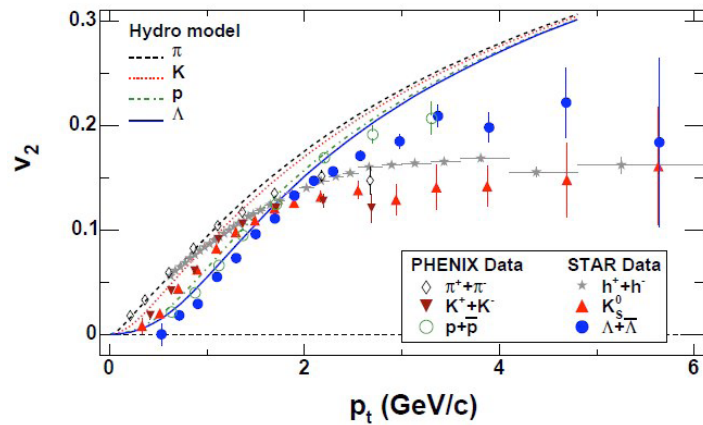


Figure 1.9: A comparison of the PHENIX and STAR measurements of the v_2 variable for the different hadron species [17][18] to the hydro model predictions from [19].

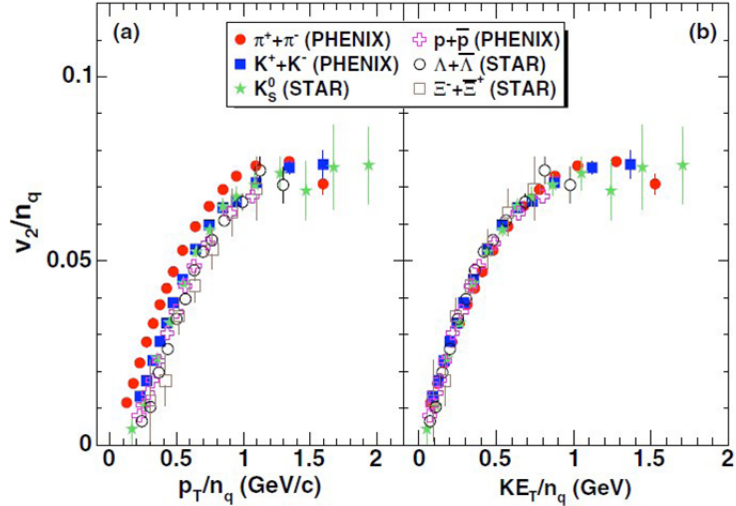


Figure 1.10: A compilation from [20] of the PHENIX and STAR results [21],[22] of v_2/n as a function of p_T (a), and kinetic energy (b) for various hadron species.

remarkably, v_2/n for all hadron species follow identical universal scaling. This strongly indicates that it is quarks (partons) during the early times of the collisions, not hadrons, that participate in the collective motion caused by strong interactions. It turned out that the matter created in the Au + Au collisions at RHIC is consistent with a liquid-like strongly interacting bulk with very short thermalization times, quite different from the initially conjectured gas-like plasma. The data strongly supports the notion that the degrees of freedom of the created matter are of partonic origin, which would be a clear indication of deconfinement. PHENIX has also measured preliminary J/ψ v_2 recently as shown in Figure 1.11. This result is expected to provide a valid information about the J/ψ production mechanisms at heavy ion collisions. If J/ψ are produced from $c\bar{c}$ recombination in a deconfined phase [24], they should inherit their flow. On the contrary, J/ψ directly produced by hard QCD processes early in the collision cannot be sensitive to collective phenomena. Therefore, measuring a positive J/ψ elliptic flow would indicate the level of recombination that takes part in the J/ψ production mechanisms [25]. Intitial production, regeneration and comover interaction models are being applied to explain the data.

1.3.4 Charmonium suppression

Perhaps the most famous and the most controversial subject in the heavy ion physics, charmonium suppression has long been proposed as a direct evidence that the matter created in the heavy ion collisions is of a deconfined nature [8]. The J/ψ , particle is

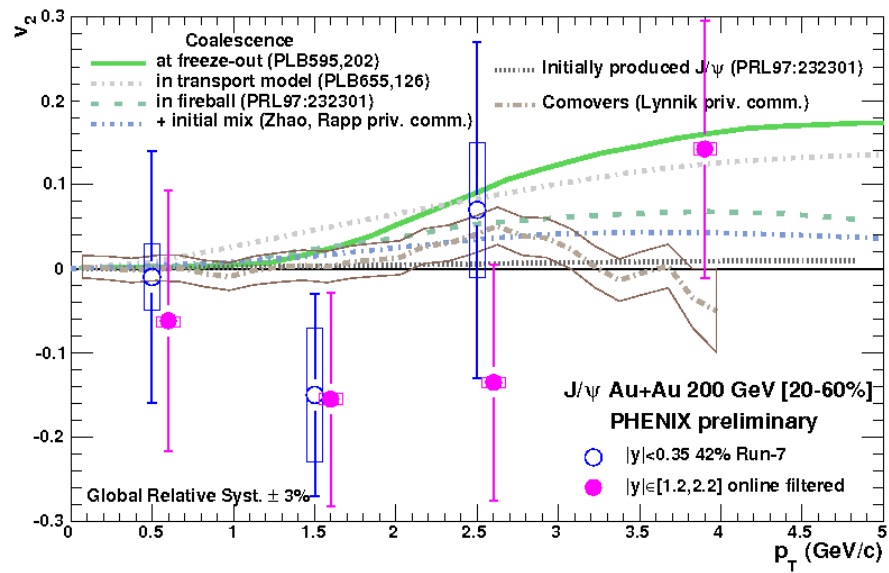


Figure 1.11: J/ψ v_2 at $|y| < 0.35$ and at $|y| \in [1.2, 2.2]$ for [20,60%] in centrality, as a function of p_T , using the data of 2007 Au + Au, with theoretical models. Error bars are statistical errors uncorrelated point to point, boxes are systematic errors correlated between each p_T bins, and a global systematic error is written.

the lightest and the most stable of the charmonium vector mesons, the bound states of the $c\bar{c}$ pairs. A $c\bar{c}$ pair is initially produced as a result of hard partonic collisions and subsequently hadronizes into a J/ψ particle. In normal QCD matter, the strong (confining) potential between the colored ccbar quarks at large distances behaves as

$$V_0(r) \sim \sigma r, \quad (1.9)$$

with σ being the string tension [9]. Thus, an infinitely large energy would be required to break up the bond between the pair. However, if a system of $c\bar{c}$ finds itself in a dense environment of deconfined partons, the strong potential between the $c\bar{c}$ quarks will be screened due to the presence of other color charges [10],

$$V_0(r) \sim \sigma r \left[\frac{1 - e^{-\mu r}}{\mu r} \right] \quad (1.10)$$

with μ being the inverse of a screening radius. This is analogous to the Debye screening of the electromagnetic potential arising in a plasma of electric charges. As a result, J/ψ production is expected to be suppressed in the deconfined environment. Remarkably, this was exactly what was initially observed in the heavy ion collisions at the CERN SPS, as shown in Figure 1.12. The suppression was not observed in the peripheral collisions of light nuclei, which was interpreted by many as a proof that QGP was indeed produced in the ultrarelativistic heavy ion collisions at the SPS. However, it turned out that the production of J/ψ particles is also suppressed in p + A type collisions. These collisions are not expected to produce hot and dense deconfined matter, which suggests that there are some cold nuclear matter effects (different from the suggested color screening) that are absolutely necessary to take into account. In particular, gluon shadowing, the depletion of small momentum (with respect to the momentum of nucleon) gluons inside nuclei [11]. Another possible effect is Cronin Effect, the observed broadening of p_T [12], also seen for the production of different particle species [13]. Understanding charmonium production and the underlying mechanisms of its suppression in heavy ion collisions is one of the priorities of the heavy ion physics program at RHIC.

The measurements observed at RHIC are strongly supportive of the hypothesis that the matter created in the heavy ion collision is of deconfined nature. However, these results were indeed unexpected based on the early theoretical predictions for the QGP as a gas-like state of weakly interacting partons. Instead the data strongly suggest that the matter created in the early stages of heavy ion collisions behaves as a liquid-like, very dense and strongly interacting medium of color charges, often referred to as strongly-coupled QGP (sQGP).

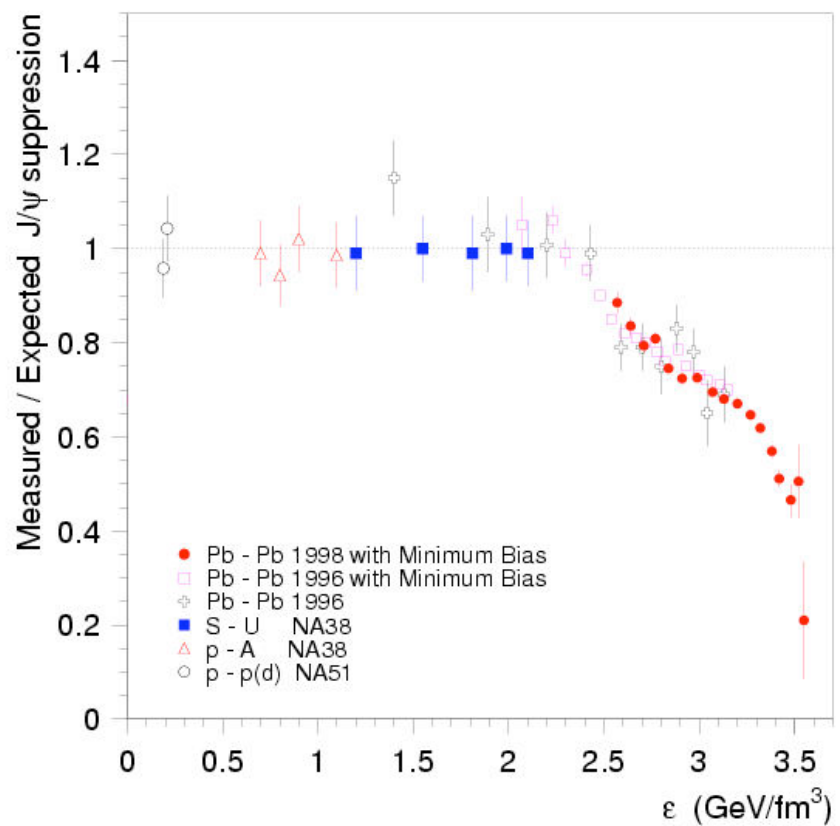


Figure 1.12: The ratio of the measured to the expected charmonium production as a function of energy density for the collisions of the different ion species as measured at SPS [26].

1.4 Cold Nuclear Matter effect and quarkonia measurement

Two effects have typically been referred to as cold nuclear matter effects: a) modifications of the parton distribution functions in the nucleus relative to the nucleon, assumed to be an initial-state effect, intrinsic to the nuclear target, often referred to as shadowing, and b) the absorption (destruction, breakup) of the quarkonium state as it passes through the nucleus. Since the latter effect occurs after the $Q\bar{Q}$ pair has been produced and while it is traversing the nuclear medium, this absorption is typically referred to as a final-state effect. Another quarkonia states, Υ and χ_c as well as J/ψ would help to understand and entangle the puzzles of various mechanisms of cold nuclear matter. In this thesis, Υ and χ_c results will be shown.

1.4.1 Nuclear Shadowing

It is known that nuclear structure functions in nuclei are different from the superposition of those of their constituents. And the nuclear ratio is defined as the nuclear structure function per nucleon divided by the free nucleon structure function.

$$R_i^A(x, Q^2) = \frac{F_i^A(x, Q^2)}{AF_i^{nucleon}(x, Q^2)}. \quad (1.11)$$

where i is each parton flavor, A is the nuclear mass number for Bjorken x and momentum transfer, Q^2 [29]. Recently developed next-to-leading order(NLO) nuclear parton distribution functions(nPDFs), called EPS09 [31], and another nPDFs represent gluon modification in lead nucleus at Figure 1.14. In $d + Au$ collisions of $\sqrt{s_{NN}} = 200$ GeV at PHENIX, gluons are estimated to have momentum fraction $x \sim 3 \times 10^{-3}$ for J/ψ and $x \sim 1 \times 10^{-2}$ for Υ in Au nucleus at positive rapidity which is deuteron-going direction [30]. That region is in the shadowing region in the Figure 1.13 and Figure 1.14. This provides one explanation to understand the quarkonia suppression of PHENIX heavy ion collisions since gluons are the dominant source of quarkonia production.

1.4.2 Nuclear absorption cross section

After produced, quarkonia attenuate in the nucleus on the way out of it [38][39]. Physical picture of nuclear absorption of charmonium described in this subsection is based on Ref. [41]. The effect of nuclear absorption alone on the charmonium production cross section in $p + A$ collisions may be expressed as

$$\sigma_{pA} = \sigma_{pp} \int db \int_{\infty}^{\infty} dz \rho_A(b, z) S^{abs}(b, z), \quad (1.12)$$

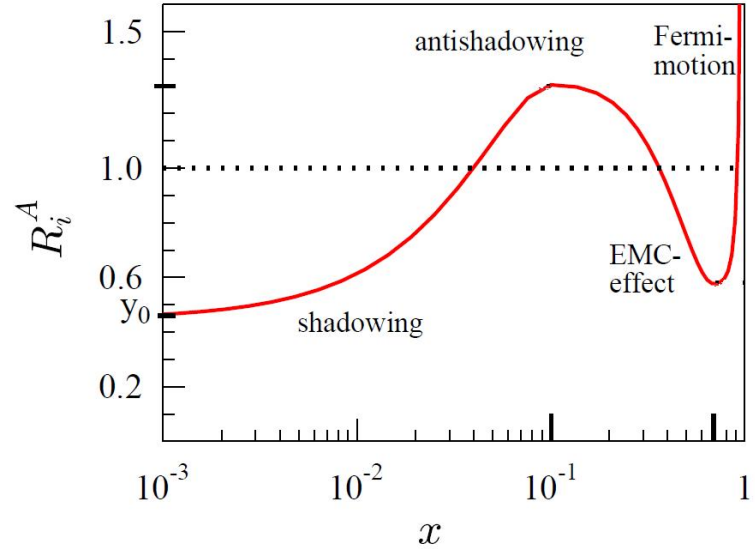


Figure 1.13: An illustration of the fit function $R_i^A(x)$

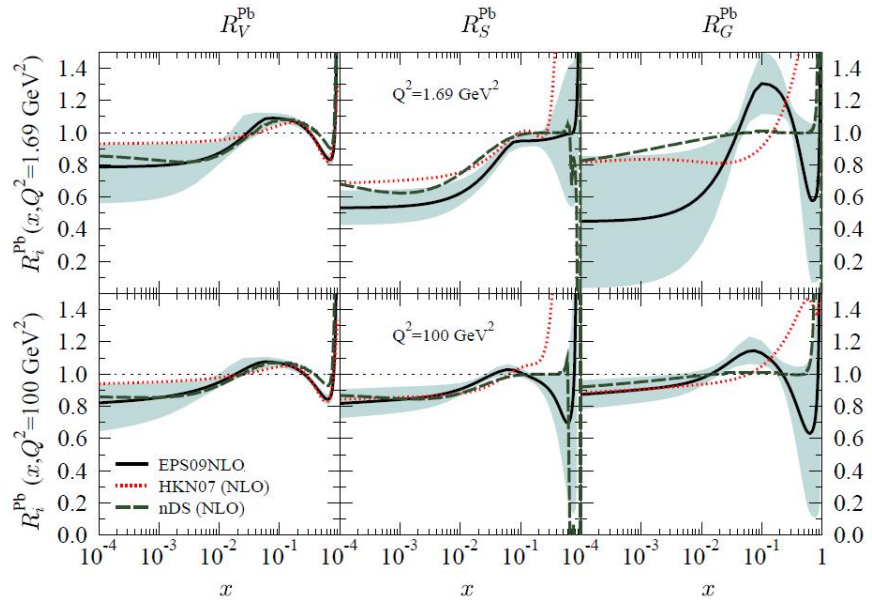


Figure 1.14: Comparison of the average valence and sea quark, and gluon modifications at $Q^2 = 1.69 \text{ GeV}^2$ and $Q^2 = 100 \text{ GeV}^2$ for Pb nucleus from the NLO global DGLAP analyses HKN07 [32], nDS [33] and this work, EPS09NLO [31].

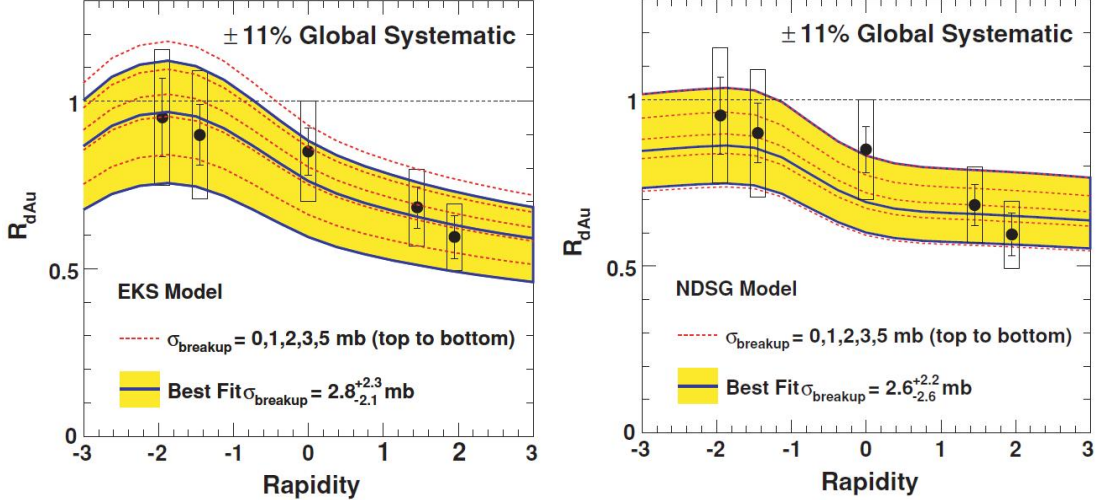


Figure 1.15: R_{dAu} data compared to various theoretical curves for different $\sigma_{breakup}$ values. Also, shown as a band are the range of $\sigma_{breakup}$ found to be consistent with the data within one standard deviation. The left panel is a comparison for EKS shadowing [34] while the right panel is for NDSG shadowing [35]

where b is the impact parameter, z is the longitudinal production point and ρ_A is the nucleon density of the nucleus A. If the production and absorption can be factorized and no other A dependent effects are included, the nuclear absorption survival probability, S^{abs} , is

$$S^{abs}(b, z) = \exp\left\{-\int_z^\infty dz' \rho_A(b, z) \sigma_{abs}(z - z')\right\}, \quad (1.13)$$

where σ_{abs} is the absorption cross section of charmonia or preresonant $c\bar{c}$ states. The effective A dependence is obtained from Eqs. 1.12 and 1.13 by integrating over z , z' and b . PHENIX has published the J/ψ data on cold nuclear effect [37] which explains the data by shadowing models and nuclear absorption models Figure 1.15. And the shadowing models with nuclear absorption models were used to estimate the contribution from cold nuclear matter effects that should be present in Cu + Cu and Au + Au collisions. These contributions, obtained using the best-fit value of $\sigma_{breakup}$ and their one-standard-deviation values extracted from the data in Figure 1.15 for each of the two shadowing models, are shown in Figure 1.16 and Figure 1.17. In the Cu + Cu case, J/ψ production is not suppressed beyond cold nuclear matter effects at midrapidity or at forward rapidity, within the limits of the large error bands, and the midrapidity data in the Au + Au case are similarly inconclusive. However, there is a significant suppression in the data at forward rapidity, beyond the uncertainties in both the data and the projection [37]. And recent R_{CP} of J/ψ data, which has an increase in yield by a factor of 30 - 50 over

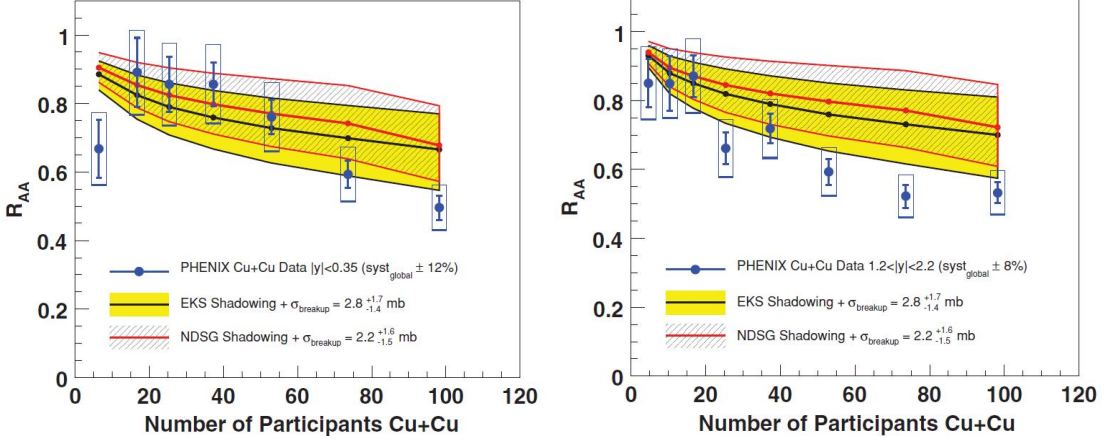


Figure 1.16: R_{AA} for Cu+Cu [5] collisions compared to a band of theoretical curves for the $\sigma_{breakup}$ values found to be consistent with the $d + \text{Au}$ data as shown in Figure 1.15. The left figure includes both EKS shadowing [34] and NDSG shadowing [35] at midrapidity. The right figure is the same at forward rapidity.

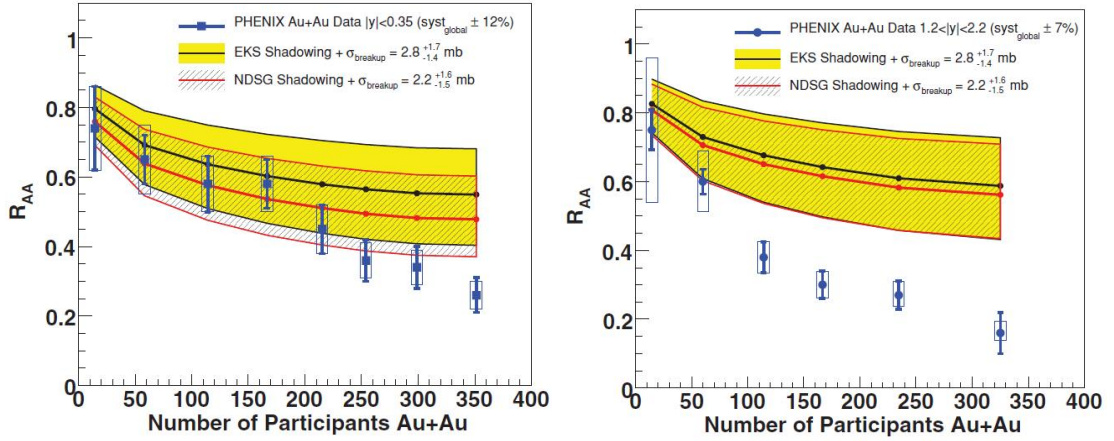


Figure 1.17: R_{AA} for Au+Au [1] collisions compared to a band of theoretical curves for the $\sigma_{breakup}$ values found to be consistent with the $d + \text{Au}$ data as shown in Figure 1.15. The left figure includes both EKS shadowing [34] and NDSG shadowing [35] at midrapidity. The right figure is the same at forward rapidity.

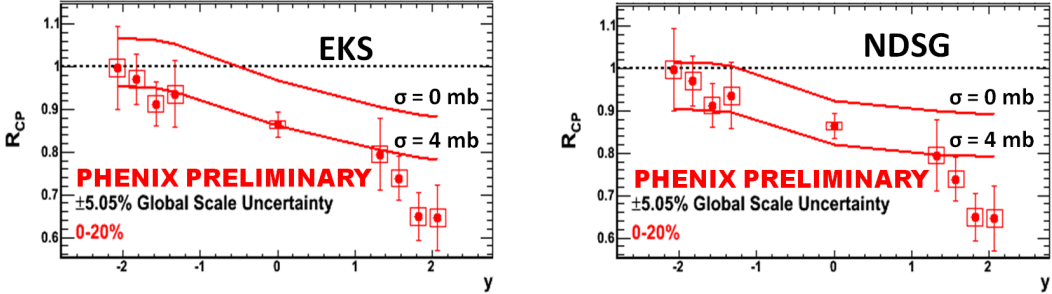


Figure 1.18: J/ψ nuclear modification R_{CP} versus rapidity compared to shadowing models of EKS [34] and NDSG [35] nuclear parton distribution modification fuctions(nPDFs). Each shadowing model has uniform breakup cross sections of 0 mb and 4mb.

the previous results, shows anormal supresion in low x region as seen at Figure 1.18. So another models, for example, initial state parton energy loss is being suggested to explain the behavior.

1.4.3 Cronin effect

Partons suffer multiple scatterings while they traverse in nuclei before charmonium production. Partons from the projectile nucleus collide with various target nucleons exchanging a transverse momentum in each collision. This makes the p_T distribution of charmonia wider compared to that in $p + p$ collisions and is known as the Cronin effect [46]. The mean squared transverse momentum $\langle p_T^2 \rangle$ depends on the production point $x = (b, z)$,

$$\langle p_T^2 \rangle(b, z) = \langle p_T^2 \rangle_{pp} + \langle p_T^2 \rangle_{gN} \sigma_{gN} \int_{-\infty}^z dz' \rho_A(b, z'), \quad (1.14)$$

where $\langle p_T^2 \rangle_{pp}$ is the mean squared transverse momentum in $p+p$ collisions, σ_{gN} is gluon-nucleon cross section, $\langle p_T^2 \rangle_{gN}$ is the mean squared transverse momentum acquired per gluon-nucleon collision and ρ_A is the nucleon number density of a nucleus A. Eq.(1.14) can be written in terms of the pass length L using a coefficient a_{gN} which includes σ_{gN} and $\langle p_T^2 \rangle_{gN}$,

$$\langle p_T^2 \rangle = \langle p_T^2 \rangle_{pp} + a_{gN} L.$$

1.5 Quarkonia system

Quarkonia are bound states of heavy quark-antiquark pairs. Quarkonia composed of charm quarks and anti-charm quarks ($c\bar{c}$) are called charmonia and quarkonia composed of bottom quarks and anti-bottom quarks ($b\bar{b}$) are called bottomonia. Figure 1.19 shows

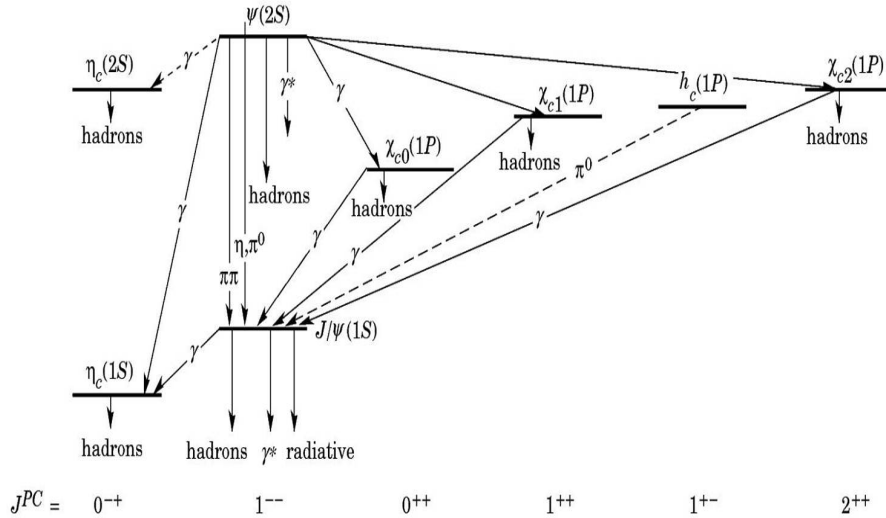


Figure 1.19: The current state of knowledge of the charmonium system and transitions, as interpreted by the charmonium model. Uncertain transitions are indicated by dashed lines. The notation γ refers to decay processes involving intermediate virtual photons, including decays to $\mu^+\mu^-$ and e^+e^- [49].

the level scheme of the charmonium family with quantum numbers in the vacuum. And Figure 1.20 shows the level scheme of the bottomonium family. Properties of J/ψ and three states of χ_c are listed in Table 1.1. The branching ratio (BR) of J/ψ in the $\mu^+\mu^-$ (e^+e^-) mode is $BR = 5.93 \pm 0.06\%$ ($5.94 \pm 0.06\%$). At temperature $T = 0$, the level scheme of the quarkonium bound states can be reasonably described with the nonrelativistic potential,

$$V(r, T = 0) = -\frac{4}{3} \frac{\alpha_s(r)}{r} + \sigma r, \quad (1.16)$$

where r is the separation between the heavy quark Q and the heavy antiquark \bar{Q} . This naive potential does not account for spin-orbit or spin-spin couplings needed to separate the three χ_c states or to separate J/ψ from η_c , respectively. The $1/r$ term is Coulomb-like and governs the short distance behavior of the potential. It arises from the exchange of a gluon between the Q and \bar{Q} . The shorter the distance scale, corresponding to increasing momentum scales, the weaker the coupling. The linear term corresponds to the confining potential. The strength of the confining term is determined by the string tension, σ . The quarkonium energy levels depend not only on the potential but also on the a priori unknown masses of heavy quarks, m_c and m_b . The four parameters α_s , σ , m_c and m_b can be roughly determined by fitting the spectra and the obtained values are

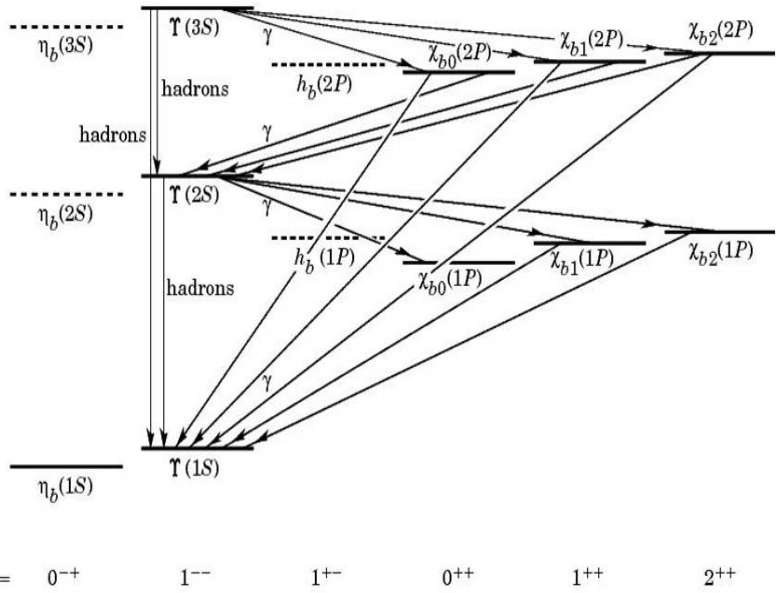


Figure 1.20: The current state of knowledge of the bottomonium system and transitions, as interpreted by the charmonium model. Uncertain transitions are indicated by dashed lines. The notation γ refers to decay processes involving intermediate virtual photons, including decays to $\mu^+ \mu^-$ and $e^+ e^-$ [49].

Particle	Mass (MeV/ c^2)	Mass width (MeV/ c^2)	Mass difference from J/ψ (MeV/ c^2)	$BR(\chi_{cJ} \rightarrow J/\psi \gamma)$
$J/\psi(1S)$	3096.916 ± 0.011	0.0934 ± 0.0021		
$\chi_{c0}(1P)$	3414.76 ± 0.35	10.4 ± 0.7	318	$1.30 \pm 0.11 \%$
$\chi_{c1}(1P)$	3510.66 ± 0.07	0.89 ± 0.05	414	$35.6 \pm 1.9 \%$
$\chi_{c1}(1P)$	3556.20 ± 0.09	2.06 ± 0.12	459	$20.2 \pm 1.0 \%$

Table 1.1: Mass, mass width and radiative decay branching ratio (BR) of J/ψ and three χ_c states from PDG 2010.

Particle	Mass (GeV/ c^2)	Radius (fm)
$J/\psi(1S)$	3.070	0.453
$\chi_c(1P)$	3.500	0.696
$\psi'(2S)$	3.698	0.875
$\Upsilon(1S)$	9.445	0.226
$\Upsilon(2S)$	9.778	0.509
$\chi_b(1P)$	9.829	0.408

Table 1.2: Mass and radius of each quarkonium obtained from a potential model [48].

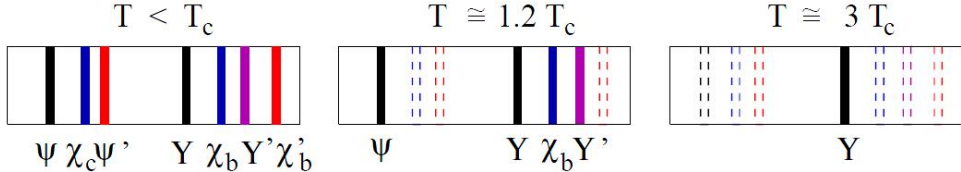


Figure 1.21: Quarkonium spectral lines as thermometer [47].

[48].

$$\alpha_s = 0.353, \quad (1.17)$$

$$\sigma = 0.192 GeV^2, \quad (1.18)$$

$$m_c = 1.32 GeV/c^2, \quad (1.19)$$

$$m_b = 4.75 GeV/c^2, \quad (1.20)$$

The masses and radii of charmonia estimated by the potential model are shown in Table 1.2.

1.6 Quarkonia measurement as probes of production mechanism

The investigation of J/ψ suppression proposed by Matsui and Satz [8] has long been considered as one of the most promising signatures of QGP formation and is one of the primary subjects of the PHENIX experiment. In QGP, Debye screening limits reach of the color field of a quark within the Debye length λ_D . As temperature increases, λ_D decreases. If λ_D becomes smaller than the radius of a quarkonium (J/ψ , ψ' , χ_c and Υ), the quarkonium becomes unbound [47] and resolve as Figure 1.21. J/ψ has a large production cross section and di-lepton (e^+e^- , $\mu^+\mu^-$) decay channels. Leptons have the advantage that they are experimentally easily identified. Therefore, among quarkonia,

J/ψ has been used as a tool of QGP search in high-energy heavy-ion collisions. In high-energy heavy-ion collisions, the J/ψ yield is also reduced by cold nuclear matter (CNM) effects. The CNM effects include absorption of J/ψ into nuclei and the modification of parton distribution function in nuclei. But the production mechanism of the nuclear matter is still not explained successfully between the various theoretical expectations. Another quarkonia measurement of Υ , ψ' and χ_c is expected to provide another constraints for the theories so disentangle those expectations since they have different mass and binding radii to J/ψ . This thesis focuses on the study of the cold nuclear matter effects of $\Upsilon \rightarrow \mu^+ \mu^-$ and $\chi_c \rightarrow \mu^+ \mu^- \gamma$ among the heavy quarkonia states.

1.7 Υ and χ_c measurement from another experiments

PHENIX has the preliminary result for Υ as shown in Figure 1.22. At mid rapidity, PHENIX and STAR cross sections of $\sqrt{S} = 200\text{GeV}$ $p+p$ collision follow the theoretical line of the Color Evaporation Model(CEM) (Figure 1.22). Figure 1.23 is the preliminary result for the Υ measurement of $d + \text{Au}$ collision at STAR. They present the nuclear modification factor $R_{d\text{Au}} = 0.98 \pm 0.32(\text{stat.}) \pm 0.28(\text{sys.})$ at mid rapidity Figure 1.24 shows R_{χ_c} , which is defined

$$R_{\chi_c} = \frac{1}{\sigma_{J/\psi}} \sum_{J=0}^2 BR(\chi_{cJ} \rightarrow J/\psi \gamma) \sigma_{\chi_{cJ}}, \quad (1.21)$$

where BR and σ are the branching ratio and cross section, respectively for various collision sets. PHENIX shows $R_{\chi_c} < 0.42$ with confidence level of 90 % at mid rapidity. Figure 1.25 is the preliminary Υ $R_{\text{AuAu}} < 0.64$ with confidence level of 90 %. This thesis will show the PHENIX Υ cross section and the nuclear modification factor $R_{d\text{Au}}$ and χ_c measurement at forward rapidity.

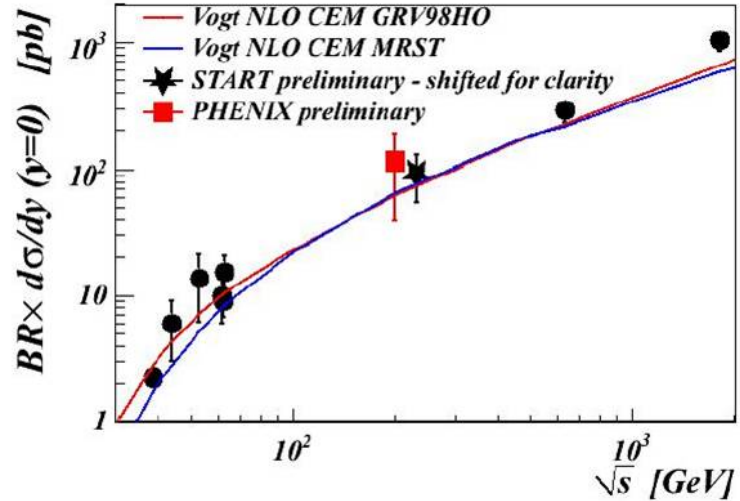


Figure 1.22: Collision energy dependence of Υ cross section at mid rapidity from PHENIX and other experiments.

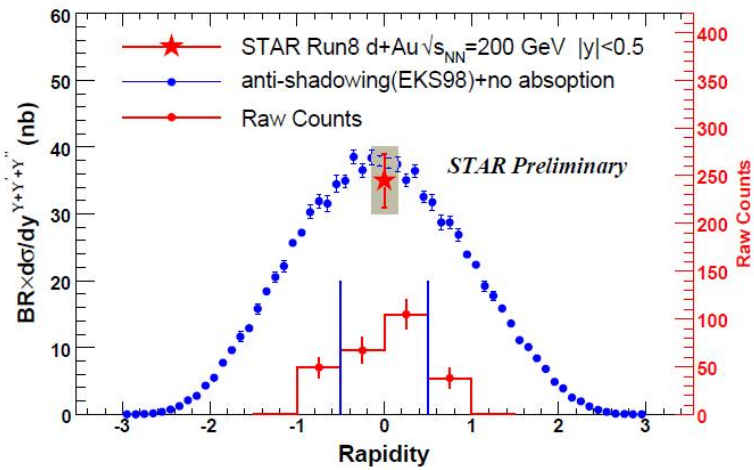


Figure 1.23: The red star shows the measured $BR \times (\frac{d\sigma}{dy})_{y=0}^{\Upsilon(1S+2S+3S)}$ at midrapidity. The bar indicates the statistical error and the band shows the systematic uncertainty. The cross section is compared with the NLO CEM model prediction (blue solid circles). The raw yields vs. rapidity is shown by the red histogram at the bottom with the statistical errors.

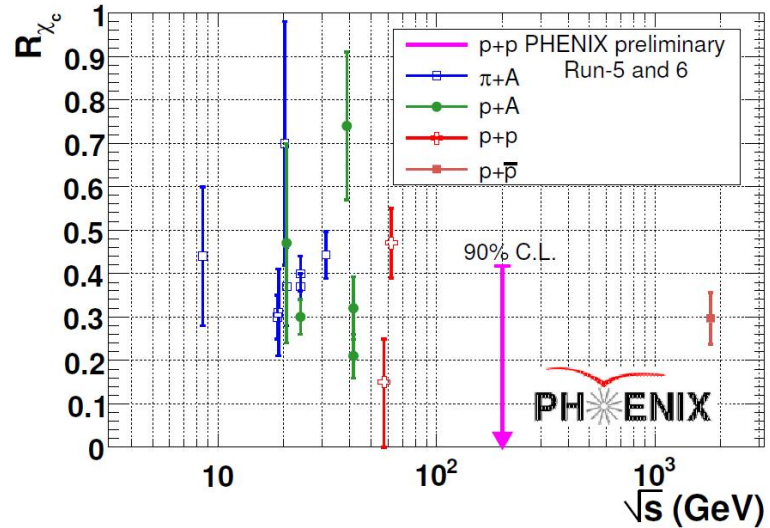


Figure 1.24: The 90 % confidence level upper limit of the R_{χ_c} value < 0.42 obtained from PHENIX Run-5 p + p and Run-6 p + p data. The R_{χ_c} values obtained from other experiments are also shown as a function of beam energy.

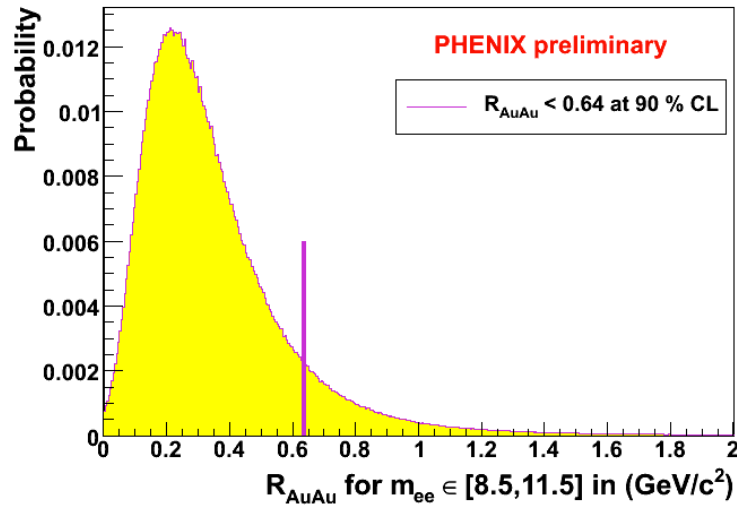


Figure 1.25: The 90 % confidence level upper limit of the Υ R_{AA} value < 0.64 obtained from PHENIX Run-7 Au + Au and Run-6 p + p data at mid rapidity, $|y| < 0.35$.

Chapter 2

Experimental Setup

2.1 RHIC and PHENIX detector

The Relativistic Heavy Ion Collider(RHIC) is located at the Brookhaven National Laboratory(BNL) in Upton, New York [50][51][52]. RHIC collides heavy ions to study the primordial form of matter that existed in the universe shortly after the Big Bang[53] or collides spin-polarized protons to study the spin structure of the proton. Beams are accelerated through LINAC, Booster and AGS, and then injected to RHIC.

2.1.1 LINAC

The LINAC is a 200 MHz linear accelerator which brings the nuclearly polarized \mathbf{H}^{1-} atoms to 200 MeV and strip-injects the ions into the Booster.

2.1.2 Booster

The Booster, a fast cycling synchrotron, captures the $400 \mu\text{s}$ pulse into a single bunch of protons, accelerates them to 2.35 GeV and injects them into the AGS. The Booster acceleration stage is spin-transparent.

2.1.3 AGS

The Alternating Gradient Synchrotron (AGS) further accelerates the polarized protons to 24.3 GeV. Depolarizing resonances in the AGS are overcome by RF dipoles and Siberian Snakes.

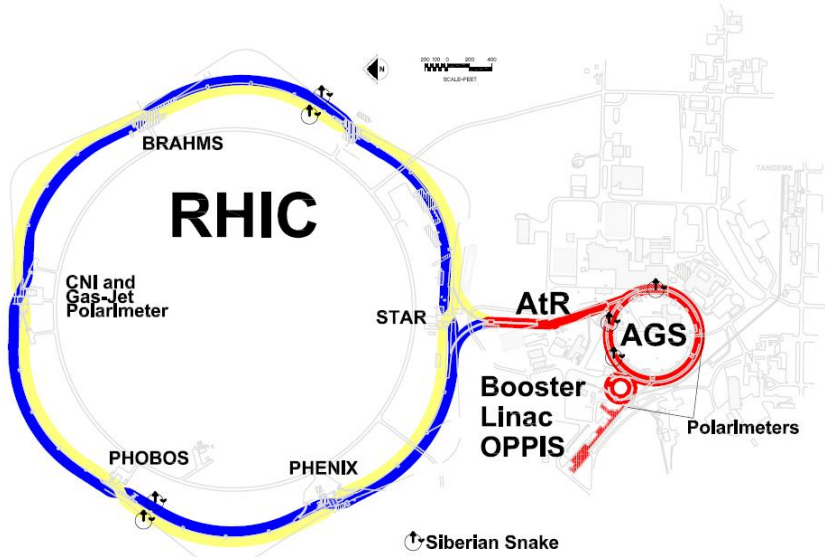


Figure 2.1: PHENIX, STAR, PHOBOS, BRAHMS at RHIC

2.1.4 RHIC

The RHIC double rings are hexagonally shaped and 3,834 m long in circumference, with curved edges in which particles are deflected and focused by 1,740 superconducting niobium-titanium magnets. The dipole magnets operate at 3.45 T. Starting in the year 2000, RHIC has been colliding at center of mass energies ranging from 7.7 to 200 GeV for heavy ions and 62.4 to 500 GeV for polarized protons. Several features of the accelerator make it unique: collisions of non-symmetric ions are possible; it was designed to operate at many energies rather than a single peak energy; and it is the only facility colliding polarized protons. The accelerator is a synchrotron in that the ions are accelerated in packets as opposed to a continuous stream. The packets of particles, called bunches, are accelerated by two independent accelerator rings called Blue (clockwise) and Yellow (counterclockwise), provide collisions for roughly eight hour periods during which time the beam luminosity drops, and then the beams are dumped. Each packet contains roughly 1.4×10^{12} protons which are separated from one another by 106 ns. The interaction points are enumerated by clock positions, with the injection near 6 o'clock. Four collisions points were originally instrumented. BRAHMS and PHOBOS are two smaller special-purpose detectors which have completed their physics goals and are now dismantled. Two larger detector, STAR and PHENIX, are still active and located at 6 and 8 o'clock respectively (Figure 2.1).

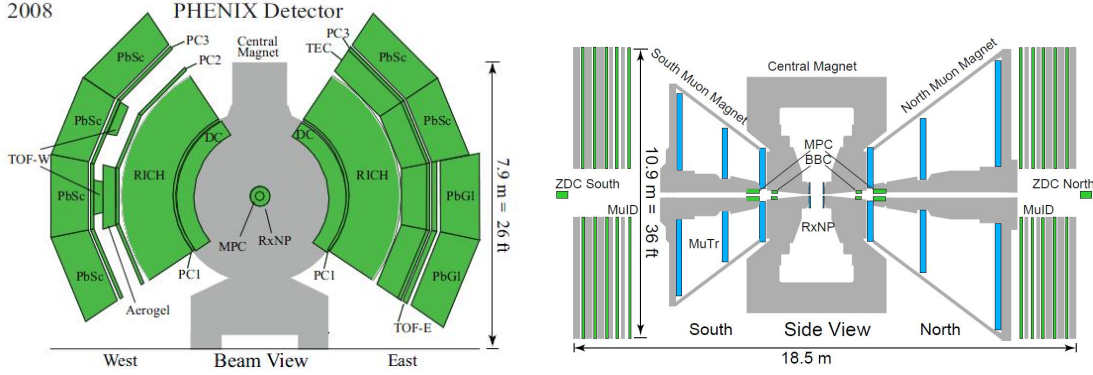


Figure 2.2: Top view and front view of PHENIX detectors

2.1.5 PHENIX

The Pioneering High Energy Nuclear Interaction eXperiment (PHENIX) is being carried out by a collaboration of about 650 physicists and engineers from 69 participating institutions in 14 countries. The PHENIX detector consists of a collection of detectors, which are grouped into two central arms and two muon arms. Two central arms measure photons and electrons, and two muon arms measure muons. There are also additional event characterization detectors that provide additional information about a collision, and a set of three huge magnets that bend the trajectories of the charged particles. Figure 2.2 shows PHENIX detector components of 2008 when the Υ and χ_c analysis was performed. Currently, PHENIX upgrade project is ongoing. So RPCs and (F)VTX detector is installed or will be installed soon. Among these PHENIX detectors, Muon arms and Muon Piston Calorimeters(MPCs) are used for the Υ and χ_c analysis.

2.2 PHENIX Central Arm

The central detectors are used to reconstruct identified charged particles, direct photons and neutral hadrons at mid-rapidity ($|\eta| < 0.35$). They are composed of a magnet system, a drift chamber, two flavors of time of flight detectors, three layers of multi-wire proportional chambers with pad readout (Pad Chamber, PC1,2,3), an aerogel Cerenkov detector, a time expansion chamber, a ring imaging Cerenkov detector (RICH) and an electromagnetic calorimeter(EMC) [54][55][56]. The electromagnetic calorimeter (EMC) is divided into eight sectors: six sectors are Lead-Scintillator sampling calorimeters (PbSc), and two sectors are Lead Glass homogeneous calorimeters (PbGl). A sector of the lead scintillator (lead glass) is composed of a grid of 72 by 36 (96 by 48) towers in the z and y coordinate of PHENIX where each tower covers approximately $0.01 \times$

0.01 (0.008×0.008) in $\Delta\eta\Delta\phi$ space. The calorimeters are described in detail in the references [57][58][59].

2.3 PHENIX Muon arms

The muon arms are designed to measure muons and composed of North and South arms. The acceptance of Muon arm covers $1.2 < |\eta| < 2.2$. A particle in the muon arm acceptance traverses five elements of the PHENIX detector, two of which produce analyzable data. First, the muons pass through the Central Magnet. Next they enter a radial magnetic field set up by the muon magnet system. Three stations of cathode strip chambers(Muon Tracker, Mutr) measure the muon deflection to reconstruct momenta and charge-sign. Lastly the muons traverse five layers of steel walls and stacked Iarocci tubes(Muon Identifier, MuID). Only muons with energy above 2.7 GeV have the penetrating power to reach the last layer of the Muon Identifier, so it is used to both identify muons and provide a fast trigger.

2.3.1 The muon tracker detector

The muon tracker detector (Mutr), with its spatial resolution of about $100 \mu\text{m}$, corresponding to the relative mass resolution of about $\sigma(M)/M = 6\%/\sqrt{M}$, provides the ability for separation of the ρ/ω and ϕ peak from J/ψ and Υ . The Mutr, which is placed inside the muon magnet frame, as illustrated in Figure 2.3 , consists of three octant-shaped stations of tracking chambers with cathode-strip readout. The numbering convention of the MuTR stations is illustrated on Figure 2.4. Stations 1 and 2 consist of three layers ("gaps") and Station 3 composed from 2 layers ("gaps"). Each gap consists of the plane of almost azimuthally running anode wires, which is between two planes with 1 mm wide cathode strips. Only cathode strips are read out. In the first plane the cathode strips run radially, exactly perpendicular to the anode wires. In the second plane, the cathode strips are positioned at the stereo angles within 11.5° with respect to the perpendicular strips. This specific configuration of strips results in a position resolution of $100 \mu\text{m}$. The MuTR chambers are operated with a 50 : 30 : 20 (non-flammable) gas mixture of Ar : CO₂ : CF₄ at a typical voltage of 1850 V on the anode wires. The momentum of a charged particle traversing the MuTR is measured using the bend in its trajectory (sagitta) due to the influence of the magnetic field. According to the Lorentz law only the perpendicular component of the velocity vector is affected by the magnetic force, therefore the bend in trajectory is in the perpendicular direction with respect to the magnetic field. The momentum of the track can be calculated from the following formula:

$$p = q \times B \times R \quad (2.1)$$

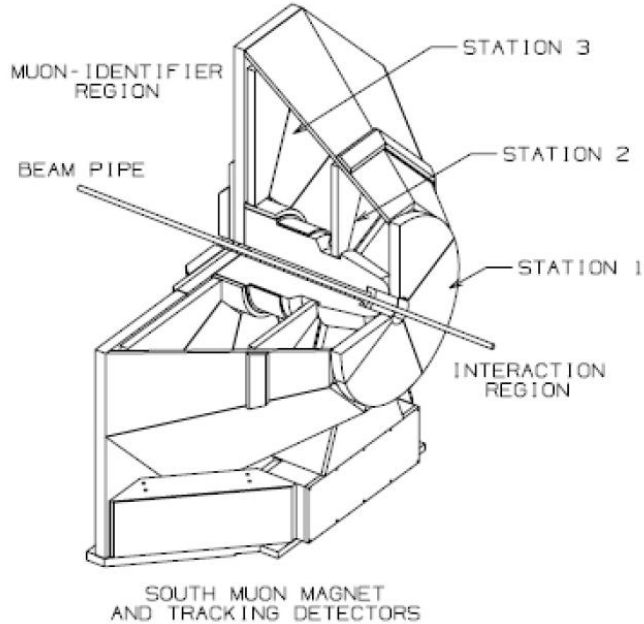


Figure 2.3: Drawing of the South muon arm tracking spectrometer.

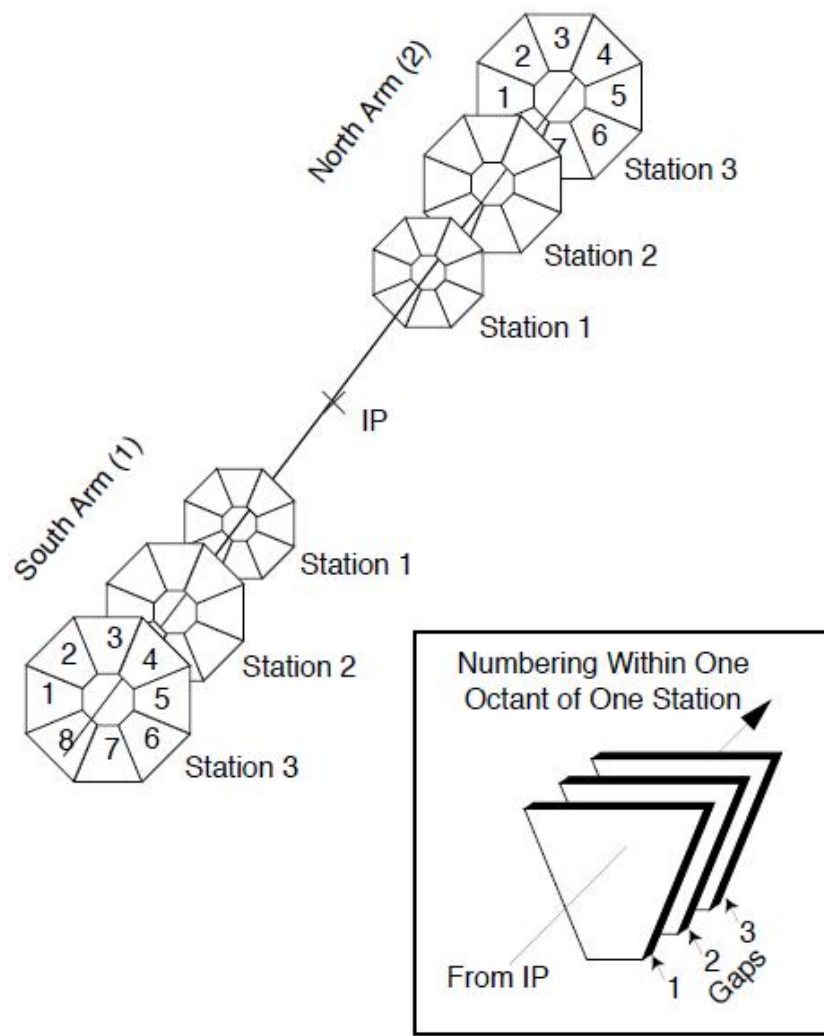
where q is the charge of the track, B is the strength of the magnetic field, and R is the radius of the "bent" trajectory, which is determined from measuring track coordinates in all three stations. Although the magnets between the arms are different (1.5 m shorter in the south arm), they are operated to provide a similar $\int B dl$, which is about 0.75 Tm at the 15° polar angle. The detailed information about the operational principles and performance of the PHENIX magnets can be found in [60].

2.3.2 The muon identifier detector

The main purpose of the muon identifier (MuID) is to significantly reduce the hadronic background in the muon arms. This is primarily achieved by optimizing the size, segmentation and placement of the absorber material which is the integral part of the muon spectrometers. Muons traversing through the absorber material lose a constant amount of their energy at every step, $-dE/dx$, mainly due to the ionization energy loss [61]. On the other hand, hadrons also experience strong interactions inside the absorber, which cause a complete or significant energy degradation. As a result, the initial hadron flux decreases inside the absorber depending on the penetration depth.

The placement of the multiple layers of the entire absorber material in the muon arms along the z-axis is schematically drawn on Figure 2.5. Particles produced at the

Muon Tracking Nomenclature



W. Kimball, 8/1987

Figure 2.4: Pictorial illustration of the numbering scheme of the MuTR stations

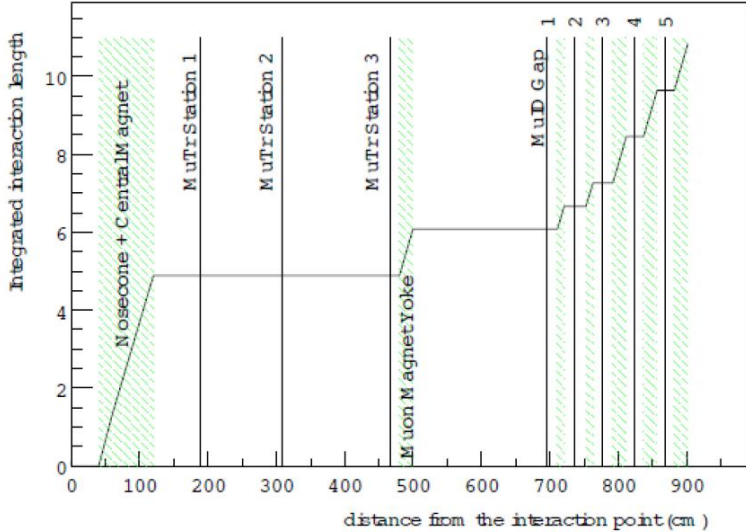


Figure 2.5: Locations of the absorbers and active layers of the muon detectors along the z-axis from the interaction point in the south arm.

interaction point first encounter the "nosecone" absorber situated before Station 1 of the MuTR. It is about 80 cm thick, which translates into $\sim \lambda_I$ of integrated nuclear interaction length. The second absorber layer, called the muon magnet backplate, is 30 cm wide in north arm and 20 cm wide in south arm. It is located immediately after the muon tracker, and followed by the four layers of the MuID absorbers of thicknesses 10, 10, 20, 20 cm. The particular finer segmentation of the first two MuID absorbers was designed to enhance the acceptance for detecting ϕ mesons. While the vast majority of hadrons produced at the interaction point are expected to be absorbed by the absorber material, there still remains an irreducible background due to weak decays into muons (μ/π ratio of 1×10^{-3}), which is fixed by the proximity of the nearest absorber. Five active layers, referred to as "gaps", of the MuID detector are created by the specific segmentation of the absorber. The gaps are numbered from 0 to 4 in the direction away from the interaction point. The conventional limited steamer tubes of the Iarocci type, referred to as "Iarocci tubes", were selected as the MuID detector technology. The Iarocci tubes, illustrated in Figure 2.6, are 8.35 cm wide, 1.3 cm high, and can be up to 2 m long. Each tube is subdivided into eight 9×9 mm channels consisting of $100 \mu\text{m}$ CuBe anode wires placed inside the graphite-coated plastic cathode case. To increase detection efficiency Iarocci tubes are paired up to form two-packs. Tubes are fixed with a half cell offset with respect to each other. A non-flammable gas mixture of isobutane 8.5 % + CO_2 91.5 % is used inside the MuID. The Iarocci tubes are operated in the proportional mode, at 4500 V, to minimize the aging effects. Each MuID gap is composed of six panels

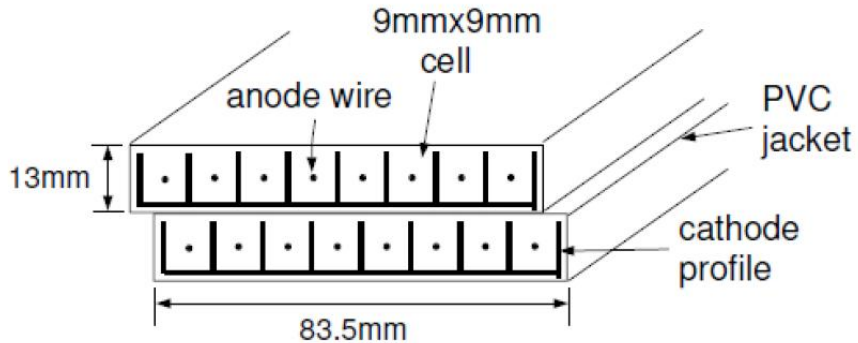


Figure 2.6: Cross section of a two-pack assembled from Iarocci tubes

placed around the square hole left for the beampipe to pass through, as illustrated on Figure 2.7. Each panel consists of two layers of horizontally and vertically oriented two-packs, which provides 8.4 cm granularity along the x and y coordinates. If a traversing track deposits enough energy through the ionization energy loss in each two-pack, a "hit" will be registered. There are total number of 6140 two-packs in the MuID detectors.

2.4 Global Detectors

The global detectors include the Beam-beam counter (BBC), Zero Degree Calorimeter (ZDC) and the Reaction Plane Detector. The two BBC arms sit ± 144 cm from the nominal interaction point with a pseudorapidity coverage of $3.1 < |\eta| < 3.9$. Each arm is composed of 64 3-cm thick Cerenkov ($\beta_{threshold} = 0.7$) radiators read-out with mesh-dynode photomultiplier tubes. The time difference between each arm is used to reconstruct the collision point along the beamline. The sum gives the start time for time of flight measurements. The z-vertex reconstruction is done both online in the trigger and offline with better precision. The multiplicity of active towers and the online measurement of the z-vertex is used to construct a minimum-bias trigger, i.e. one which fires for a large fraction of collisions and selects inelastic collisions without a selection bias. The trigger fires so frequently that not all events are collected. In fact, it fired at about 100 kHz in 2008, and most of its events were not written to disk. However, minimum bias triggered events serve an important purpose. The other PHENIX triggers are designed to select and collect rare events while discarding as few as possible. They may introduce a measurement bias. Comparing an analysis done with the minimum bias triggered data sample and to an identical analysis done with a selectively triggered data sample reveals the trigger bias and can often be used to correct it.

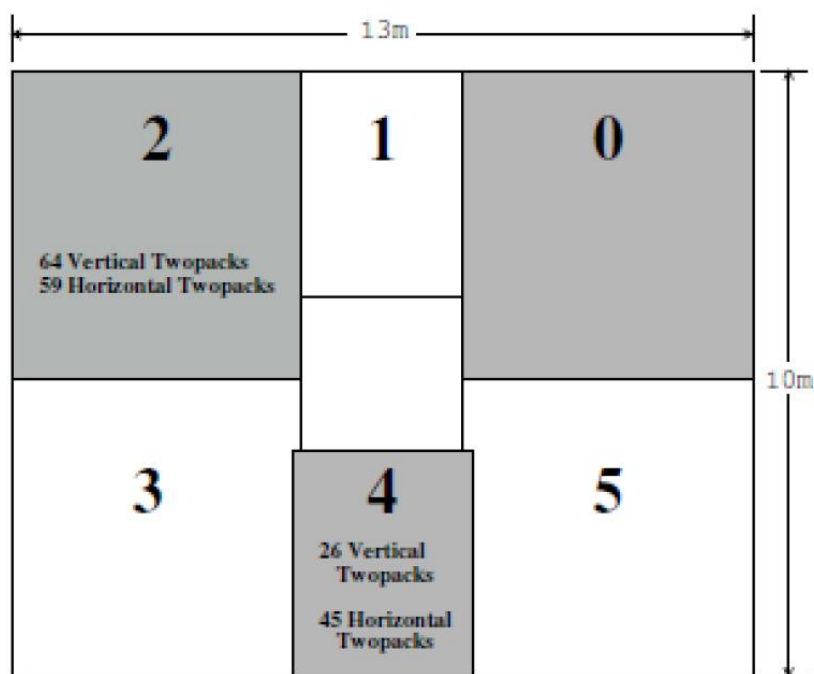


Figure 2.7: Schematic view of a MuID layer from the interaction point. The panels are numbered from 0 to 5 in the clockwise direction.

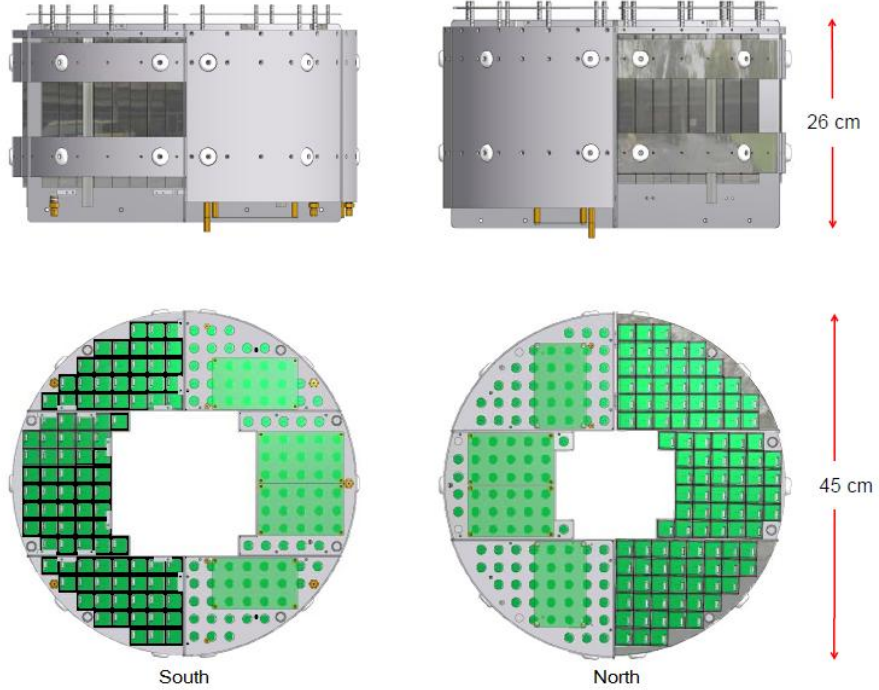


Figure 2.8: Top view and front view of South MPC and North MPC

2.5 PHENIX MPCs

2.5.1 General

Muon Piston Calorimeters(MPCs) are composed of 2 MPCs, one is in forward rapidity region (North arm) and the other one is in backward rapidity region (South arm). And they are located at 220 cm away from the nominal interaction point (Figure 2.2). North MPC has 220 crystals and South MPC has 196 crystals. Each MPC has diameter as 45 cm and thickness as 26 cm as shown at Figure 2.8. MPCs cover very forward rapidity range of $|3.1| < y < |3.8|$.

2.5.2 MPC cell

The calorimeter cell consists of two parts: scintillating crystal and avalanche photo-diode. High energy particles produce light in the crystal, and the avalanche photo-diode is used to measure its intensity (Figure 2.9). Since MPCs are located near the beam pipe, they need high density material. So the crystal is made of PbWO_4 which has short

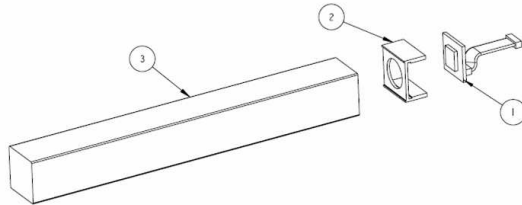


Figure 2.9: MPC Tower Assembly: 1) Crystal, 2) APD Holder, 3) Avalanche Photodiode and preamp

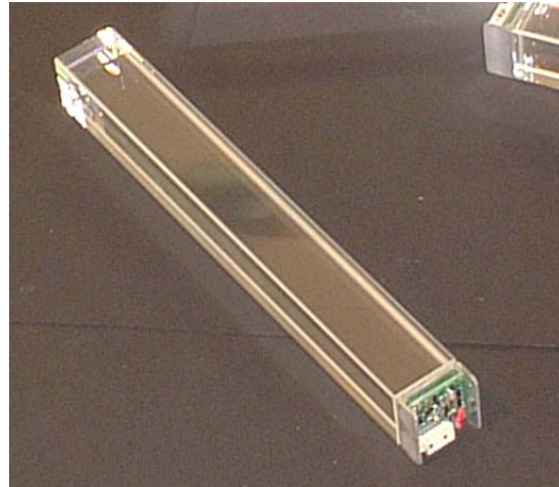


Figure 2.10: MPC crystal which is made of $PbWO_4$.

radiation length and small Moliere Radius, which is defined as the radius of a cylinder which contain 90 % of the shower's energy (Figure 2.10). Table 2.1 shows the properties of the crystal. The dominant interaction between high energy ($> 20 \text{ MeV}$) photons and electrons with the crystals is pair-production and bremsstrahlung.

Index	Values
Size	$2.2 \times 2.2 \times 18\text{cm}^3$
Density	8.28 g/cm^3
Moliere Radius	2.0 cm
Radiation Length	0.89 cm
Interaction Length	22.4 cm
Hardness	4 Moh
Refractive index($\lambda=632\text{nm}$)	2.16
Main emisson lines	420, 480-520 nm
Temperature Coefficient	$-2\%/\text{ }^\circ\text{C}$
Radiation Hardness	1000 Gy

Table 2.1: PbWO_4 Properties

Chapter 3

Data Analysis 1 - Υ measurement at $p + p$ and $d + \text{Au}$ Collisions

3.1 Data set, Quality Assurance Good Run list

3.1.1 Quality Assurance, Good Runlist and Data Set

Quality Assurance was performed as listed below. The list also can be checked in the PHENIX wiki page of

<https://www.phenix.bnl.gov/WWW/offline/wikioffline/index.php/Run8dAuDimuon>

Besides the QA, additional bad runs were identified by looking for dead HV channels in the HV monitoring. These bad runs cause severe discrepancies between the MC representation of the detector and the real detector. The good runs for Run6pp was taken from AN 636 which has Run6pp QAs.

Table 3.1 shows the number of minimum bias events from BBC live conunts and integrated luminosity. Integrated luminosity is calculated using the fomulae below.

$$\text{Luminosity} = \frac{N_{MB}^{BBC}}{\sigma_{BBC}} \quad (3.1)$$

$$\sigma_{BBC} = \sigma_{Total} \times \varepsilon_{BBC} \quad (3.2)$$

where, for dAu collision system, $\sigma_{Total}^{dAu} = 2.26 \text{ b}$ is the total cross section which was taken from Sebastian White's dAu dissociation cross section measurement for MB normalization of AN 385. $\varepsilon_{BBC}^{dAu} = 0.88$ is the BBC Min. Bias efficiency of which value is taken from AN 396. Similarly, $\sigma_{Total}^{pp} = 42.2 \text{ mb}$ and $\varepsilon_{BBC}^{pp} = 0.545$ is used for pp collision system.

Dataset	Runs analyzed	N_{MB}^{BBC}	Luminosity
Run6pp South	548	1.721e+11	7.5pb^{-1}
Run6pp North	571	1.793e+11	7.8pb^{-1}
Run8dAu South	697	1.326e+11	67nb^{-1}
Run8dAu North	711	1.365e+11	69nb^{-1}

Table 3.1: BBC MB Event and Luminosity of Run6pp and Run8dAu

Cut Name	Run6pp	Run8dAu
BBC z-vertex range	$ Z_{vtx} < 30\text{cm}$	$ Z_{vtx} < 30\text{cm}$
DG0 North/South	20/16	20/16
DDG0 North/South	9/9	9/9
MUTR χ^2	23.0	23.0
Vertex match χ^2	9.0	9.0
Rapidity	$1.2 < y < 2.2$	$1.2 < y < 2.2$
MUID LL1	2D trigger	2D trigger

Table 3.2: Cut conditions for Run6pp and Run8dAu. Cut conditions for Υ are basically the same as the J/ψ analysis from AN 794

3.1.2 Cut conditions

We applied basic dimuon cuts which are common to Run6pp and Run8dAu J/ψ analysis of AN 794 as seen in Table 3.2. To check the cut settings and flags, one can find the macros in CVS:

```
offline/packages/DimuonMixer/DimuonCutterRun6pp.C
offline/packages/DimuonMixer/DimuonCutterRun8dAu.C
```

3.2 Data Analysis

3.2.1 Analysis code and output

We used Dimuon mixer to mix the dimuon events. The location in CVS is

```
offline/packages/DimuonMixer
```

Analysis train 175 was used to get the analysis output which contains the likesign event, the mixed event and the unlikesign event. The macros for train riding are in CVS:

```
offline/AnalysisTrain/pat/macro/Run_run8dAu_dimuon.C  
offline/AnalysisTrain/pat/macro/Run_run6pp_dimuon.C
```

3.2.2 Combinatorial background subtraction

After getting analysis train output, one need to estimate and exclude the combinatorial background. To exclude the combinatorial background, there are two resonable ways. One is the likesign subtraction method and the other one is the mixed event subtraction method.

Likesign event subtraction method

The likesign event is thought to retain some correlations from jets, such as muons from decayed hadrons or punch-through hadrons. So we might exclude that kind of correlations from the unlikesign foreground by the likesign event subtraction method. But the likesign events have large fluctuations, especially in the high mass range of the Υ where there are far fewer statistics. The low statistics of the likesign events seems to distort the Υ signal. Figure 3.1 is the ratio of the likesign event over the scaled mixed event. Figure 3.2 is the mass distribution from the likesign event subtraction.

For this analysis, we applied the mixed event subtraction method since the mixed events have fewer fluctuation than the likesign events, which is crucial in this analysis, and we do not see evidence for any difference between the shapes of the likesign and mixed event backgrounds.

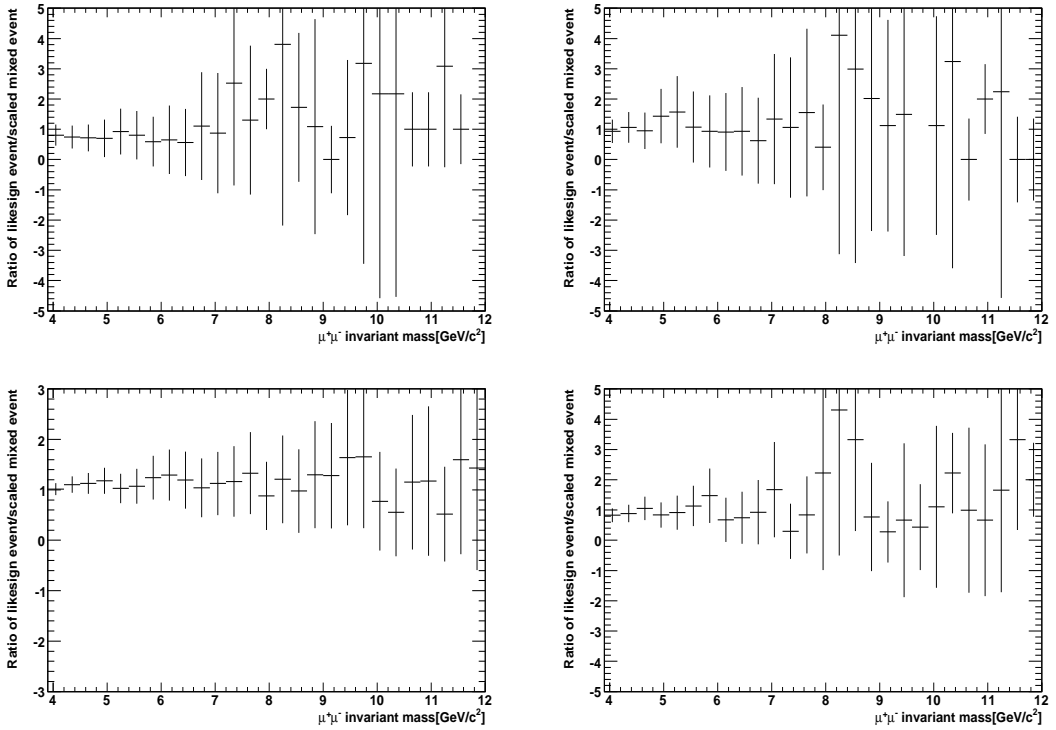


Figure 3.1: Ratio of the likesign event over the scaled mixed event of Run6pp (top row) and Run8dAu (bottom row) dataset. Likesign event has large fluctuation especially for high mass region. The low statistics of the likesign sample results in difficulties in the Υ signal extraction.

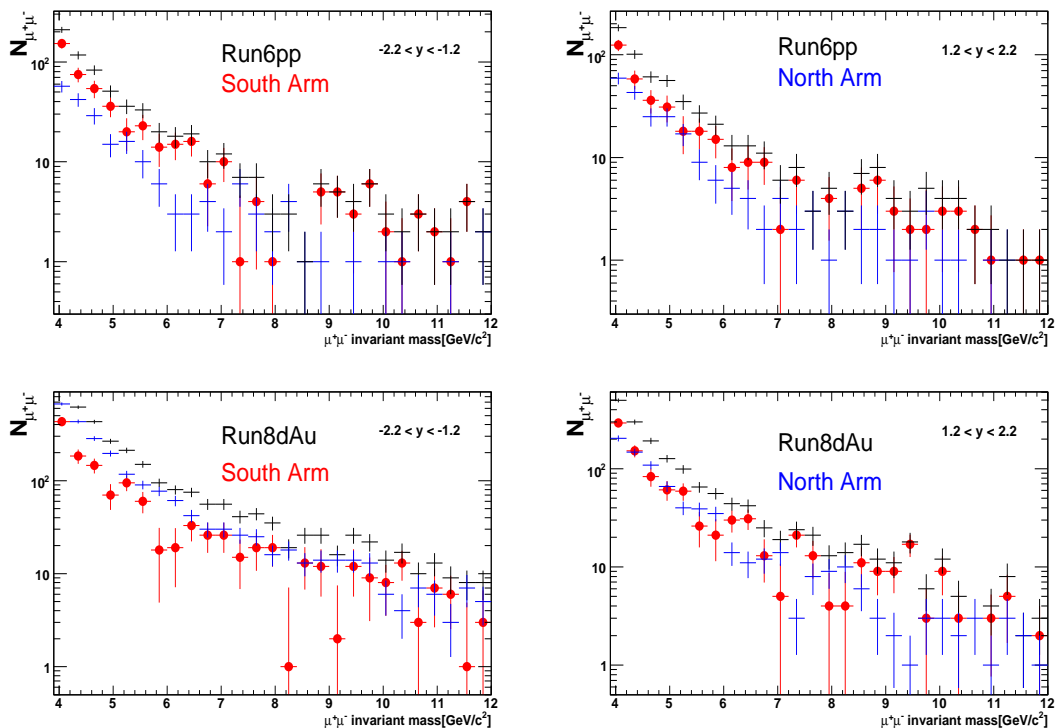


Figure 3.2: High mass region distribution of Run6pp and Run8dAu dataset by the likesign event subtraction method. Black cross stands for the unlikesign foreground and blue cross is the likesign event. Red point is the subtracted signal that is black cross - blue cross.

Mixed event subtraction method

In the event mixing subtraction method, the normalization factor was calculated as below

$$\text{Normalization Factor} = \frac{2 \times \sqrt{FG_{++} \times FG_{--}}}{BG_{+-}} \quad (3.3)$$

Here, BG_{+-} stands for the number of the unlikesign mixed event background. FG_{++} and FG_{--} represent the number of the likesign foreground. By multiplying this *NormalizationFactor* to the mixed event, one can scale down the mixed event to the level of the like sign foreground. Moreover, the scaled mixed event is expected to have fewer fluctuation than the likesign foreground since the scaled mixed event is scaled down from higher statistics than the likesign event. Afterwards, the scaled mixed event is subtracted from the unlike sign foreground. Normalization range is from 1.7 GeV to 16 GeV. Figure 3.3 shows the subtracted events of Run6pp and Run8dAu.

3.2.3 Residual background estimation

The subtracted event is considered as the Υ signal with residual background from Drell Yan, correlated open bottom and correlated open charm. Thus one has to be careful to estimate the residual background. For this analysis, we simulated Drell Yan, correlated open bottom and correlated open charm based on Drell Yan, open bottom and open charm 4π cross sections of PHENIX Preliminary result and Run6pp, Run8dAu luminosities of Table 3.1. You can see the details of the simulation in Section 3.5.

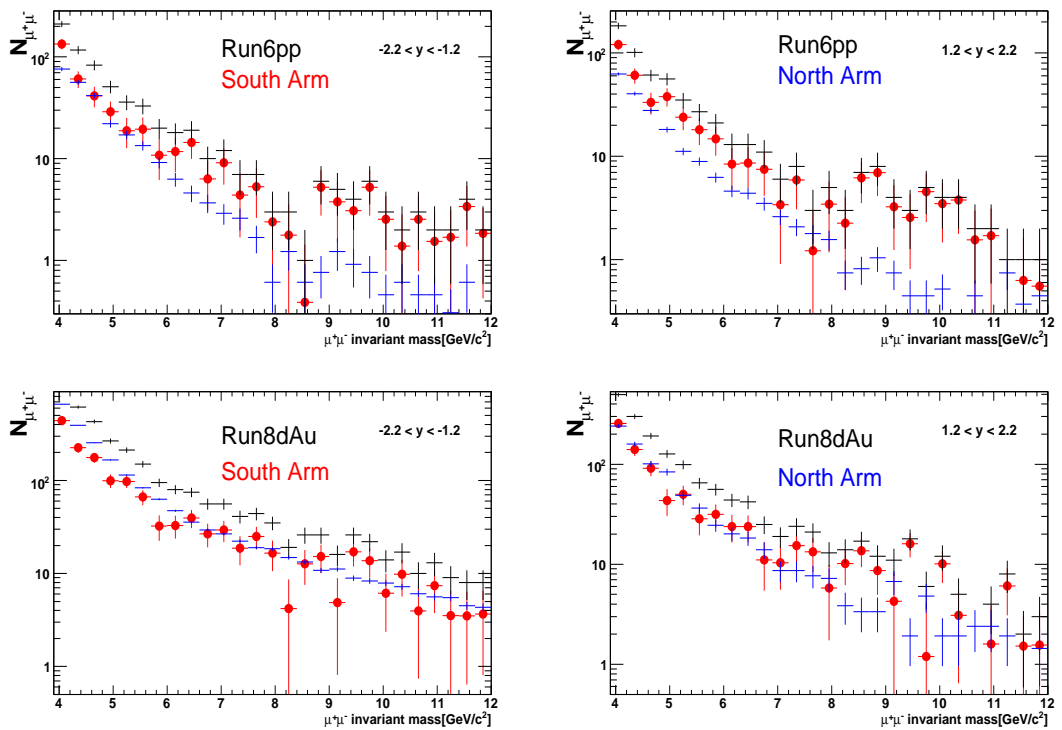


Figure 3.3: High mass region distribution of Run6pp and Run8dAu dataset by the mixed event subtraction method. Black cross stands for the unlike sign foreground and blue cross stands for the scaled mixed background. Red point is the subtracted signal that is black cross - blue cross

3.3 Υ simulation

3.3.1 Simulation setup and procedure

Υ generation

PHPythia generator was used to generate three states of Υ , Υ_{1S} , Υ_{2S} and Υ_{3S} . PHPythia, Trigger and Particle selector of PHPythia generator are in CVS:

```
event_gen/src/PHPythia
event_gen/src/PHPythia/Triggers
event_gen/src/PHPythia/ParticleSelection
```

One can set a trigger to the PHPythia events which require that the Υ decays into a muon pair with both muons into the muon arm acceptance. Besides, ParticleSelector make the generator write out only the selected particles. Specifically, for Υ events, only the Υ decay muon pairs are selected. These give an advantage to save the simulation time and disk space.

Simulation parameters

Unfortunately, there is no direct way to generate Υ_{3S} state. So we just used Υ_{1S} state generation method changing the mass of Υ_{1S} state to the mass of Υ_{3S} state. That can be done in pythia simulation card by adding the line of

```
pmas 553 1 10.3552
```

that means changing Υ_{1S} mass to 10.3552 of Υ_{3S} mass. The simulation card for the Υ_{1S} state is shown at Table 3.3. Cards for Υ_{2S} and Υ_{3S} are similar with the one of Υ_{1S} . These cards are also available in CVS:

```
event_gen/src/pythia_muons/pythia_upsilon_1s.cfg
event_gen/src/pythia_muons/pythia_upsilon_2s.cfg
event_gen/src/pythia_muons/pythia_upsilon_3s.cfg
```

And the detailed description for the pythia setting can be obtain in the official pythia manual

<http://home.hep.lu.se/~torbjorn/pythia/lutp0613man2.pdf>

Parameters	Index1	Index2	Setting	Meaning
msel			0	turn off all production mechanisms manually
msub	86		1	turn on $g + g \rightarrow J/\psi + g$
msub	106		1	turn on $g + g \rightarrow J/\psi + \gamma$
msub	107		1	turn on $g + \gamma \rightarrow J/\psi + g$
msub	108		1	turn on $\gamma + \gamma \rightarrow J/\psi + \gamma$
kfpr	86	1	553	request Υ_{1S} instead of J/ψ of msel 86
kfpr	106	1	553	request Υ_{1S} instead of J/ψ of msel 106
kfpr	107	1	553	request Υ_{1S} instead of J/ψ of msel 107
kfpr	108	1	553	request Υ_{1S} instead of J/ψ of msel 108
mdme	1034	1	0	turn off $\Upsilon_{1S} \rightarrow e^+e^-$
mdme	1035	1	1	turn on $\Upsilon_{1S} \rightarrow \mu^+\mu^-$
mdme	1036	1	0	turn off $\Upsilon_{1S} \rightarrow \tau^+\tau^-$
mdme	1037	1	0	turn off $\Upsilon_{1S} \rightarrow dd$
mdme	1038	1	0	turn off $\Upsilon_{1S} \rightarrow uu$
mdme	1039	1	0	turn off $\Upsilon_{1S} \rightarrow ss$
mdme	1040	1	0	turn off $\Upsilon_{1S} \rightarrow cc$
mdme	1041	1	0	turn off $\Upsilon_{1S} \rightarrow ggg$
mdme	1042	1	0	turn off $\Upsilon_{1S} \rightarrow \gamma gg$
mdme	858	1	0	turn off $J/\psi \rightarrow e^+e^-$
mdme	859	1	1	turn on $J/\psi \rightarrow \mu^+\mu^-$
mdme	860	1	0	turn off $J/\psi \rightarrow \text{random flavor}$
mstp	51		7	select PDF of CTEQ5L

Table 3.3: Simulation parameters for Υ_{1S} generation.

Υ states	South arm	North arm
Υ_{1S}	520 MeV	410 MeV
Υ_{2S}	580 MeV	450 MeV
Υ_{3S}	610 MeV	480 MeV

Table 3.4: Simulated mass resolutions for three states of Υ .

3.3.2 Υ mass resolution

The generated three states of Υ are run through the PISA simulation chain. Figure 3.3.2 and Figure 3.5 show the each state of reconstructed Υ and Υ_{Family} . Table 3.4 shows the reconstructed Υ mass resolution. Some experimental aspects might affect the Υ mass resolution in the real data. One effect is the position resolution and alignment errors which have been discussed in AN 401. This effect is not a big deal for J/ψ mass resolution since the J/ψ decay muon experiences multiple scattering so the geometrical effect might be smeared out by the absorber. On the other hand, Υ decay muons have higher momenta than J/ψ decay muons. The Υ decay muon is thought not to have as much multiple scattering as from J/ψ 's, so that means the Υ mass resolution might be affected by the geometrical effect mainly.

For the difference of mass resolutions between South and North arm, geometrical issue or difference of $\int B dx$, which had been discussed in AN 401, might cause it.

But the real mass resolutions of the three states of the Υ are not measured precisely because of the low statistics of Υ . Thus, for the precise measurement, we need better detector performance and more Υ statistics than now. Thus, in this analysis, we assume the Υ mass resolution to be 600 MeV assigning a systematic uncertainty to the mass resolution. You can check Section 3.7 for this uncertainty assignment.

3.3.3 Composition of Υ family

Table 3.5 shows the composition ratio of Υ_{Family} from CDF and FNAL experiments. Their measurements are almost same. So we assume that Υ composition at RHIC follows the composition of CDF measurement. First, we generate three states of Υ and reconstruct those through the PISA simulation chain. Afterwards, we sum those following the ratio of CDF the measurement to compose the Υ_{Family} .

We assume the same composition of the Υ_{Family} for the real data that allows us three Gaussians for Υ fitting. Figure 3.2 is the simulated Υ_{Family} which is fitted by three Gaussians. That might be closer to the reality than assuming only one state of Υ , even

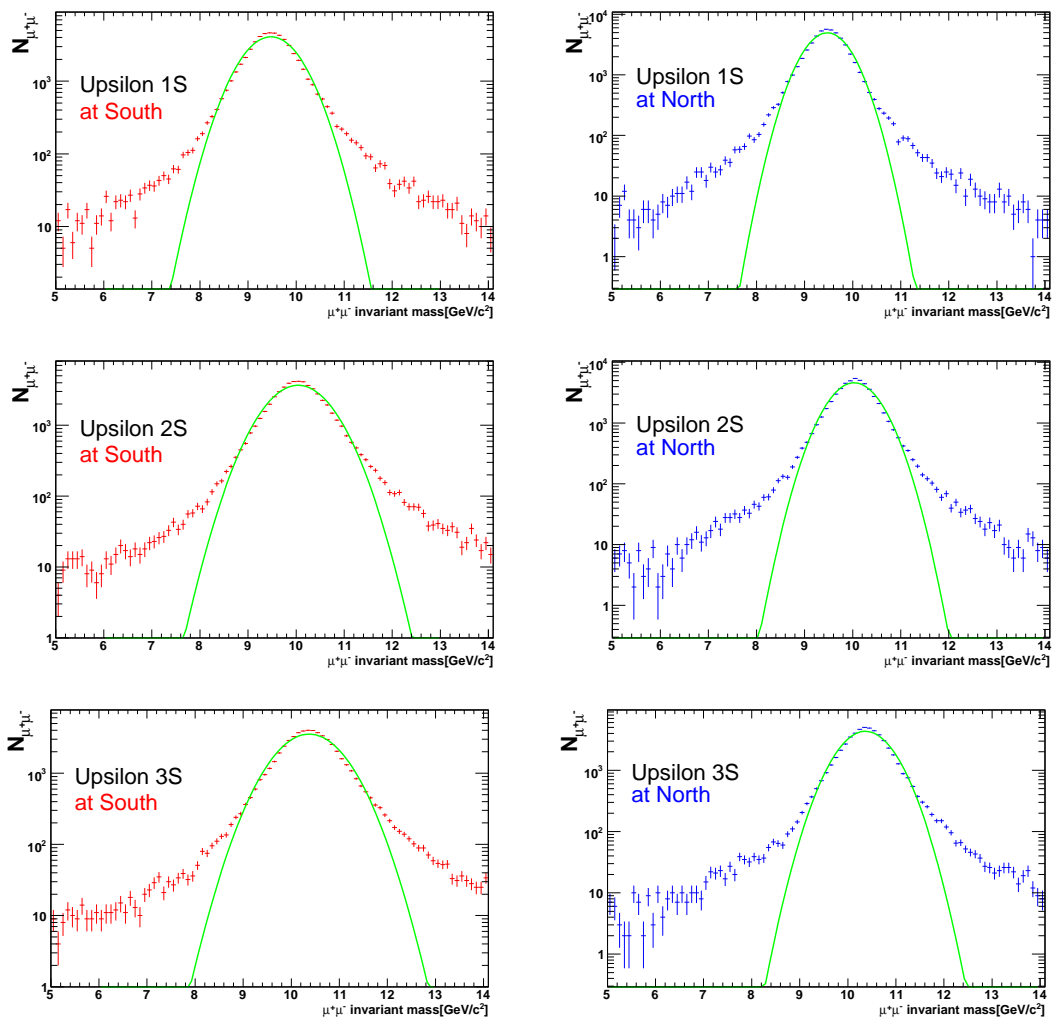


Figure 3.4: Simulated three states of Υ . Fitted by Gaussian for each of states.

Υ states	Mass	BR of $\Upsilon \rightarrow \mu^+ \mu^-$	CDF $\sqrt{S} = 1.8 TeV$	FNAL E605 $\sqrt{S} = 39 GeV$
Υ_{1S}	9.46	2.48	73%	72%
Υ_{2S}	10.02	1.93	17%	19%
Υ_{3S}	10.36	2.29	10%	9%

Table 3.5: Composition of Υ_{Family} at CDF and FNAL experiments.

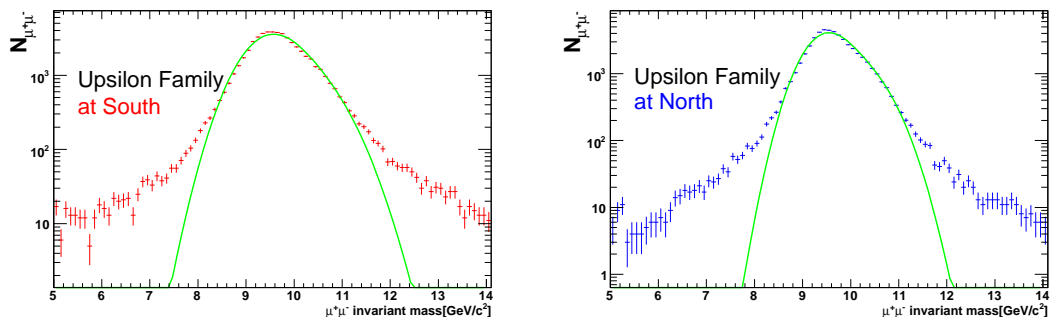


Figure 3.5: Simulated Υ_{Family} . Fitted by 3 Gaussians.

though the three states of the Υ can't be resolved clearly in this data set due to the poor mass resolution. In fact, this assumption fits the real data quite well. You can see Section 3.6 for details on the data fitting to the real data.

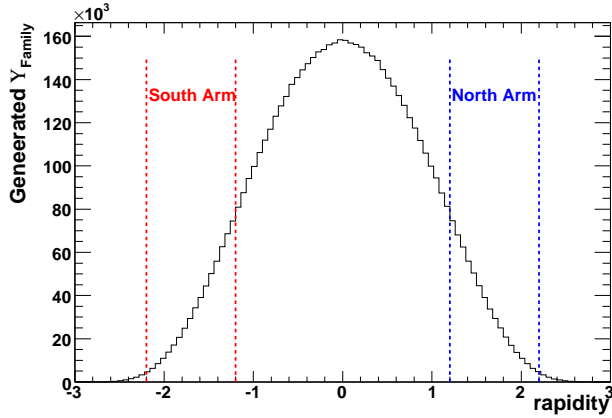


Figure 3.6: The generated Υ_{Family} by PHPythia generator. The dotted line represents the geometrical Muon arm acceptance. Reds for South, Blues for North.

3.4 Acceptance×efficiency calculation

PHPythia event generator and PISA simulation chain are used to calculate acceptance×efficiency of Υ . Υ is generated with same simulation parameters as Section 3.3. Afterwards, those are run through the PISA simulation chain. One difference between Run6pp and Run8dAu is the additional embedding step. We think that the embedding step, which embeds simulated pure Υ in real data, is needed in dAu collisions to make a more realistic environment, but it does not make a big difference for pp collisions since the multiplicity is not as high as dAu collision. Thus we include the embedding step additionally for Run8dAu estimation, but not for Run6pp estimation. This is consistent with what has been done previously for the J/ψ measurements. Besides that, we use the Υ_{family} , which is composed of three states of Υ for dAu collision. And we use just Υ_{1S} for pp collision. Actually, We found differences of acceptance×efficiency between three states was not big so it is negligible. Figure 3.7 shows the acceptance×efficiency values of each of the three states of Υ and Υ_{Family} at different rapidities. Those values for the three states of Υ and Υ_{Family} are quite similar with one another.

3.4.1 Run6pp Acceptance×efficiency calculation

Figure 3.6 shows the generated Υ of 4π acceptance. In principle, one can get the acceptance×efficiency by dividing the reconstructed Υ by the thrown Υ within the Muon arm acceptance. Table 3.6 includes the acceptance×efficiency calculation of Run6pp. That table includes the values for four rapidity bins per each arm. But for this analysis

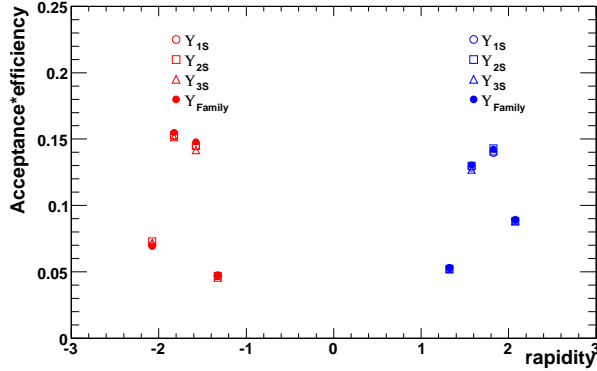


Figure 3.7: Acceptance \times Efficiency of each Υ and Υ_{Family} . Those values of three states of Υ and Υ_{Family} are quite similar with one another. Υ_{Family} is composed of Υ_{1S} , Υ_{2S} and Υ_{3S} following the ratio of 73 % : 17 % : 10 %.

we've used one inclusive bin from the four, one bin per each arm, since we don't have enough Υ statistics in the real data to get more points. That is a statistical limitation of the data, so just two rapidity bins are what can be analyzed for now.

For the reconstruction, same cuts and macros with real data reconstruction are used based on DimuonMixer except for a few minor things like the Level-1 trigger. That is, simulated data use the emulated Level-1 2 Deep trigger while real data use the real Level-1 2 Deep trigger. The reference run number is 194458.

3.4.2 Run8dAu Acceptance \times efficiency calculation

The same procedure as the Run6pp calculation is applied except for the additional embedding step. For the embedding step, we embed the simulated dst to the real dst from PRDFF and make the embedded ndst. For more dedicated simulation, we extract the vertex information from PRDFF and make a simulated Υ which has exactly same vertex information with real data and we also match the vertex while embedding to real data. That embedded ndst is run with DimuonMixer like real data. Table 3.7 shows the acceptance \times efficiency calculation. We used an inclusive two bins as in the Run6pp dataset. Reference run number is 250214.

Rapidity	Thrown Υ_{1S}	Reconstructed Υ_{1S}	Acceptance \times Efficiency
$[-2.2, -1.2]$	224328	24591.8 ± 156.818	0.1096 ± 0.0007
$[-1.45, -1.2]$	106679	6145.77 ± 78.3949	0.0576 ± 0.0007
$[-1.7, -1.45]$	67161	11180.3 ± 105.737	0.1665 ± 0.0016
$[-1.95, -1.7]$	35745	6096.3 ± 78.0788	0.1706 ± 0.0022
$[-2.2, -1.95]$	14743	1092.07 ± 33.0465	0.0741 ± 0.0022
$[1.2, 2.2]$	225202	25491.4 ± 159.66	0.1132 ± 0.0007
$[1.2, 1.45]$	107160	6177.92 ± 78.5998	0.0577 ± 0.0007
$[1.45, 1.7]$	67632	10620.9 ± 103.058	0.1570 ± 0.0015
$[1.7, 1.95]$	35675	6847.19 ± 82.7477	0.1919 ± 0.0023
$[1.95, 2.2]$	14735	1816.68 ± 42.6225	0.1233 ± 0.0029

Table 3.6: Acceptance \times Efficiency values of Υ_{1S} for Run6pp. Only two inclusive bins of top rows are used for this analysis.

Rapidity	Thrown Υ_{Family}	Reconstructed Υ_{Family}	Acceptance \times Efficiency
[-2.2, -1.2]	566398	55521.8 \pm 235.631	0.0980 \pm 0.0004
[-1.45, -1.2]	271646	13161.6 \pm 114.724	0.0485 \pm 0.0004
[-1.7, -1.45]	170812	25732.4 \pm 160.413	0.1506 \pm 0.0009
[-1.95, -1.7]	88557	14083.8 \pm 118.675	0.1590 \pm 0.0013
[-2.2, -1.95]	35383	2546.19 \pm 50.460	0.0720 \pm 0.0014
[1.2, 2.2]	563565	53542.6 \pm 231.393	0.0950 \pm 0.0004
[1.2, 1.45]	269834	14641 \pm 121.000	0.0543 \pm 0.0004
[1.45, 1.7]	169301	22601.6 \pm 150.338	0.1335 \pm 0.0009
[1.7, 1.95]	89032	13040.1 \pm 114.193	0.1465 \pm 0.0013
[1.95, 2.2]	35398	3299.06 \pm 57.438	0.0932 \pm 0.0016

Table 3.7: Acceptance \times Efficiency values of Υ_{Family} for Run8dAu. Υ_{Family} is composed of Υ_{1S} , Υ_{2S} and Υ_{3S} following the ratio of 73 % : 17 % : 10 %. Only two inclusive bins of top rows are used for this analysis.

Parameters	Index	Setting	Meaning
msel		11	Single W/Z production
ckin	1	3.5	set minimum mass value as 3.5 GeV
parp parp	91 31	1.5 1.1	set k_T value = 1.5 set k factor = 1.1
mstp mstp mstp	32 33 51	4 1 7	set Q_2 scale = 4 use k factor select PDF of CTEQ5L

Table 3.8: Drell Yan simulation parameters setting.

3.5 Drell Yan, Open Bottom and Open Charm estimation

Drell Yan, open bottom and open charm productions are thought to be a physical background in Υ mass region. Those are generated by PHPythia, and reconstructed thorough PISA simulation chain to consider detector response except random correlated Bottom, which is only estimated by randomization code. 4π cross section is assumed as $\sigma_{DY} = 42 \text{ nb}$, $\sigma_{b\bar{b}} = 3.7 \mu\text{b}$ and $\sigma_{c\bar{c}} = 567 \mu\text{b}$. Those numbers are extracted using the assumptions of PHENIX preliminary result.

3.5.1 Drell Yan estimation

Simulation parameters for Drell Yan

PHPythia simulation cards is shown at Table 3.8. Besides this setting, for the dedicated muon arm Υ study, minimum parton p_T setting is released while minimum parton mass is set to 3.5 GeV since we are interested in over 4 GeV up to Υ mass range to estimate the physical background of Υ .

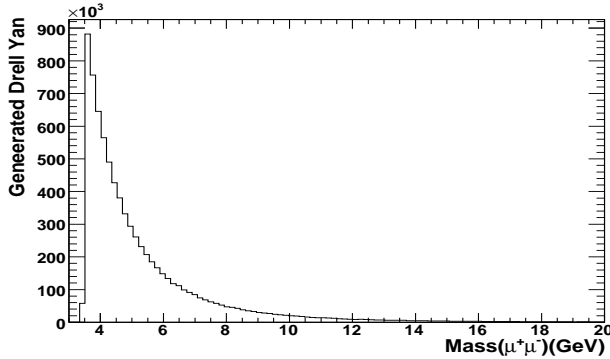


Figure 3.8: Generated Drell Yan with PHPythia. There is a mass cut which accepts above $m = 3.5$ GeV.

Drell Yan generation

PHPythia generator was used to generate Drell Yan event. For Run6pp estimation, Run6pp luminosity = 7.5 pb^{-1} for South arm, 7.8 pb^{-1} for North arm and $\sigma_{DY} = 42 \text{ nb}$ are assumed. For Run8dAu estimation, Run8dAu luminosity = 67 nb^{-1} for South, 69 nb^{-1} for North and $\sigma_{DY} = 42 \text{ nb} \times \text{number of nucleons} = 42 \text{ nb} \times 2 \times 197$ are assumed. Besides that, $\varepsilon_{BBC} = 0.79$ of pp collision and $\varepsilon_{BBC} = 0.97$ of dAu collision are also assumed, so the yields are scaled down by those ε_{BBC} s. As in the Υ generation, PHPythia Trigger and ParticleSelector are used, so only decay muons in muon arm acceptance are saved when they are generated. Figure 3.8 shows the generated Drell Yan by PHPythia.

Drell Yan reconstruction and getting fit function

Figure ?? shows the reconstructed Drell Yan production through PISA simulation chain for Run6pp and Run8dAu. For the dAu collision, additional embedding step is done as in the Υ simulation. An exponential function is used to fit the reconstructed Drell Yan. Fitting range is from 4 GeV to 12 GeV, which is same with real data's, so we get the shape and yield of Drell Yan from the exponential fit function.

3.5.2 Open bottom estimation

For open bottom estimation, two methods are considered. One is the correlated open bottom production which is obtained by pythia, and the other one is the uncorrelated open bottom production which is obtained by randomizing ϕ angle. Since we don't know

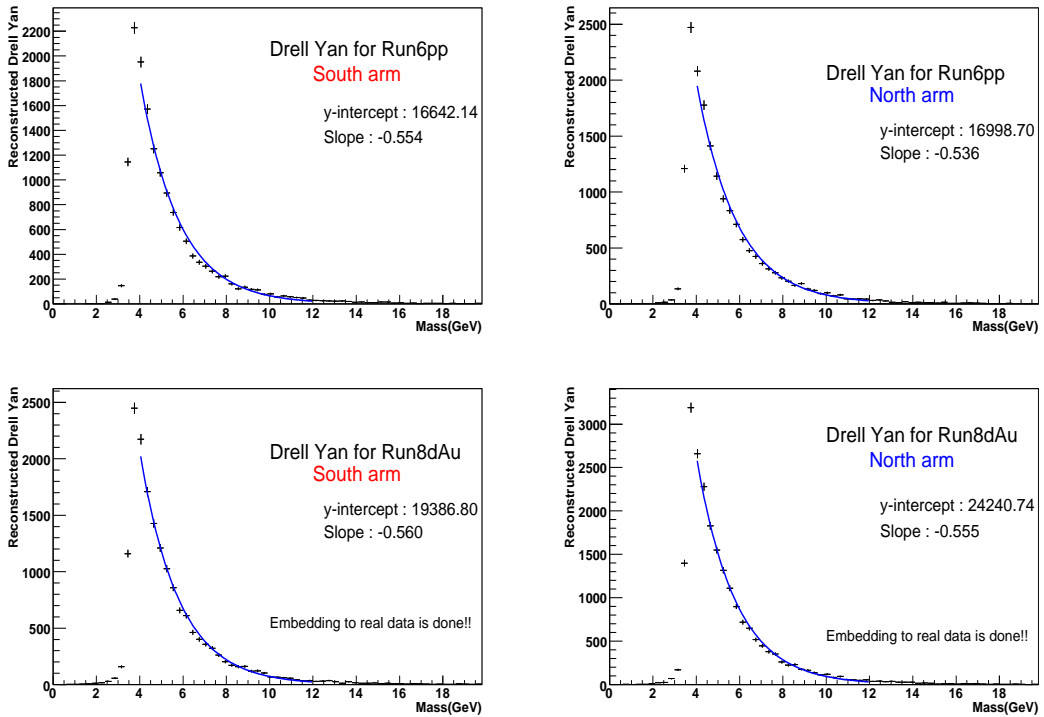


Figure 3.9: Reconstructed Drell Yan through PISA simulation chain with Run6pp and Run8dAu simulation configuration. Blue line is the fit function to get the shape. Reference runnumber is 194458 for pp and 250971 for dAu. Also, Embedding procedure is added for dAu estimation
dysimul1

Parameters	Index1	Index2	Setting	Meaning
msel			5	turn on bottom production of heavy flavor.
pmas	5	1	4.1	make bottom quark mass as 4.1 GeV
parp	91		1.5	set k_T value = 1.5
parp	31		3.4	set k factor = 3.4
mstp	32		4	set Q_2 scale = 4
mstp	33		1	use k factor
mstp	51		7	select PDF of CTEQ5L

Table 3.9: Simulation parameters setting for open bottom production.

the exact mechanism of real world, we think it is better to consider two possibilities separately. Afterwards, systematic uncertainty is assigned between the two possibilities.

Simulation parameters for the correlated open bottom

Simulation parameter cards is shown at Table 3.9.

Correlated open bottom generation

Luminosities of Run6pp and Run8dAu, $\sigma_{b\bar{b}} = 3.7 \mu b$, number of nucleons and ε_{BBC} are considered for dAu collision to estimate the correlated bottom, exactly as was done in the Drell Yan case. PHPythia was used to generate open bottom event. As in the Υ and Drell Yan generation, PHPythia Trigger and ParticleSelector are used to save disk space and simulation time. For the triggering, the event, which has the open bottom decay muon, was triggered whenever the muon pair goes into the muon arm acceptance.

Correlated open bottom reconstruction and getting the fit function

Figure 3.10 shows the reconstructed open bottom through PISA simulation chain with Run6pp and Run8dAu PISA configuration. Again, an exponential function is fit to

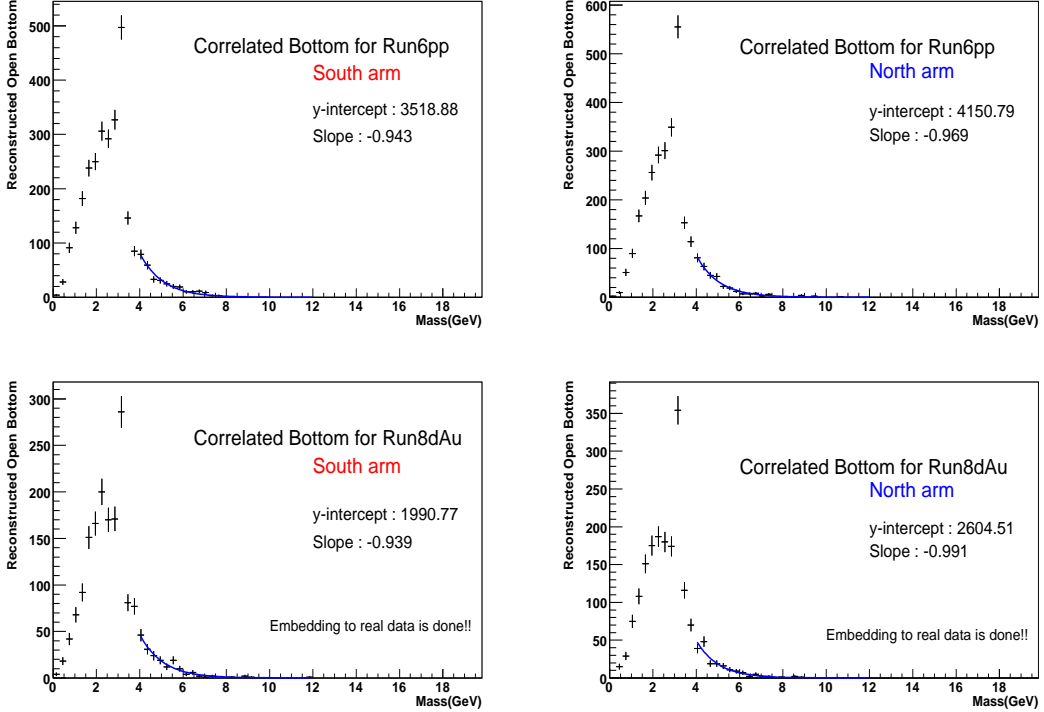


Figure 3.10: Reconstructed open bottom production through PISA simulation chain with Run6pp and Run8dAu simulation configuration. Blue line is the fit function to get the shape. Reference runnumber is 194458 for pp and 250971 for dAu. Also, Embedding procedure is added for dAu estimation

the reconstructed open bottom and the fitting range is from 4 GeV to 12 GeV. The embedding procedure is added for the Run8dAu estimation.

Uncorrelated open bottom estimation

To estimate the uncorrelated open bottom production, we sample p_T and rapidity distribution of bottom decay muon for muon arm using PHPythia. Figure 3.11 shows the p_T distribution of muon arm. Using that P_T distribution, we randomize ϕ angle and construct the uncorrelated mass keeping the rapidity shape of muon arm. Figure 3.12 shows the constructed mass. We extract the shape using exponential function.

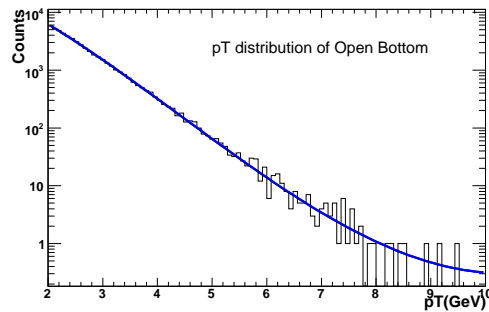


Figure 3.11: p_T distribution of bottom decay muon. Blue line is fit function to get the shape of distribution

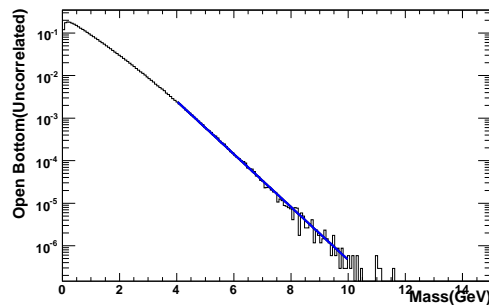


Figure 3.12: Uncorrelated mass construction. Blue line is fit function to get the shape of distribution

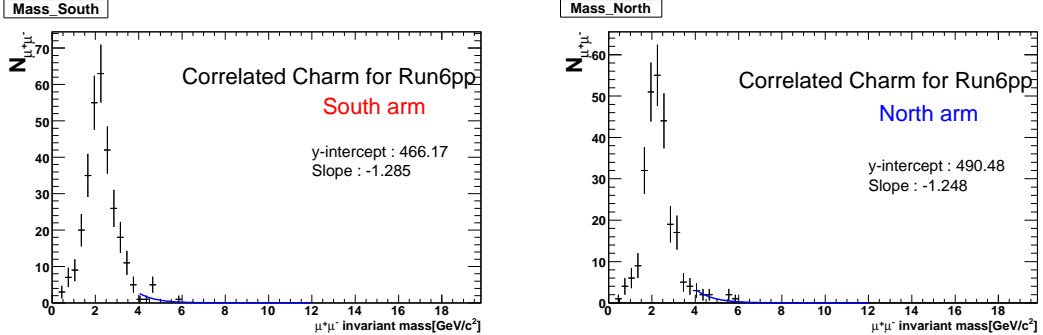


Figure 3.13: Reconstructed open charm production through PISA simulation chain with Run6pp simulation configuration. Blue line is the fit function to get the shape. Reference runnumber is 194458. Charm production turns out to be negligible for Υ estimation.

3.5.3 Open Charm estimation

We might need to estimate charm contribution since it might influence Drell Yan or correlated bottom estimation even though charm production doesn't affect Υ mass range directly. So, to estimate correlated charm, we did same procedure of open bottom simulation applying open charm cross section and open charm simulation card. For the open charm generation, we can change two lines of open bottom simulation setting as below

```
msel 4 (means trun on charm production)
pmas 4 1 1.25 (means set charm quark mass as 1.25 GeV)
```

But we don't add the embedding procedure for dAu collision estimation since the contribution of the correlated open charm is turned out to be negligible for Υ estimation. Figure 3.13 is the reconstructed open charm through PISA simulation chain.

3.6 Fitting real data

3.6.1 Fitting parameters and options

After subtracting combinatorial background as in Section 3.2, the combinatorial background subtracted signal is fit by Drell Yan, open bottom and open charm estimates as described in the previous section to figure out the residual background. When fitting to real data, the Drell Yan yield and open charm yield are constrained by $\pm 50\%$ from estimates taken from simulation. And open bottom yield is constrained by $\pm 100\%$. We assign the systematic uncertainty for slope variations of $+10\%$ and -10% from the simulation estimates for Drell Yan and correlated open bottom slope. Moreover, for open bottom we assign a systematic uncertainty for choosing the correlation types between the correlation got from pythia and random correlation. But we don't assign the systematic uncertainty for open charm since its contribution turns out to be negligible comparing to the other contributions. You can see the details of systematic uncertainty at Chapter 7

Three Gaussians are used for the three Υ states. The total Gaussian yield is not constrained, but the relative ratio of three states is fixed by the $73\% : 17\% : 10\%$ from the CDF measurement. Mean values of Υ_{1S} and Υ_{3S} are constrained by $\pm 10\%$ of simulated value, and the order of three states is set to be in order. Mass resolution is set to 600 MeV for three states commonly. As a result, we have a fitting function like Eq. 3.4 below.

$$F(x) = p_0 \exp(p_1 x) + p_2 \exp(p_3 x) + p_4 \exp(p_5 x) + \\ p_6 [(1.0 - p_9 - p_{12}) \exp(-0.5A^2) + p_9 \exp(-0.5B^2) + p_{12} \exp(-0.5C^2)], \quad (3.4)$$

where x = dimuon mass, $A = (x - p_7)/p_8$, $B = (x - p_{10})/p_{11}$, $C = (x - p_{13})/p_{14}$. The first term and second term of the fitting function corresponds to Drell Yan and open bottom estimation. Third term is for the open charm estimation. The rest are three Gaussians for the three states of Υ . Parameter settings are summarized in Table 3.10. The modified likelihood fit method is called from PostCabana Fitter class. That method fits the foreground by the scaled background plus fitting function. When the log-likelihood method is used, it is important to fit the foreground not the foreground minus scaled background since the log-likelihood method needs statistical error from the measurement. That is, we need to have the number of count of the foreground not the number of the difference between the number of the foreground and the scaled background. That also has the advantage to treat properly the empty bins, which have same number of foreground and scaled background. The macro for fitting is in CVS:

offline/analysis/

Fit parameters	Settings
p_0 (y axis intercept of Drell Yan) p_1 (slope of Drell Yan) p_2 (y axis intercept of Open Bottom) p_3 (slope of Open Bottom) p_4 (y axis intercept of Open Charm) p_5 (slope of Open Charm) p_6 (total magnitude of three Gaussians) p_7 (mean value of Υ_{1S}) p_8 (sigma of Υ_{1S}) p_9 (ratio of Υ_{2S}) p_{10} (mean value of Υ_{2S}) p_{11} (sigma of Υ_{2S}) p_{12} (ratio of Υ_{3S}) p_{13} (mean value of Υ_{3S}) p_{14} (sigma of Υ_{3S})	scaled simulation value $\pm 50\%$ constrained simulation value fixed scaled simulation value $\pm 100\%$ constrained simulation value fixed scaled simulation value $\pm 50\%$ constrained simulation value $\pm 10\%$ constrained set free simulation value $\pm 10\%$ 600 MeV(fixed) 0.17(fixed) between upper-limit of Υ_{1S} and lower-limit of Υ_{3S} 600 MeV(fixed) 0.10(fixed) simulation value $\pm 10\%$ 600 MeV(fixed)

Table 3.10: Fitting parameters for Υ fitting.

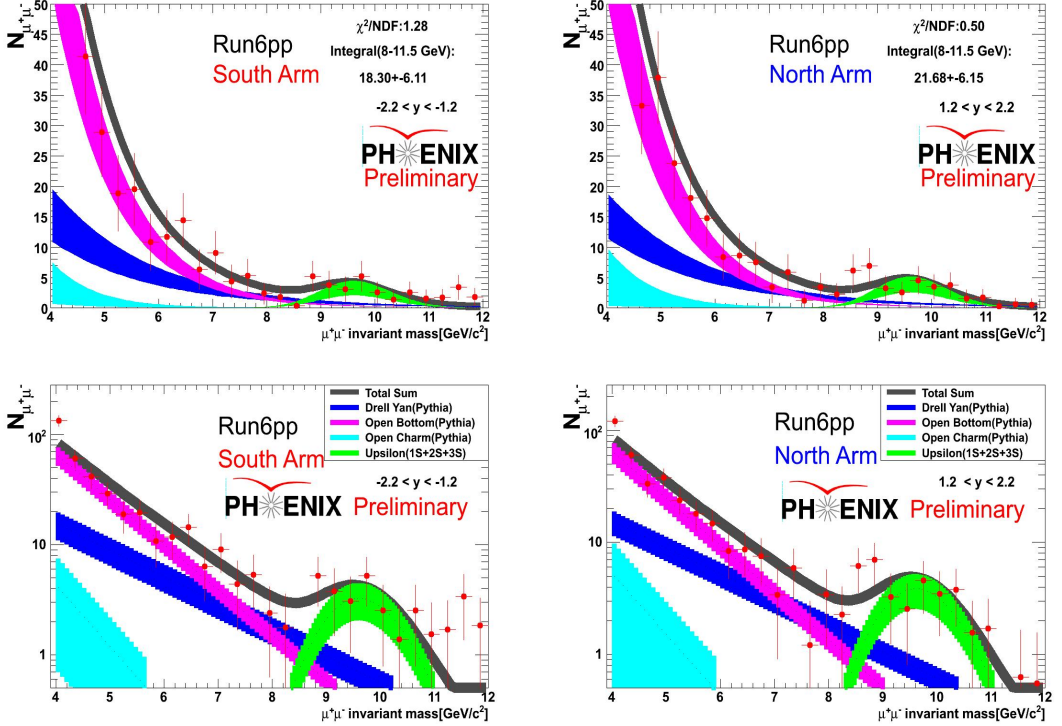


Figure 3.14: Run6pp Υ of North arm and South arm. Drell Yan, correlated open bottom and correlated open charm are considered to fit the physical background. Three Gaussians are used to fit Υ signal and exponential functions are used to fit Drell Yan, correlated bottom and correlated charm. Errorbands of fitting function include statistical and systematical uncertainties.

3.6.2 Fitting Run6pp and Run8dAu

Figure 3.14 and Figure 3.15 show the fitting results of Run6pp and Run8dAu dataset after subtracting the scaled mixed background. Table 3.11 and Table 3.12 show the raw integrals of Υ , Drell Yan, open bottom and open charm from fit functions for Run6pp and Run8dAu dataset, respectively.

Data sets	Υ Gaussians	Drell Yan	$b\bar{b}$	$c\bar{c}$
pp South	21.7 ± 6.2	7.6 ± 1.8	5.5 ± 0.7	0.1 ± 0.1
pp North	24.2 ± 6.7	9.5 ± 1.1	4.4 ± 0.7	0.1 ± 0.1

Table 3.11: Integrals of each components of Υ mass range in Run6pp.

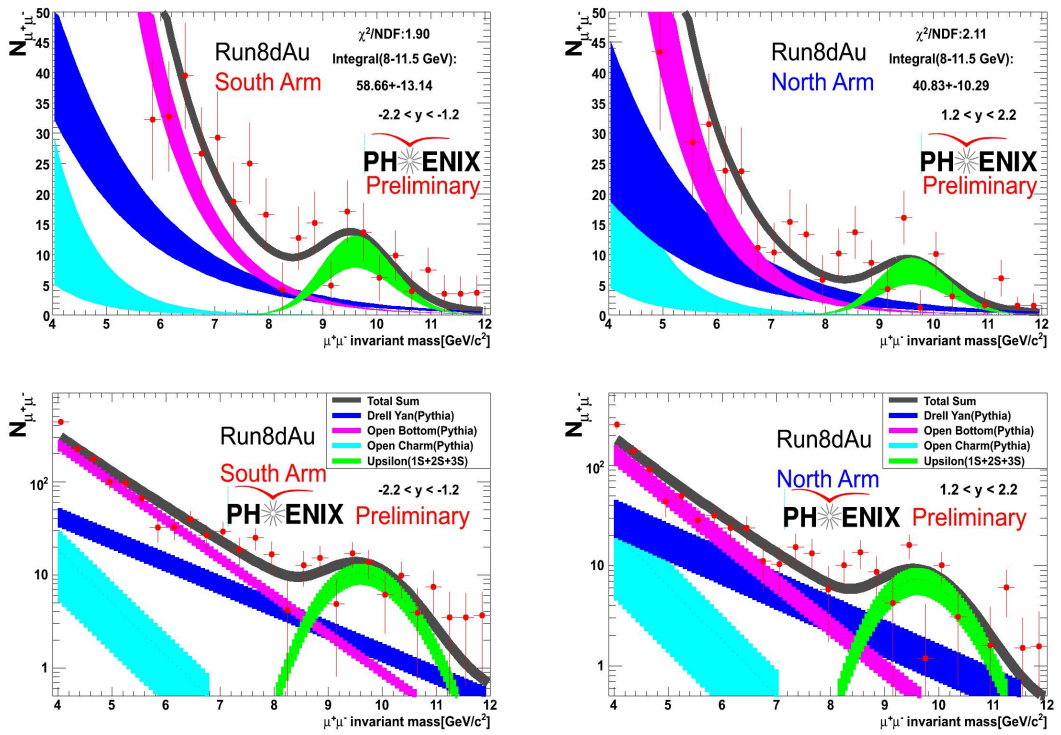


Figure 3.15: Run8dAu Υ of North arm and South arm. Drell Yan, correlated open bottom and correlated open charm are considered to fit the physical background. Three Gaussians are used to fit Υ signal and exponential functions are used to fit Drell Yan, correlated bottom and correlated charm. Errorbands of fitting function include statistical and systematical uncertainties.

Data sets	Υ Gaussians	Drell Yan	$b\bar{b}$	$c\bar{c}$
dAu South	70.4 ± 5.9	12.8 ± 5.8	22.6 ± 1.2	0.6 ± 0.3
dAu North	52.6 ± 10.6	16.7 ± 2.7	8.5 ± 1.4	0.4 ± 0.2

Table 3.12: Integrals of each components of Υ mass range in Run8dAu.

Υ mass resolution	Run6pp South raw integral	Run6pp North raw integral	Run8dAu South raw integral	Run8dAu North raw integral
600 MeV	21.7 ± 6.2	24.2 ± 6.7	70.4 ± 5.9	52.6 ± 10.6
500 MeV	21.6 ± 6.1	24.4 ± 6.6	67.0 ± 5.0	51.2 ± 10.5
700 MeV	21.6 ± 5.8	23.9 ± 6.7	73.1 ± 14.6	53.4 ± 10.7
RMS	0.4%	1%	4%	2%

Table 3.13: Systematic uncertainty table for Υ mass resolution. 600 MeV is nominal setting.

3.7 Systematic uncertainties

Since Υ signal is not as big as the J/ψ , the biggest part of the uncertainty is from the statistical uncertainty. Besides the statistical error, we estimate the systematic uncertainties as described in the following.

3.7.1 Fitting Function

We constrain or fix some parameters of the fitting function. But the shapes of Drell Yan and open bottom are not known precisely. Upsilon mass resolution is also not measured confirmly. So we need to assign the systematic uncertainties from the variations of the uncertain parameters.

Υ Gaussian width

Υ mass resolution is fixed to 600 MeV as nominal value. That is varied as 500 MeV and 700 MeV for systematic study. Table 3.13 shows the Υ yield variation for the changes. The RMS between the three yields is assigned for the systematic uncertainty of Υ mass resolution.

Drell Yan

Yield estimation from simulation is constrained by $\pm 50\%$ and slope parameter is fixed by simulation estimates for the nominal setting. $+10\%$ and -10% variation from the slope

Drell Yan slope variation	Run6pp South raw integral	Run6pp North raw integral	Run8dAu South raw integral	Run8dAu North raw integral
Estimated value	21.7 ± 6.2	24.2 ± 6.7	70.4 ± 5.9	52.6 ± 10.6
Estimated value $\times 1.1$	24.0 ± 6.2	27.5 ± 6.7	74.6 ± 5.9	58.9 ± 10.9
Estimated value $\times 0.9$	17.8 ± 6.1	18.8 ± 6.6	63.5 ± 6.0	42.3 ± 10.4
RMS	14 %	18 %	8 %	16 %

Table 3.14: Systematic uncertainty table for Drell Yan. $+10\%$ and -10% variations from the slope simulation estimate are used to estimate the systematic uncertainty for the Drell Yan estimation.

parameter are used to assign the systematic uncertainty for the Drell Yan estimation. The variation is shown in Table 3.14. The RMS between the three variations is set as the systematic uncertainty for the Drell Yan fitting function.

Open bottom

The correlated bottom estimation of pythia and the uncorrelated bottom estimation of randomizing code are tabulated in Table 3.15. The yield estimation from simulation is constrained by $\pm 100\%$ and the slope parameter is fixed by the correlated bottom estimates by pythia, for the nominal setting. The random correlated bottom slope and -10% variation from the slope parameter are considered as two extreme cases of slope variation. So those two cases are used to assign the systematic uncertainty for the open bottom estimation.

3.7.2 MUID, MUTR, BBC, Acceptance \times Efficiency.

We assign 4 % uncertainty due to MUID efficiency variation and 2 % due to MUTR efficiency variation similar to other muon arm analyses. For BBC efficiency, 10 % uncertainty is assigned for pp and 5.65 % for dAu as AN.396 calculated. We haven't studied the systematic uncertainty for acceptance \times efficiency, but the contribution from this is expected to be negligible compared to other sources since we are using only two rapidity bins, one for south arm and one for north arm. Thus we are not counting the uncertainty of acceptance \times efficiency for this analysis.

Correlated open bottom slope variation	Run6pp South raw integral	Run6pp North raw integral	Run8dAu South raw integral	Run8dAu North raw integral
Estimated value	21.7 ± 6.2	24.2 ± 6.7	70.4 ± 5.9	52.6 ± 10.6
Uncorrelated open bottom	20.8 ± 6.6	26.9 ± 7.6	66.9 ± 14.2	51.9 ± 12.4
Estimated value $\times 0.9$	19.9 ± 6.1	22.3 ± 6.7	62.0 ± 13.6	48.7 ± 10.5
RMS	7 %	7 %	9%	5%

Table 3.15: Systematic uncertainty table for open bottom correlations. The random correlated bottom slope and -10% variation from the slope parameter are used to assign the systematic uncertainty for the open bottom estimation.

3.7.3 Summary of the systematic uncertainties

Total systematic uncertainties are summarized in Table 3.16. The table includes the statistical uncertainty also.

Types of Uncertainty	Run6pp South rms	Run6pp North rms	Run8dAu South rms	Run8dAu North rms
T mass resolution	0%	1%	4%	2%
Drell Yan variation	14%	18%	8%	16%
Open bottom variation	7%	7%	9%	5%
Muid efficiency	4%	4%	4%	4%
Mutr efficiency	2%	2%	2%	2%
Systematic Total (Quadratic sum)	16%	20 %	13 %	17 %
BBC(Global)	10%	10%	5.65%	5.65%
Statistical uncertainty	29 %	28 %	8 %	20 %

Table 3.16: Total systematic and statistical uncertainty summary table.

Dataset	N_{BBC}	ϵ_{MB}^{BBC}	$\epsilon_{\Upsilon}^{BBC}$	Signal	dN/dy	$BR * d\sigma_{\Upsilon}/dy$
Run6pp South	1.721e+11	0.545	0.79	21.7 ± 6.2 ± 3.4	$7.9e-10 \pm 2.3e-10$ $\pm 1.3e-10$	33.5 ± 9.6 pb ± 5.4 pb
Run6pp North	1.793e+11	0.545	0.79	24.2 ± 6.7 ± 4.8	$8.2e-10 \pm 2.3e-10$ $\pm 1.6e-10$	34.7 ± 9.6 pb ± 6.9 pb
Run8dAu South	1.326e+11	0.88	0.936	70.4 ± 5.9 ± 9.2	$5.1e-09 \pm 4.3e-10$ $\pm 6.6e-10$	11.5 ± 1.0 nb ± 1.5 nb
Run8dAu North	1.365e+11	0.88	0.936	52.6 ± 10.6 ± 8.9	$3.8e-09 \pm 7.7e-10$ $\pm 6.5e-10$	8.6 ± 1.7 nb ± 1.5 nb

Table 3.17: Υ invariant yield and $BR \times$ cross section of Run6pp and Run8dAu dataset.

3.8 Results

3.8.1 Invariant yield and cross section

We calculate invariant yield and cross section using the equation below

$$B \frac{dN_{\Upsilon}}{dy} = \frac{1}{\Delta y} \frac{N_{\Upsilon}}{A \epsilon_{\Upsilon} \epsilon_{\Upsilon}^{BBC}} / \frac{N_{MB}^{BBC}}{\epsilon_{MB}^{BBC}}, \quad (3.5)$$

$$B \frac{d\sigma_{\Upsilon}}{dy} = B \frac{dN_{dy}}{dy} \sigma_{Total} \quad (3.6)$$

Table 3.17 includes the invariant yield and $BR \times$ cross section of Run6pp and Run8dAu dataset. To get the σ_{Υ} , the branching ratio of $\Upsilon \rightarrow \mu^+ \mu^-$ is obtained from the PDG on the webpage at

<http://pdg.lbl.gov/>

The branching ratio is summarized in Table 3.18. The effective branching ratio weighted over the three states is calculated as 2.37%. σ_{Υ}/dy with this effective branching ratio is

Υ states	Mass	BR of $\Upsilon \rightarrow \mu^+ \mu^-$	fraction of total Υ from CDF
Υ_{1S}	9.46	2.48	73 %
Υ_{2S}	10.02	1.93	17 %
Υ_{3S}	10.36	2.29	10 %

Table 3.18: $\Upsilon \rightarrow \mu^+ \mu^-$ branching ratios. Values are obtained from PDG

Data set	rapidity	σ_Υ/dy
Run6pp South	[-2.2,-1.2]	$1.41 \pm 0.40(\text{stat.}) \pm 0.23(\text{syst.}) \text{ nb}$
Run6pp North	[1.2,2.2]	$1.46 \pm 0.41(\text{stat.}) \pm 0.29(\text{syst.}) \text{ nb}$
Run8dAu South	[-2.2,-1.2]	$485 \pm 42(\text{stat.}) \pm 63(\text{syst.}) \text{ nb}$
Run8dAu North	[1.2,2.2]	$364 \pm 72(\text{stat.}) \pm 62(\text{syst.}) \text{ nb}$
Run5pp South	[-2.2,-1.2]	$1.90 \pm 0.51(\text{stat.}) \text{ nb} \text{ (for comparison)}$
Run5pp North	[1.2,2.2]	$2.40 \pm 0.81(\text{stat.}) \text{ nb} \text{ (for comparison)}$

Table 3.19: Υ cross sections considering the effective branching ratio of 2.37%. The Run5pp preliminary result is also shown for the comparison.

calculated in Table 3.19 and also includes the Run5pp preliminary result for comparison. Figure 3.16 compares between the Run5pp preliminary result and Run6pp result for σ_Υ as a function of rapidity. Run6pp results for the Υ cross section without consideration of the statistical uncertainty are about 30% or 40% smaller than the Run5pp preliminary result, and this difference is thought to be due to the contribution of Drell Yan and open bottom correlation. If we do not consider that contribution, Run6pp results are consistent with the Run5pp results when we don't count the statistical uncertainty. Moreover, the Run6pp results are quite symmetric between the north and south. These convince us that the Run6pp results are quite believable. Figure 3.17 shows σ_Υ as a function of rapidity. The value of $y \in [-0.35, 0.35]$ is obtained from Run6pp central arm preliminary result, AN 802 based on $\Upsilon \rightarrow e^+ e^-$ decay channel. Figure 3.17 also has the theoretical comparison from Ramona Vogt. When we compare the rapidity

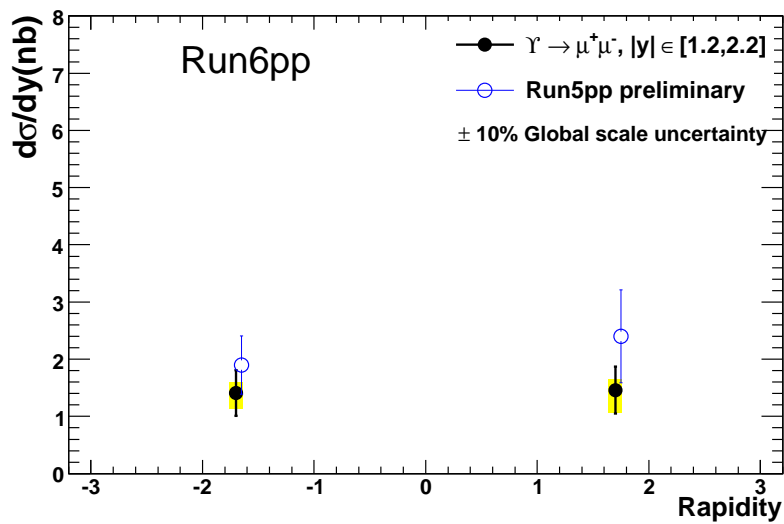


Figure 3.16: γ cross section vs. rapidity of Run5pp preliminary result and Run6pp result. For Run6pp γ cross section measurement, residual background of Drell Yan, correlated bottom and correlated charm is considered. This seems to make the new measurement of Run6pp σ_γ to be a bit smaller than the Run5pp preliminary result though they are consistent within the statistical uncertainty.

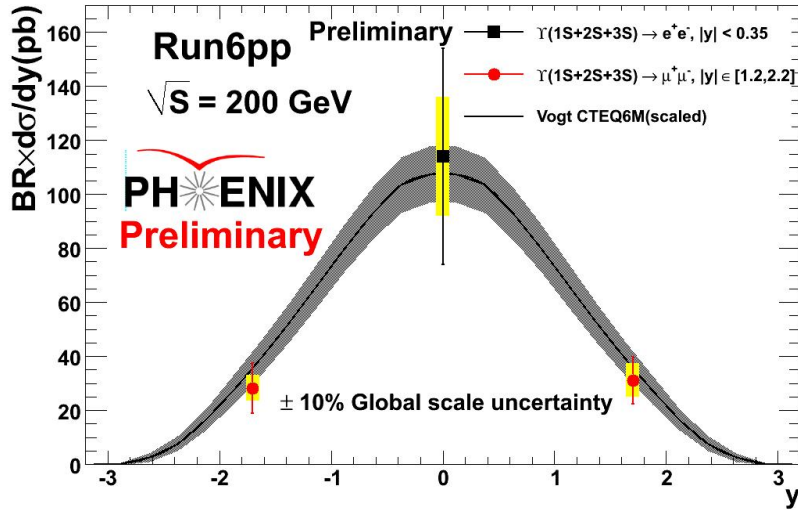


Figure 3.17: Υ cross section vs. rapidity of Run6pp. Comparison to Ramona’s theoretical estimation is also shown where her estimation is scaled down by factor of 2.

distribution with Ramona’s CEM model it matches well with her estimation scaling down her calculation by factor of 2.

3.8.2 Nuclear modification factor

The nuclear modification factor, R_{dAu}^{Υ} is taken from the equation of

$$R_{dAu}^{\Upsilon} = \frac{dN_{dAu}^{\Upsilon}/dy}{\langle N_{coll} \rangle dN_{pp}^{\Upsilon}/dy} \quad (3.7)$$

We can get R_{dAu}^{Υ} with Run6pp and Run8dAu invariant yields using the formula below. The value, $\langle N_{coll} \rangle$ is extracted from AN 342 and 7.58 is used for all centrality.

$$R_{dAu}^{\Upsilon} |_{y \in [-2.2, -1.2]} = 0.85 \pm 0.25(stat.) \pm 0.17(syst.) \quad (3.8)$$

$$R_{dAu}^{\Upsilon} |_{y \in [1.2, 2.2]} = 0.61 \pm 0.21(stat.) \pm 0.16(syst.) \quad (3.9)$$

Figure 3.18 shows R_{dAu}^{Υ} for two rapidity bins, one for the south arm (Au going direction) and one for North arm (deuterium going direction). This result shows a quite interesting result that there is suppression at low x shadowing region. We are waiting for the theoretical comparison.

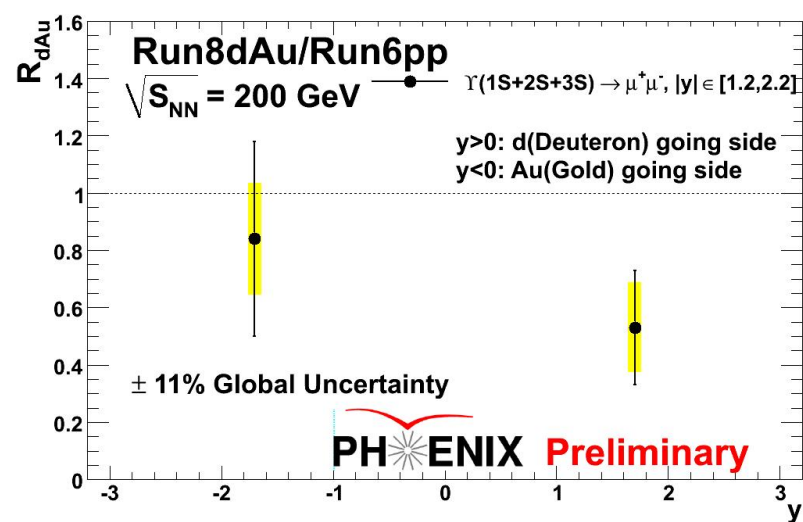


Figure 3.18: R_{dAu}^γ with Run8dAu/Run6pp.

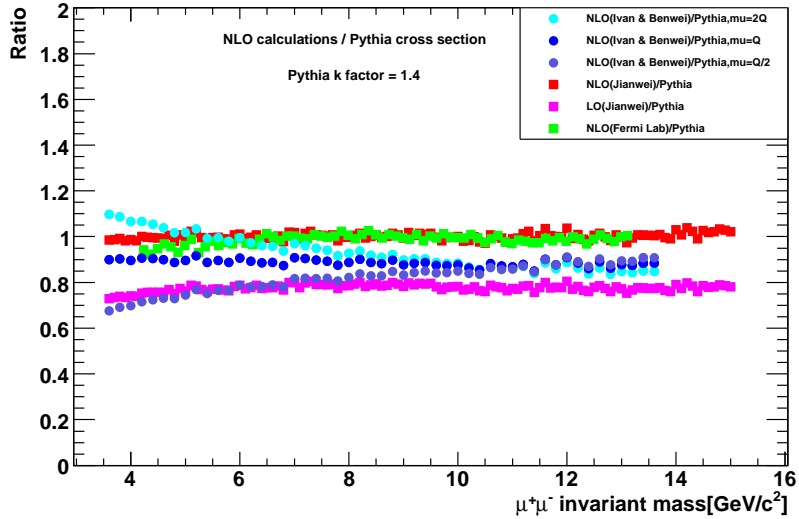


Figure 3.19: Comparison of pythia estimation and NLO Drell Yan calculation

3.9 Updates with NLO Drell Yan calculation

3.9.1 NLO Drell Yan calculation

NLO Drell Yan calculation is taken from Ivan Vitev, Jianwei and Fermi Lab. Figure 3.19 shows the comparison of pythia and NLO Drell Yan calculations. Among these calculations, Ivan's one is put to replace the preliminary Drell Yan estimation which has been done by pythia estimation. With the NLO calculation, more precise Υ analysis has been accomplished since the uncertainty from pythia estimation lessens.

3.9.2 Updated result

NLO estimations are fixed and put for the real data Υ fitting. The level of NLO estimation is higher than one from the pythia as seen in Figure 3.20. So the σ_Υ lessens than the preliminary result. Table 3.20 is comparing the updated cross sections, R_{dAu}^Υ and the preliminary results. Figure 3.21 shows updated R_{dAu}^Υ . The values are increased by about ~ 0.1 . But the difference of preliminary and updated results are in statistical uncertainty.

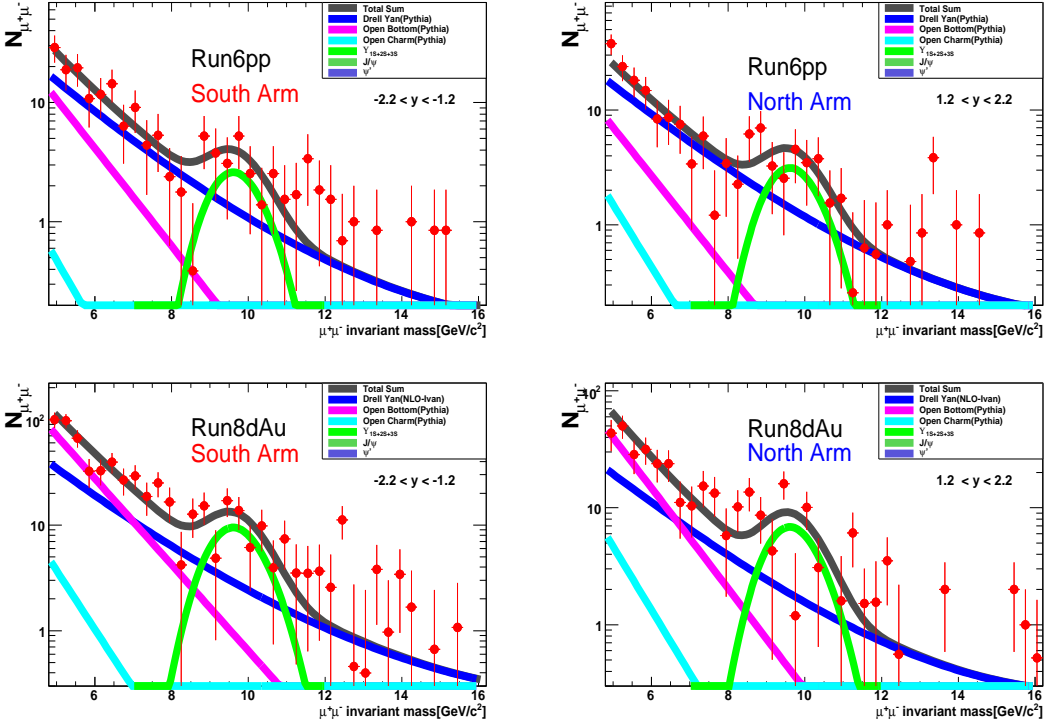


Figure 3.20: Υ fitting of North arm and South arm. NLO Drell Yan, correlated open bottom and correlated open charm are considered to fit the physical background. Three Gaussians are used to fit Υ signal and exponential functions are used to fit Drell Yan, correlated bottom and correlated charm. Errorbands of fitting function include statistical and systematical uncertainties.

Fitting results	σ_{Υ} of $p + p$ collision (North)	σ_{Υ} of $p + p$ collision (South)	R_{dAu}^{Υ} (North)	R_{dAu}^{Υ} (South)
Preliminary result	31.1 ± 8.7 pb	28.2 ± 9.4 pb	0.53 ± 0.20	0.84 ± 0.34
Updated result	25.2 ± 8.7 pb	22.5 ± 8.9 pb	0.62 ± 0.26	0.95 ± 0.44

Table 3.20: Υ cross section and R_{dAu} of preliminary and NLO Drell Yan updated result

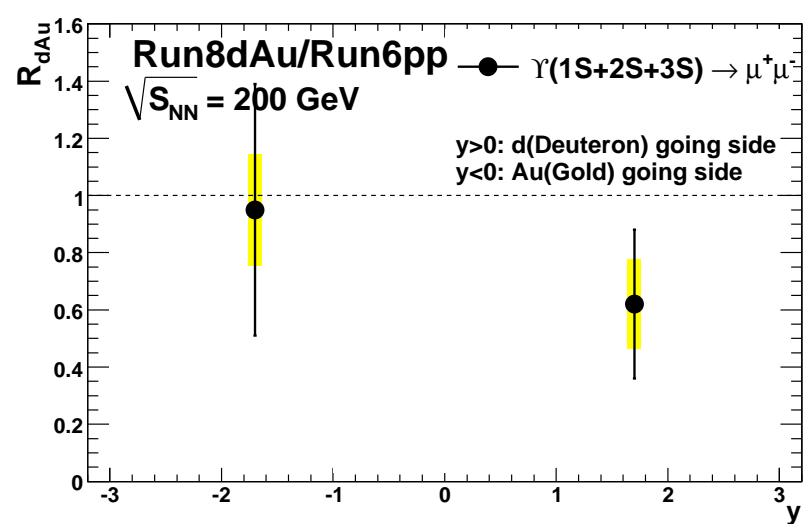


Figure 3.21: R_{dAu}^γ with Run8dAu/Run6pp.

Chapter 4

Data Analysis 2 - χ_c measurement at $p + p$ and $d + \text{Au}$ Collisions

4.1 Data set, Quality Assurance Good Run list

4.1.1 Quality Assurance, Good Runlist and Data Set

Run8dAu and Run8pp data are analyzed. For the Muon Arm, Quality Assurance was performed like Υ analysis. Additionally, for the MPC, bad runs are extracted along the MPC correlation analysis, AN 886. After excluding bad run numbers, 238 runs are available for Run8pp and 695 runs are available for Run8dAu when riding on analysis train. See the Appendix for the detailed run numbers. Table 4.1 shows the number of minimum bias events from BBC live counts and integrated luminosity. Integrated luminosity is calculated using the formulae below.

$$Luminosity = \frac{N_{MB}^{BBC}}{\sigma_{BBC}} \quad (4.1)$$

$$\sigma_{BBC} = \sigma_{Total} \times \varepsilon_{BBC} \quad (4.2)$$

where, for dAu collision system, $\sigma_{Total}^{dAu} = 2.26 \text{ b}$ is the total cross section which was taken from Sebastian White's dAu dissociation cross section measurement for MB normalization of AN 385. $\varepsilon_{BBC}^{dAu} = 0.88$ is the BBC Min. Bias efficiency of which value is taken from AN 396. Similarly, $\sigma_{Total}^{pp} = 42.2 \text{ mb}$ and $\varepsilon_{BBC}^{pp} = 0.545$ is used for pp collision system.

Dataset	Runs analyzed	N_{MB}^{BBC}	Luminosity
Run8pp South	238	9.715e+10	4.24pb ⁻¹
Run8pp North	238	9.715e+10	4.24pb ⁻¹
Run8dAu North	695	1.337e+11	69.7nb ⁻¹

Table 4.1: BBC MB Event and Luminosity of Run8pp and Run8dAu

Cut Name	Run8pp	Run8dAu
BBC z-vertex range	$ Z_{vtx} < 30cm$	$ Z_{vtx} < 30cm$
DG0 North/South	20/16	20/16
DDG0 North/South	9/9	9/9
MUTR χ^2	23.0	23.0
Vertex match χ^2	9.0	9.0
Rapidity	$1.2 < y < 2.2$	$1.2 < y < 2.2$
MUID LL1	2D trigger	2D trigger

Table 4.2: Cut conditions for Muon arm of Run8pp and Run8dAu. Cut conditions for Muon Arm are basically the same as the J/ψ analysis from AN 794

4.1.2 Cut conditions

Basic dimuon cuts, which are common to Run8pp and Run8dAu J/ψ analysis of AN 794, are applied as seen in Table 4.2. MPC cuts are tabulated in Table 4.3. Those are determined by simulation and MPC performance. Simulation study for MPC kinematic cuts are explained in section 4.3.3.

4.1.3 MPC ϕ angle distribution

Fig. 4.2 shows ϕ distribution of the embedding simulation for the North arm. There comes up weird peak around [-2.7, -3.1] of ϕ angle. Fig. 4.1 shows ϕ distribution of the single simulation for the North arm. This means that the peak is not from χ_c signal So we masked out that area for the North MPC. On the right plot of Fig. 4.2, that area

Cut Name	Run8pp	Run8dAu
Photon energy	$1.3 < E < 5.0$	$1.3 < E < 5.0$
MPC radius	$11 < r < 19$	$11 < r < 19$
Dispersion	$d < 4$	$d < 4$
Cluster χ^2	Cluster $\chi^2 < 2.5$	Cluster $\chi^2 < 2.5$
MPC warnmap	Applied	Applied
Kinematic cuts	$1.2 < y < 2.2$	$1.2 < y < 2.2$
Tanztential angle cut	Not applied	Appiled
Photon energy-rapidity cut	Not applied	Appiled

Table 4.3: Cut conditions for MPC of Run8pp and Run8dAu. MPC warnmap was taken from Beau's MPC analysis

corresponds to the red towers.

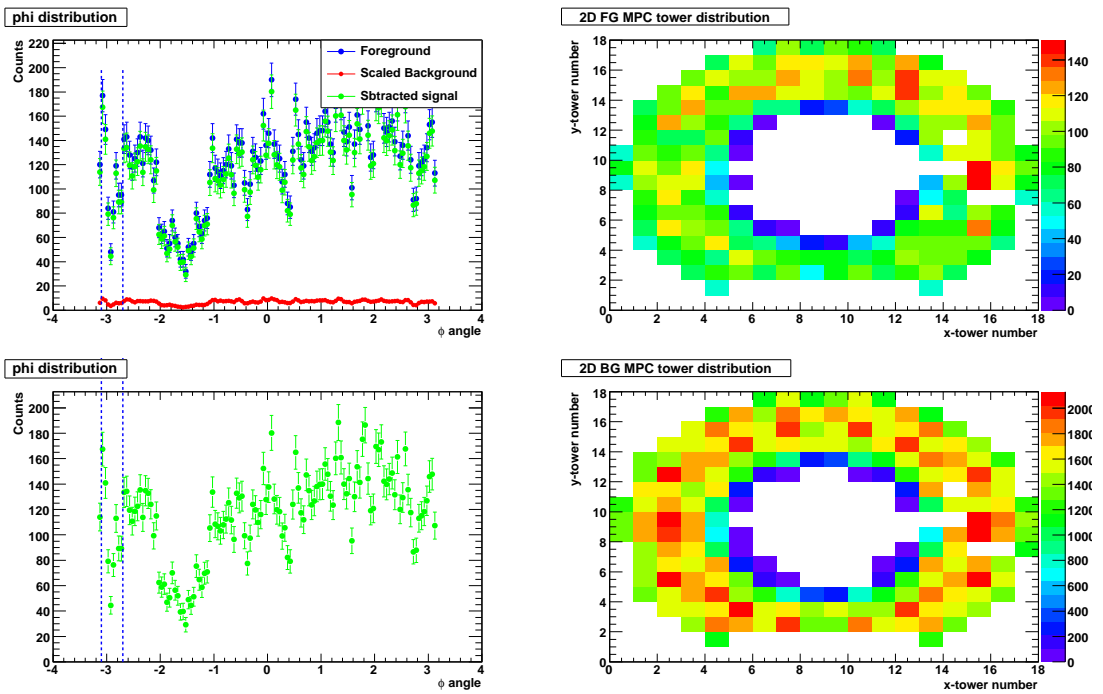


Figure 4.1: Left plot: The ϕ distribution of the single χ_c simulation. Right plot: MPC tower hit distribution.

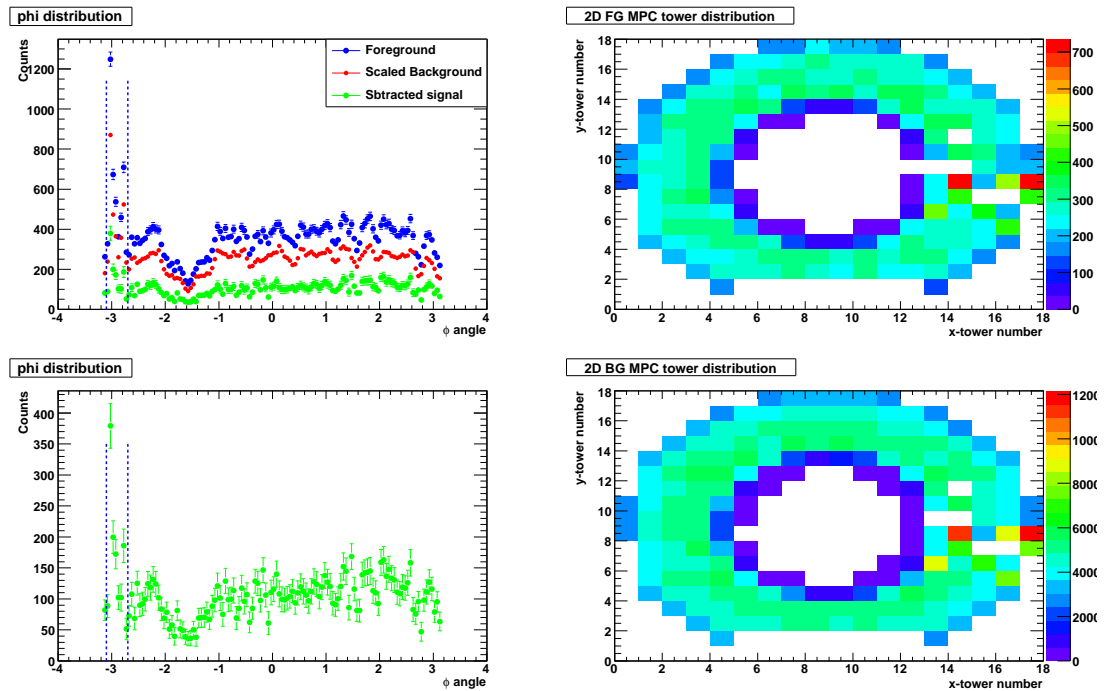


Figure 4.2: Left plot: The ϕ distribution of the embedded χ_c simulation. Right plot: MPC tower hit distribution. The peak around $[-2.7, -3.1]$ of ϕ is thought to come from background. So that area is masked out.

4.2 Data Analysis

4.2.1 Analysis code and output

χ_c is reconstructed by three particle correlation of χ_c decay dimuon and χ_c decay photon. So the code to correlate three particle is developed at CVS

offline/AnalysisTrain/Chic_analyzer

Analysis train 219 was used to get the analysis output which contains the three particle correlations. The macros for train riding are in CVS:

offline/AnalysisTrain/pat/macro/Run_run8_chic_mpc_muon_pp_10.C
offline/AnalysisTrain/pat/macro/Run_run8_chic_mpc_muon_10.C

The χ_c signal is reconstructed as mass difference between χ_c and *dimuon* of,

$$\mu^+ \mu^- \gamma - \mu^+ \mu^-, \quad (4.3)$$

Here, $\mu^+ \mu^- \gamma$ is three particle correlation of dimuon and photon. And $\mu^+ \mu^-$ is two particle correlation of dimuon. For the Foreground events, three particles are reconstructed from same event. And for the combinatorial background, muon pair of one event and MPC photon of another events was reconstructed. Fig. 4.3, 4.4 and 4.5 show the χ_c reconstruction from real data.

Study of Normalization range

After applying the cuts, it is hard to determine the right normalization since remaining events out of the χ_c signal region is not sufficient. That makes any small change of mass region to be a big change of the normalization scale factor. So the like sign of dimuon pair was used to determine the normalization scale factor. χ_c signal is reconstructed from the correlation of the unlike sign dimuon, which is from J/ψ , and photon. But the correlation of the like sign and photon is just fake signal since like sign is not from J/ψ . Here the probability for the like sign to be correlated with photon from the another event could be assumed to be same with the probability for the unlike sign to be correlated with photon from the another event since those correlations are just random. Fig. 4.3, 4.4 and 4.5 show the χ_c signal applying the normalization scale factor which is taken from the like sign. Normalization scale factor is calculated as

$$F = \frac{FG_{++} + FG_{--}}{BG_{++} + BG_{--}}, \quad (4.4)$$

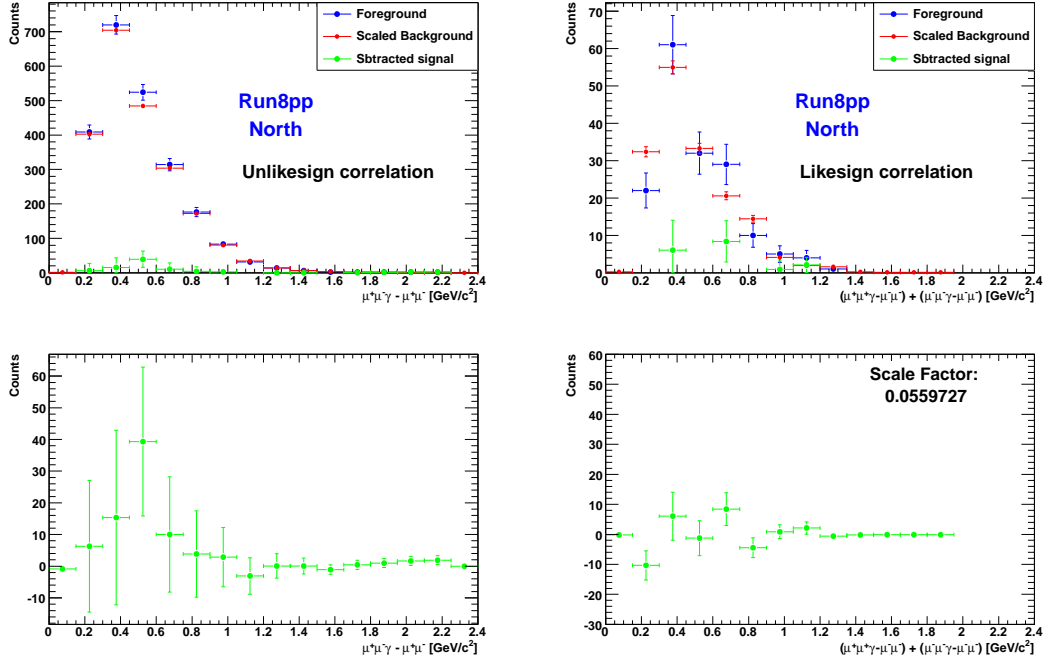


Figure 4.3: Mass difference between χ_c and J/ψ . Left plot is three particle correlation of unlikesign dimuon which is the signal and right plot is three particle correlation of likesign which is to get scale factor. These plots are from Run8pp North arm.

Here, F is the scale factor, FG_{++} represents like sign muon pair correlation of $\mu^+ \mu^+ \gamma - \mu^- \mu^- \gamma$ in same event, FG_{--} represents like sign muon pair correlation of minus sign and BG takes the γ from another events. Right plots of Fig. 4.3, 4.4 and 4.5 show the likesign events for data sets.

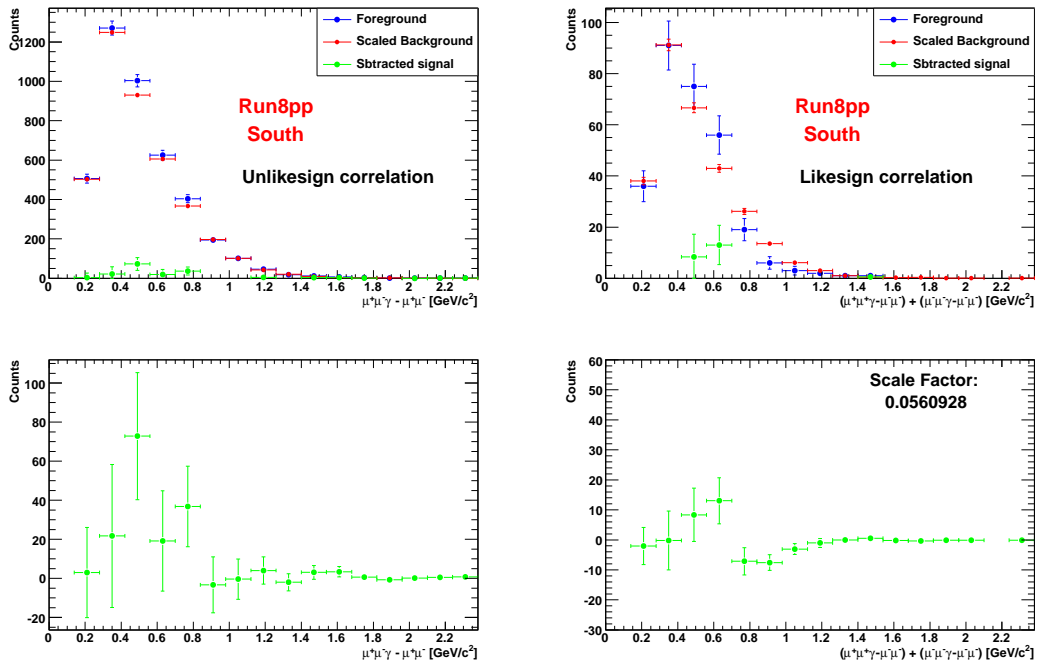


Figure 4.4: Mass difference between χ_c and J/ψ . Left plot is three particle correlation of unlikesign dimuon which is the signal and right plot is three particle correlation of likesign which is to get scale factor. These plots are from Run8pp South arm.

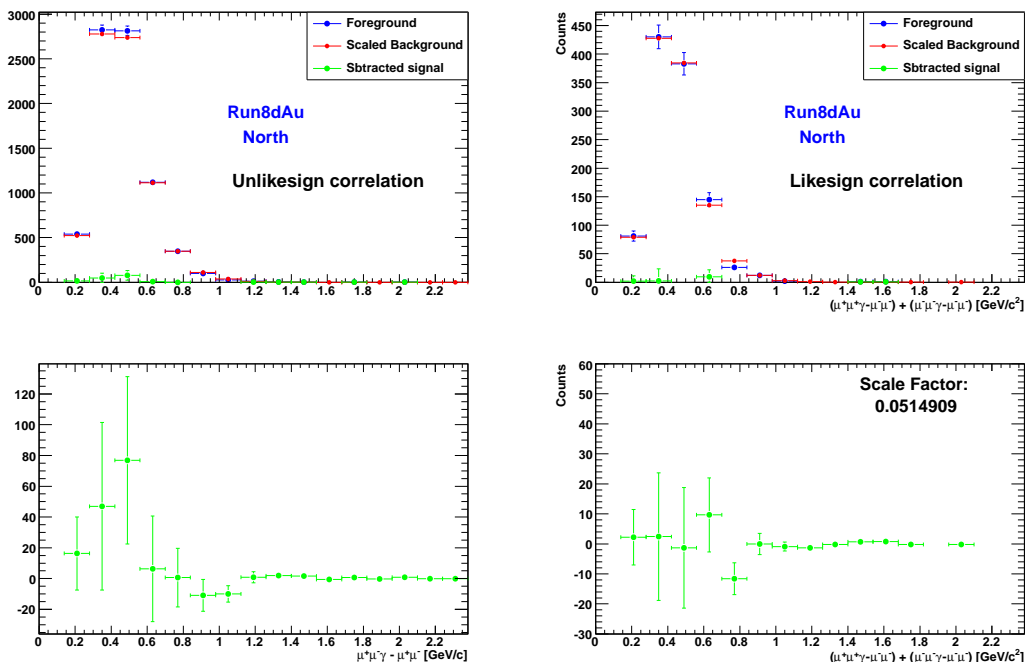


Figure 4.5: Mass difference between χ_c and J/ψ . Left plot is three particle correlation of unlikesign dimuon which is the signal and right plot is three particle correlation of likesign which is to get scale factor. These plots are from Run8dau North arm.

4.3 χ_c simulation

χ_c simulation is important to test the feasibility of the χ_c , determine the kinematic cuts and calculate the acceptance×efficiency, which is most important and one of hardest part of χ_c analysis since MPC has small geometrical acceptance and large background of which energy is around the χ_c photon energy. We tried embedding simulation to estimate the background level.

4.3.1 Single χ_c simulation

Single χ_c simulation is used to test the χ_c reconstruction code and to get the resolution of χ_c . PHPythia event generator was used to generate three kinds of χ_c state. But the contribution of χ_{c0} state is estimated to be negligible since it has small branching ratio to J/ψ decay. The rest two states of χ_c is run through the PISA and Fun4all simulation chain to check the detector effects and check the kinematics of the χ_c . Pythia generation card for χ_{c1} and χ_{c2} is seen at Table 4.4. And the cards are accessible at CVS :

```
event_gen/src/PHPythia/macros/chictojpsi.cfg
```

And the detailed description for the pythia setting can be obtain in the official pythia manual

<http://home.thep.lu.se/~torbjorn/pythia/lutp0613man2.pdf>

The reconstruction is done using same code with real data.

MPC Geometrical acceptance of χ_c

Fig. 4.6 shows rapidity distribution of J/ψ which decays from χ_{c1} using pythia generator. Here, MPC decay photon has rapidity distribution like Fig. 4.7 when J/ψ comes into Muon arm rapidity of $1.2 < |y| < 2.2$. MPC has very forward rapidity coverage of $3.1 < |y| < 3.8$. For the χ_{c1} , the MPC photon has geometrical acceptance of 3.5 % which is small value. Fig. 4.8 and Fig. 4.9 are same rapidity distribution of J/ψ and MPC photon for the χ_{c2} . For the χ_{c2} , the MPC photon geometrical acceptance is 3.8 %

Energy distribution of χ_c decay photon

Fig. 4.10 shows the energy distribution of χ_{c1} decay photon of MPC when χ_{c1} decay J/ψ goes into Muon Arm. Since the MPC is located at very forward region, the χ_{c1} decay photon to MPC is simulated to have energy bigger than about 1 GeV. Fig. 4.11 is same

Parameters	Index1	Index2	Setting	Meaning
msel			0	turn off all production mechanisms manually
msub	86		0	turn off $g + g \rightarrow J/\psi + g$
msub	87		1	turn on $g + g \rightarrow \chi_{c0} + g$
msub	88		1	turn on $g + g \rightarrow \chi_{c1} + g$
msub	89		1	turn on $g + g \rightarrow \chi_{c2} + g$
mdme	1501	1	1	turn off $\chi_{c0} \rightarrow J/\psi\gamma$
mdme	1502	1	0	turn on $\chi_{c0} \rightarrow random$
mdme	1555	1	1	turn off $\chi_{c1} \rightarrow J/\psi\gamma$
mdme	1556	1	0	turn off $\chi_{c1} \rightarrow random$
mdme	861	1	1	turn off $\chi_{c2} \rightarrow J/\psi\gamma$
mdme	862	1	0	turn off $\chi_{c2} \rightarrow random$
mdme	858	1	0	turn off $J/\psi \rightarrow e^+e^-$
mdme	859	1	1	turn on $J/\psi \rightarrow \mu^+\mu^-$
mdme	860	1	0	turn off $J/\psi \rightarrow random flavor$
mstp	51		7	select PDF of CTEQ5L

Table 4.4: Simulation parameters for χ_c generation.

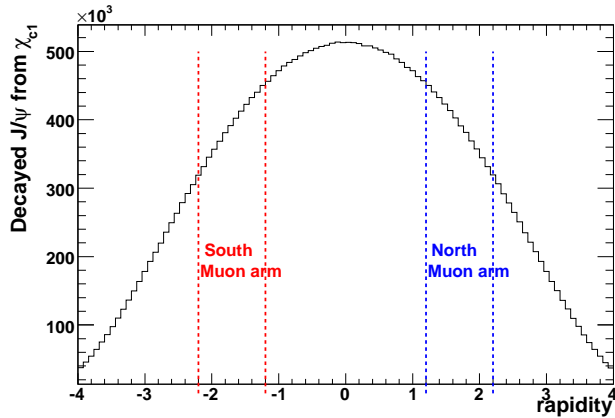


Figure 4.6: The decay J/ψ of generated χ_{c1} by PHPythia generator. The dotted line represents the geometrical Muon arm acceptance. Reds for South, Blues for North.

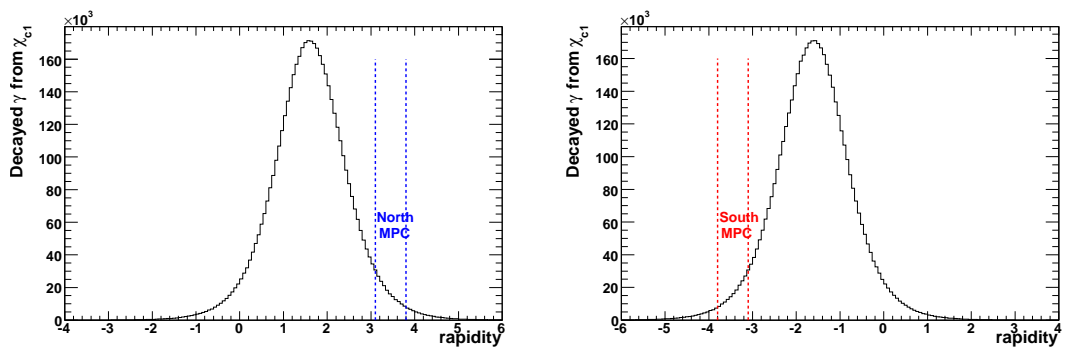


Figure 4.7: The decay γ of generated χ_{c1} by PHPythia generator. The dotted line represents the geometrical MPC acceptance. Left figure is from north muon arm and blue lines represent for North MPC. Right figure is from south muon arm and red lines represent for South MPC.

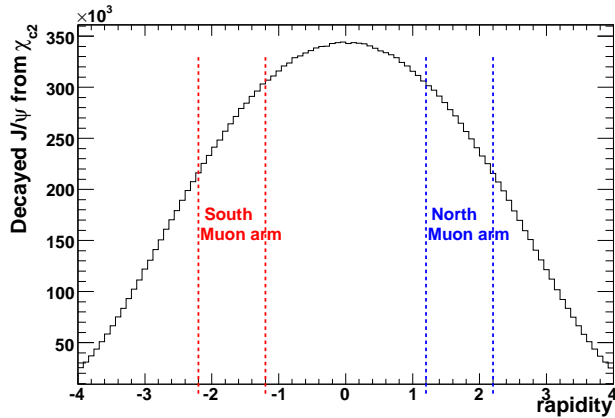


Figure 4.8: The decay J/ψ of generated χ_{c2} by PHPythia generator. The dotted line represents the geometrical Muon arm acceptance. Reds for South, Blues for North.

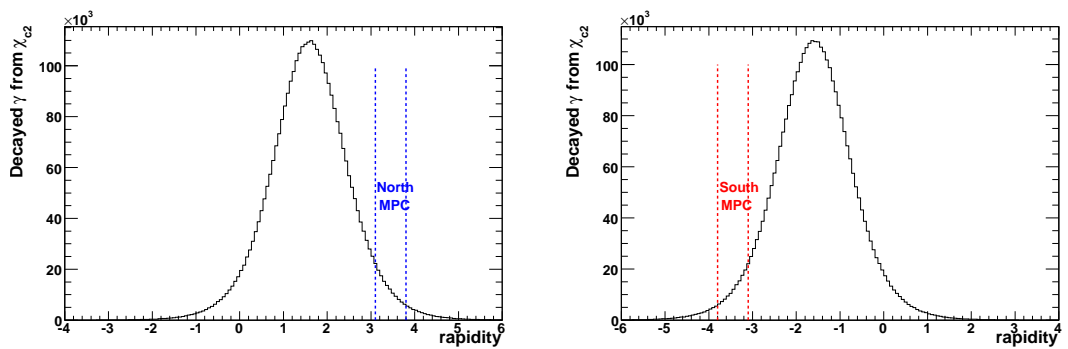


Figure 4.9: The decay γ of generated χ_{c2} by PHPythia generator. The dotted line represents the geometrical MPC acceptance. Left figure is from north muon arm and blue lines represent for North MPC. Right figure is from south muon arm and red lines represent for South MPC.

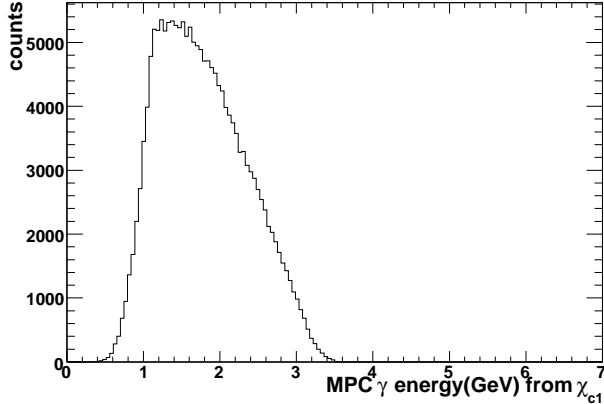


Figure 4.10: The energy distribution of χ_{c1} decay γ at MPC. The γ is tagged when decay J/ψ goes into Muon arm.

plot but just for χ_{c2} . This makes the MPC photon energy cut for the photon less than around 1 and MPC photon energy cut is expected to get rid of low energy background.

χ_c reconstruction and mass resolution

Fig. 4.12 and 4.14 show mass difference between the reconstructed χ_{c1} and the reconstructed dimuon pair. As you see the figure, it gives resonable peak position comparing to the PDG values. And it gives about 100 MeV mass resolution for the χ_{c1} and about 110 MeV for the χ_{c2} . Fig. 4.13 and 4.15 are for χ_{c2} .

4.3.2 Embedded χ_c simulation

Embedding simulation is mainly for estimating the background contribution from high multiplicity of MPC. In real data, signal to background ratio is estimated about 1/10 and almost of the background come from the MPC. So it is important to estimate the background level and signal loss from the background correctly. To embed the χ_c to real data, Muon arm and MPC embeddings are added at same level. For MPC embedding, mpc tower energy of χ_c photon and background from real data were summed.

χ_c reconstruction and mass resolution

Fig. 4.16 and 4.18 are the mass differences between the reconstructed χ_{c1} - the reconstructed dimuon pair by embedding simulation. And Fig. 4.17 and 4.19 are for χ_{c2} .

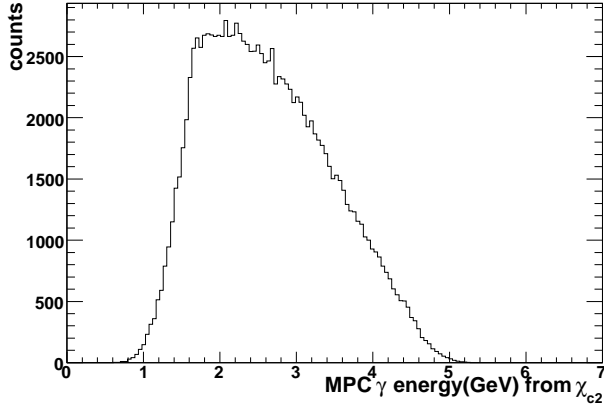


Figure 4.11: The energy distribution of χ_{c2} decay γ at MPC. The γ is tagged when decay J/ψ goes into Muon arm.

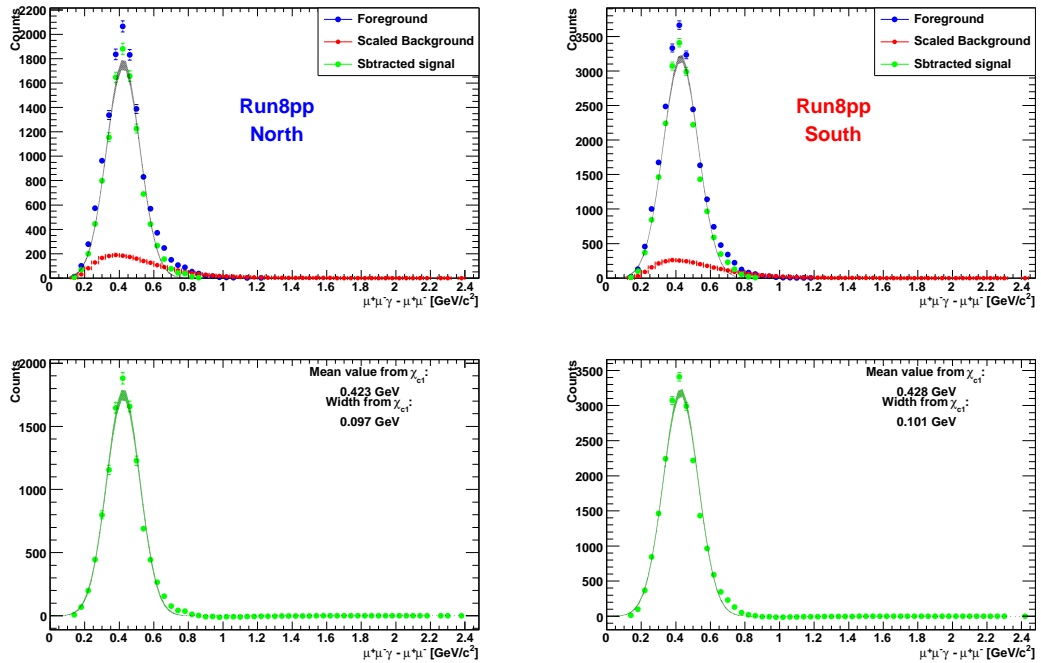


Figure 4.12: The reconstructed mass difference between χ_{c1} and J/ψ by single simulation. Based on PDG value, the difference is $3.510(\chi_{c1}) - 3.096(J/\psi) = 0.414$ GeV. The plots are for Run8pp North and South arms

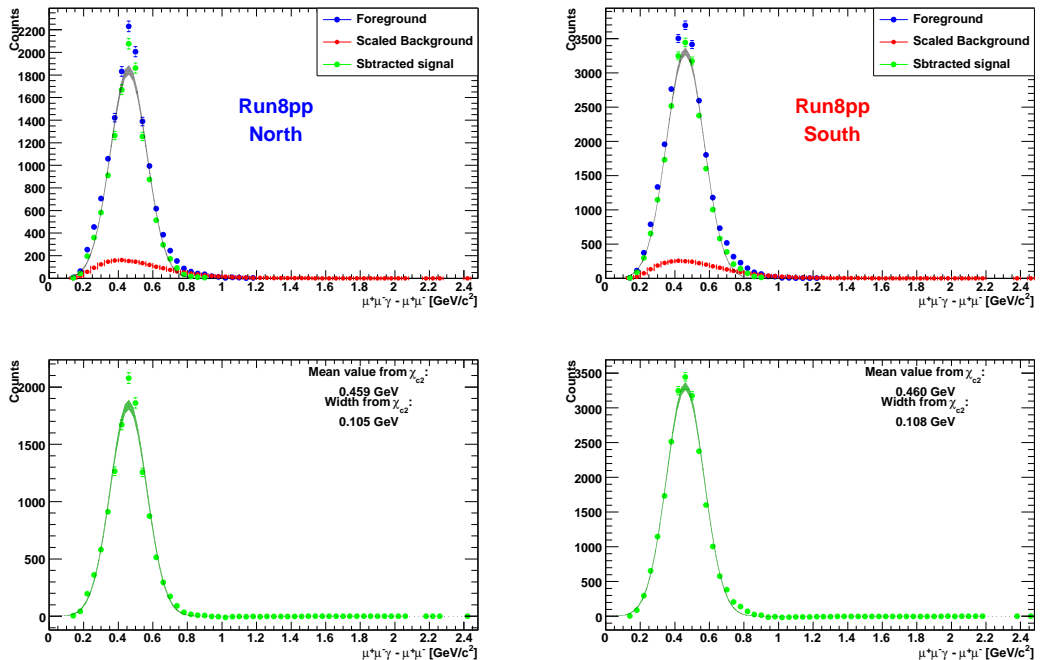


Figure 4.13: The reconstructed mass difference between χ_{c2} and J/ψ by single simulation. Based on PDG value, the difference is $3.556(\chi_{c2}) - 3.096(J/\psi) = 0.46$ GeV. The plots are for Run8pp North and South arms

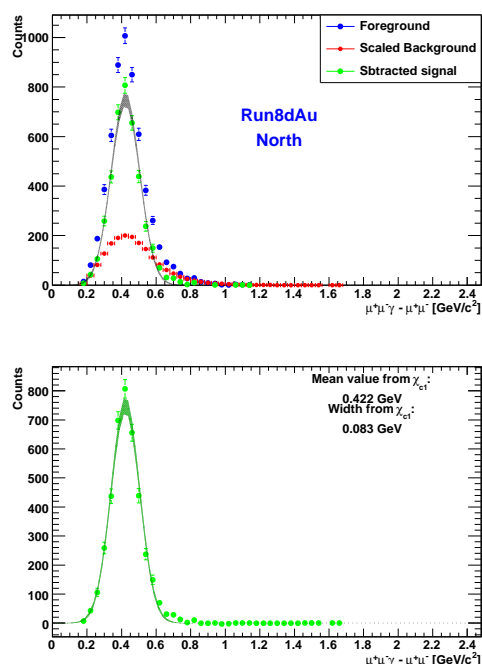


Figure 4.14: The reconstructed mass difference between χ_{c1} and J/ψ by single simulation. Based on PDG value, the difference is $3.510(\chi_{c1}) - 3.096(J/\psi) = 0.414$ GeV. The plots are for Run8dau North arm

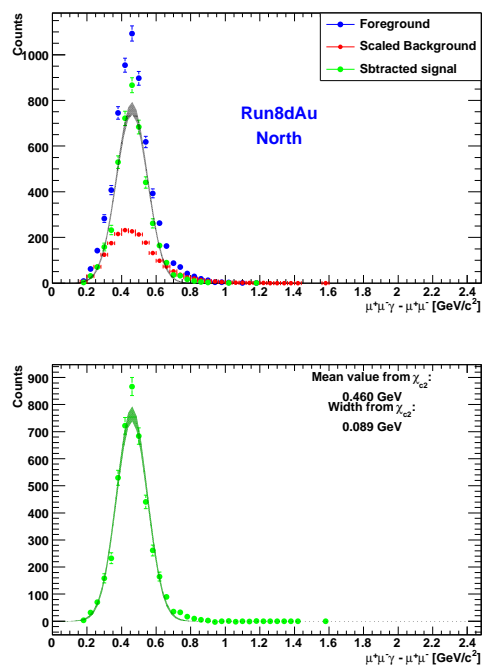


Figure 4.15: The reconstructed mass difference between χ_{c2} and J/ψ by single simulation. Based on PDG value, the difference is $3.556(\chi_{c2}) - 3.096(J/\psi) = 0.46$ GeV. The plots are for Run8dau North arm

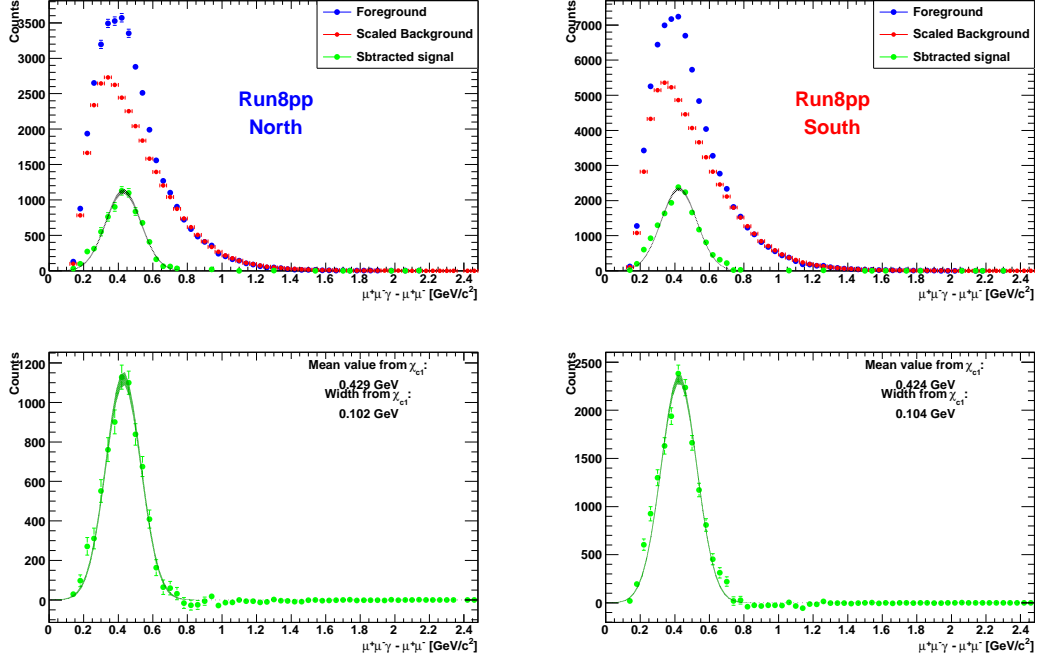


Figure 4.16: The reconstructed mass difference between χ_{c1} and J/ψ by embedding simulation. Based on PDG value, the difference is $3.510(\chi_{c1}) - 3.096(J/\psi) = 0.414$ GeV. The plots are for Run8pp North and South arms

To normalize the background, two mass regions of 0.0 - 0.2 GeV and 0.8 - 2.5 GeV are used which is turned out to contain no χ_c signal from single χ_c simulation. The mass resolutions from embedding simulation become little poorer than single simulation. We use the mass resolutions and peak values from embedding simulation since embedding simulation is thought to be more close to realistic than single simulation since it has big MPC background as real data.

Acceptance \times Efficiency calculation

We calculate χ_c acceptance \times efficiency value by dividing the reconstructed χ_c by the thrown χ_c within Muon arm and MPC acceptance. Table 4.5 includes the values for the Run8pp North arm, Run8pp South arm and Run8dAu North arm for the χ_{c1} . Table 4.6 is about χ_{c2} . When we reconstruct, same cuts and macros with real data reconstruction are used except for a few minor things like the Level-1 trigger. That is, simulated data use the emulated Level-1 2 Deep trigger while real data use the real Level-1 2 Deep trigger. The reference run numbers are 259042 for Run8pp and 249085 for Run8dAu. After we

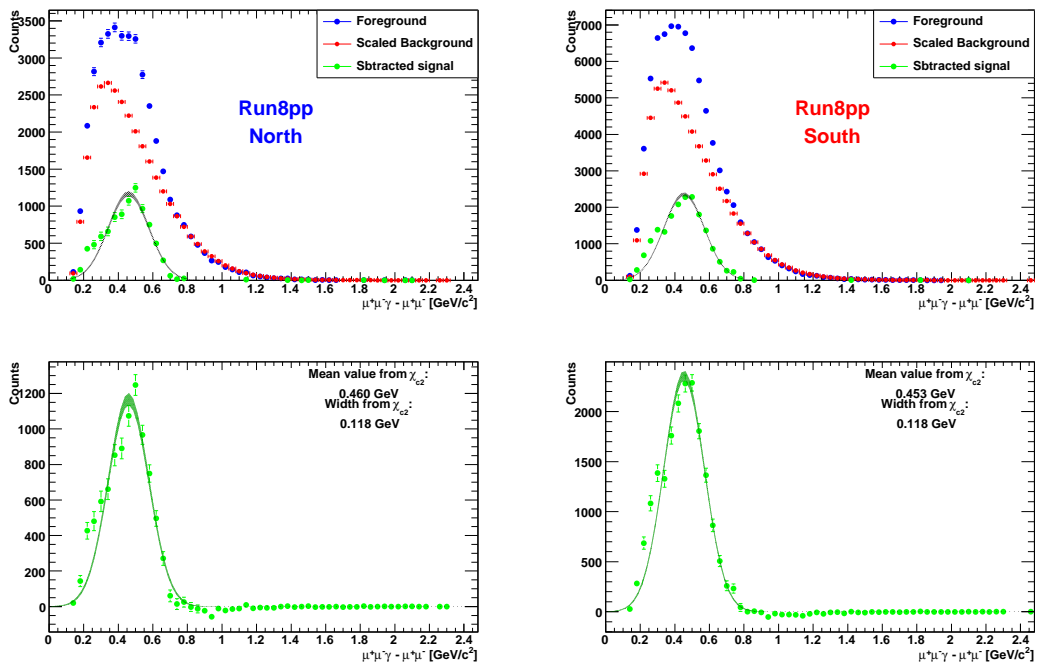


Figure 4.17: The reconstructed mass difference between χ_{c2} and J/ψ by embedding simulation. Based on PDG value, the difference is $3.556(\chi_{c2}) - 3.096(J/\psi) = 0.46$ GeV. The plots are for Run8pp North and South arms

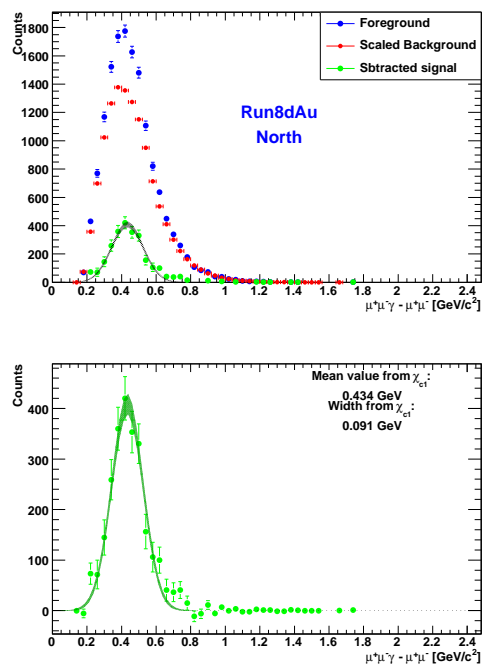


Figure 4.18: The reconstructed mass difference between χ_{c1} and J/ψ by embedding simulation. Based on PDG value, the difference is $3.510(\chi_{c1}) - 3.096(J/\psi) = 0.414 \text{ GeV}$. The plots are for Run8dau North arm

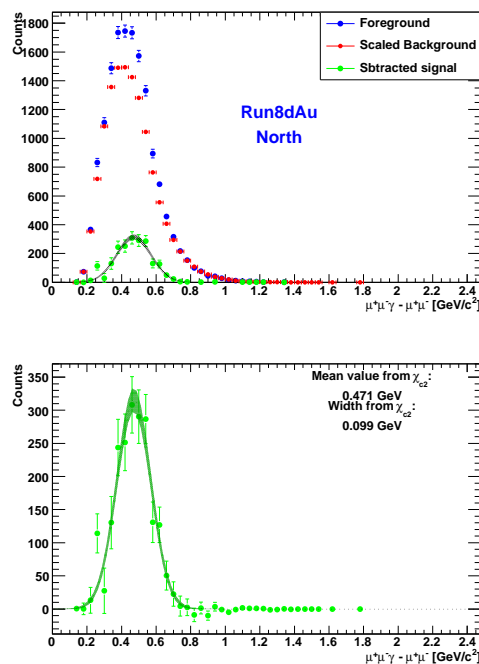


Figure 4.19: The reconstructed mass difference between χ_{c2} and J/ψ by embedding simulation. Based on PDG value, the difference is $3.556(\chi_{c2}) - 3.096(J/\psi) = 0.46$ GeV. The plots are for Run8dau North arm

Dataset	Thrown χ_{c1}	Reconstructed χ_{c1} (Single simulation)	Reconstructed χ_{c1} (Embedding simulation)	Acceptance \times Efficiency (%)
Run8pp North	779238	11952.3	8852.51	1.14
Run8pp South	780230	22034.9	17736.2	2.27
Run8dAu North	640892	4352.26	1983.95	0.31

Table 4.5: Acceptance \times Efficiency values of χ_{c1} . Rapidity ranges are $1.2 < |y| < 2.2$ for the muon arm and $3.1 < |y| < 3.8$ for the MPC.

Dataset	Thrown χ_{c1}	Reconstructed χ_{c1} (Single simulation)	Reconstructed χ_{c1} (Embedding simulation)	Acceptance \times Efficiency (%)
Run8pp North	801894	12918.4	11168.3	1.39
Run8pp South	802898	23895.2	21763.1	2.71
Run8dAu North	651290	4535.68	2036.79	0.31

Table 4.6: Acceptance \times Efficiency values of χ_{c2} . Rapidity ranges are $1.2 < |y| < 2.2$ for the muon arm and $3.1 < |y| < 3.8$ for the MPC.

get the acceptance \times efficiency values for χ_{c1} and χ_{c2} , we average both values for the inclusive χ_c . Only one bin of $1.2 < |y| < 2.2$ (Muon arm) and $3.1 < |y| < 3.8$ (MPC) is being used.

4.3.3 Kinematic Cut Study

We checked there are many background in χ_c region. And we figured out that some kinematic cuts to get rid of them by comparing single χ_c and embedded χ_c simulation.

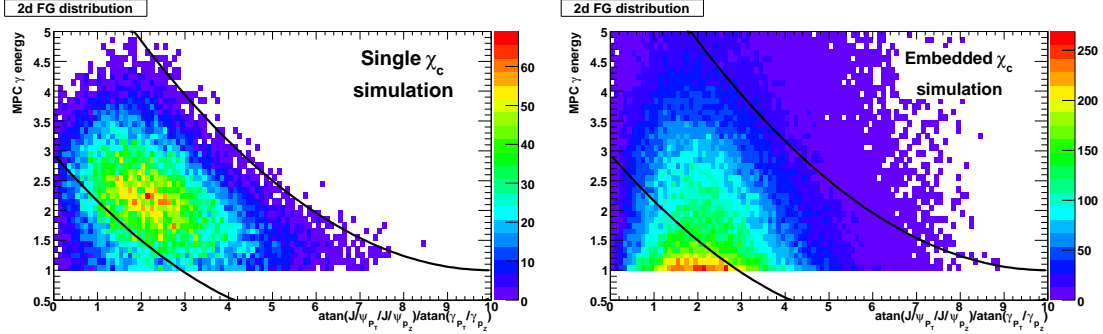


Figure 4.20: MPC photon energy vs. angle of J/ψ and photon of χ_c . Left plot is from single χ_c simulation and right plot is from embedded χ_c simulation. By cutting out of the line, many backgrounds are expected to cut out not loosing the signal much.

Tangetial angle cut

When we check MPC photon energy vs. angle of J/ψ and photon of the sigle χ_c simulation, almost MPC photon comes into the region which is defined as

$$E < 0.06 * (A - 7) * (A - 7), \quad (4.5)$$

for lower limit and

$$E > 0.06 * (A - 10) * (A - 10) + 1, \quad (4.6)$$

for upper limit. And Here, E is MPC deposited photon energy and A is defined as

$$A = \text{atan}(J/\psi_{P_T}/J/\psi_{P_Z})/\text{atan}(\gamma_{P_T}/\gamma_{P_Z}) \quad (4.7)$$

Fig. 4.20 shows the plots for single χ_c and embedded χ_c

Photon energy-rapidity cut

Fig. 4.21 shows the correlation of MPC photon energy vs. J/ψ rapidity. So we could also make the cuts from this distribution.

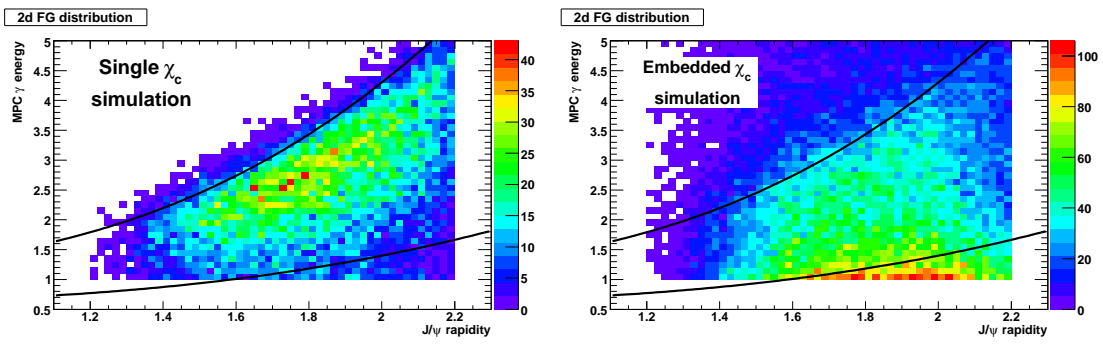


Figure 4.21: MPC photon energy vs. rapidity of J/ψ . Left plot is from single χ_c simulation and right plot is from embedded χ_c simulation. By cutting out of the line, many backgrounds are expected to cut out not loosing the signal much.

Fit parameters	Settings
p_0 (Total yield of χ_{c1}) and χ_{c2} p_1 (Peak position of χ_{c1}) p_2 (Peak width of χ_{c1}) p_3 (Relative ratio of χ_{c1} and χ_{c2}) p_4 (Peak position of χ_{c2}) p_5 (Peak width of χ_{c2})	free parameter limited by $\pm 2\%$ of the value of the embedded simulations fixed by the value of the embedded simulations fixed by 0.5 limited by $\pm 2\%$ of the value of the embedded simulations fixed by the value of the embedded simulations

Table 4.7: Fitting parameters for χ_c fitting.

4.4 Fitting real data

4.4.1 Fitting parameters and options

After subtracting combinatorial background as in Section 4.2, the signal is fit by two gaussians of which values are taken from the embedding simulation. Two gaussians correspond to the χ_{c1} and χ_{c2} , respectively. And the peak positions are limited by $\pm 2\%$ variation of the value of the embedded simulations. And the widths are fixed by the value of the embedded simulations and the widths of ± 10 MeV are assigned for the systematic uncertainties. The fitting function is defined as

$$F(x) = p_0 \times (p_3 \exp(-0.5 \times A \times A) + (1 - p_3) \exp(-0.5 \times B \times B)), \quad (4.8)$$

where $A = (x - p_1)/p_2$, $B = (x - p_4)/p_5$, $x = \text{mass}$. So one can change the ratio of χ_{c1} and χ_{c2} by the p_3 . Parameter settings are summarized in Table 4.7.

4.4.2 Fitting Run6pp and Run8dAu

Figure 4.22 and Figure 4.23 show the fitting results of Run6pp and Run8dAu dataset after subtracting the scaled mixed background.

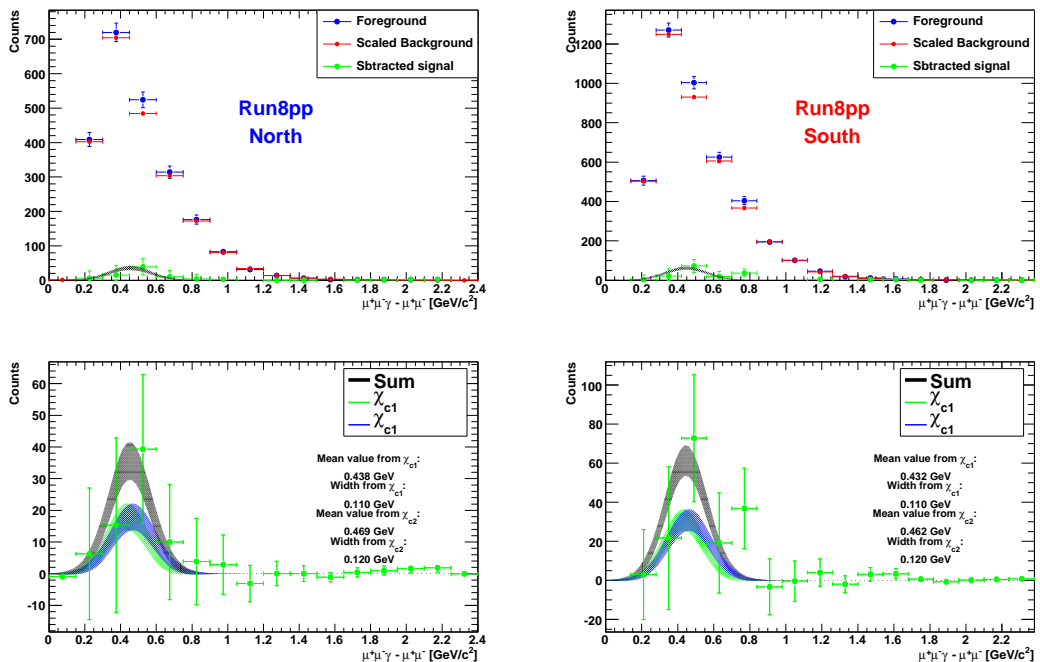


Figure 4.22: Plots are for Run8pp North and South arm. Left plot is for North arm and right plot is for South arm. Data is fit by the Gaussian function whose shape is taken from the embedding simulation.

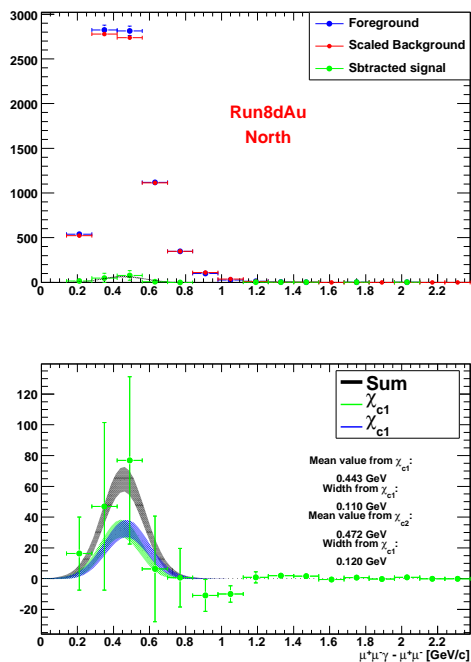


Figure 4.23: Plot is for Run8dAu North arm. As like pp data fitting, it is fit by the Gaussian function whose shape is taken from the embedding simulation.

	Run8pp North	Run8pp South	Run8dAu North
Normalization method	Sum of χ_{c1} and χ_{c2} (raw integral)	Sum of χ_{c1} and χ_{c2} (raw integral)	Sum of χ_{c1} and χ_{c2} (raw integral)
Likesign correlation Mass window1 (0.9-2.5 GeV)	69.14 29.47	127.62 44.76	134.32 325.93
RMS	57 %	65 %	143 %

Table 4.8: Yield variation for the Normalization method

4.5 Systematic uncertainties

Since Υ signal is not as big as the J/ψ , the biggest part of the uncertainty is from the statistical uncertainty. Besides the statistical error, we estimate the systematic uncertainties as described in the following.

4.5.1 determining of the Normalization

The normalization scale factor is taken from the likesign correlation. But another methods for normalization are assigned for uncertainty. Table 4.8 shows the uncertainties from the normalization.

4.5.2 Embedding efficiency

Yields from embedding simulation are changed by the range of normalization. Table 4.9 has the values for the normalization ranges.

4.5.3 MPC photon energy cut

Normal value of the photon energy cut is 1.3 GeV for all data set. Table 4.10, 4.12 and ?? show the uncertainties for pp North, pp South and dAu North arm, respectively.

Normalization method	Run8pp North	Run8pp South	Run8dAu North
	<i>Accep. × Effi.</i> (%)	<i>Accep. × Effi.</i> (%)	<i>Accep. × Effi.</i> (%)
Mass window1 (0.9-2.5 GeV)	1.27	2.49	0.31
Mass window2 (0.8-2.5 GeV)	1.19	2.34	0.39
Mass window3 (1.0-2.5 GeV)	1.29	2.62	0.38
RMS	5 %	6 %	24 %

Table 4.9: Embedding efficiency calculation along the normalization mass window.

MPC photon ennergy level (GeV)	Sum of χ_{c1} and χ_{c2} (raw integral)	Acceptance× efficiency %	χ_c yield / N_{BBC}
1.3	69.14	1.27	1.04e-06
1.0	74.54	1.51	0.94e-06
1.1	93.7385	1.42	1.26e-06
1.2	78.49	1.35	1.11e-06
1.4	95.6919	1.22	1.49e-06
RMS			26 %

Table 4.10: Systematic uncertainty table for χ_c photon energy level. 1.3 GeV is the norminal setting. This table is for Run8pp North arm.

MPC photon ennergy level (GeV)	Sum of χ_{c1} and χ_{c2} (raw integral)	Acceptance× efficiency %	χ_c yield / N_{BBC}
1.3	127.62	2.49	0.98e-06
1.0	129.47	3.00	0.82e-06
1.1	112.84	2.81	0.77e-06
1.2	89.1636	2.65	0.64e-06
1.4	121.128	2.34	0.99e-06
RMS			22 %

Table 4.11: Systematic uncertainty table for χ_c photon energy level. 1.3 GeV is the norminal setting. This table is for Run8pp South arm.

MPC photon ennergy level (GeV)	Sum of χ_{c1} and χ_{c2} (raw integral)	Acceptance× efficiency %	χ_c yield / N_{BBC}
1.3	134.318	0.31	8.18e-06
1.0	131.759	0.33	7.53e-06
1.1	96.9983	0.33	5.55e-06
1.2	54.9213	0.32	3.24e-06
1.4	108.219	0.30	6.81e-06
RMS			35 %

Table 4.12: Systematic uncertainty table for χ_c photon energy level. 1.3 GeV is the norminal setting. This table is for Run8dAu North arm.

Peak widths of χ_{c1} and χ_{c2} (χ_{c1} , χ_{c2})	χ_{c1} (raw integral)	χ_{c2} (raw integral)	Sum of χ_{c1} and χ_{c2} (raw integral)	χ^2/NDF
0.11, 0.12	33.01	36.01	69.03	1.68
0.10, 0.11	32.56	35.81	68.37	1.44
0.12, 0.13	32.22	34.90	67.12	2.13
RMS			2.0 %	

Table 4.13: Systematic uncertainty table for χ_c peak width. 110 MeV for χ_{c1} and 120 MeV for χ_{c2} are the norminal setting. This table is for Run8pp North arm.

4.5.4 Fitting Function

We are using two Gaussians to fit the χ_{c1} and χ_{c2} . But the exact ratio of two and the width of the peaks are not known. So we need to assign the systematic uncertainties from the variations of the parameters.

χ_c Peak width

Peak widths of χ_{c1} and χ_{c2} are assumed as 110 MeV and 120 MeV from the embedding simulation. The variation of ± 10 MeV are tried to estimate the systematic uncertainties like Table 4.13, 4.14 and 4.15.

The ratio of χ_{c1} and χ_{c2}

The ratio of χ_{c1} and χ_{c2} is assumed as 50% : 50%. But, exact ratio of two could not be measured because of pure resolution. Table 4.16, 4.17 and ?? are showing the variation of the ratio and its uncertainties.

MPC acceptance

χ_c kinematic properties are not known exactly. And MPC acceptance is varying when the χ_c kinematics are varying. MPC acceptance has uncertainties as the Table chickinematic. And the norminal value for MPC geometrical acceptance is set as 4.30 %.

Peak widths of χ_{c1} and χ_{c2} (χ_{c1} , χ_{c2})	χ_{c1} (raw integral)	χ_{c2} (raw integral)	Sum of χ_{c1} and χ_{c2} (raw integral)	χ^2/NDF
0.11, 0.12	61.14	66.70	127.84	0.46
0.10, 0.11	60.40	66.43	126.83	0.45
0.12, 0.13	59.76	64.74	124.50	0.47
RMS			1.9 %	

Table 4.14: Systematic uncertainty table for χ_c peak width. 110 MeV for χ_{c1} and 120 MeV for χ_{c2} are the norminal setting. This table is for Run8pp South arm.

Peak widths of χ_{c1} and χ_{c2} (χ_{c1} , χ_{c2})	χ_{c1} (raw integral)	χ_{c2} (raw integral)	Sum of χ_{c1} and χ_{c2} (raw integral)	χ^2/NDF
0.11, 0.12	84.59	92.28	176.87	1.45
0.10, 0.11	87.04	95.75	182.79	1.44
0.12, 0.13	77.57	84.03	161.61	1.48
RMS			6.5 %	

Table 4.15: Systematic uncertainty table for χ_c peak width. 110 MeV for χ_{c1} and 120 MeV for χ_{c2} are the norminal setting. This table is for Run8dAu North arm.

Ratio of χ_{c1} and χ_{c2} ($\chi_{c1} : \chi_{c2}$)	χ_{c1} (raw integral)	χ_{c2} (raw integral)	Sum of χ_{c1} and χ_{c2} (raw integral)	χ^2/NDF
1 : 0	65.32	0	65.32	1.68
0.9 : 0.1	59.06	7.16	66.22	1.68
0.8 : 0.2	52.67	14.36	67.04	1.68
0.7 : 0.3	46.18	21.59	67.77	1.68
0.6 : 0.4	39.62	28.82	68.44	1.68
0.5 : 0.5	33.01	36.01	69.03	1.68
0.4 : 0.6	26.38	43.16	69.54	1.68
0.3 : 0.7	19.74	50.25	69.99	1.68
0.2 : 0.8	13.12	57.25	70.37	1.67
0.1 : 0.9	6.53	64.14	70.67	1.67
0 : 1	0	70.92	70.92	1.67
RMS			3.8 %	

Table 4.16: Systematic uncertainty table for χ_c ratios. The ratio of 50 % : 50 % of χ_{c1} and χ_{c2} is norminal setting. This table is for Run8pp North arm.

Ratio of χ_{c1} and χ_{c2} ($\chi_{c1} : \chi_{c2}$)	χ_{c1} (raw integral)	χ_{c2} (raw integral)	Sum of χ_{c1} and χ_{c2} (raw integral)	χ^2/NDF
1 : 0	121.21	0	121.21	0.48
0.9 : 0.1	109.54	13.28	122.81	0.48
0.8 : 0.2	97.65	26.63	124.28	0.47
0.7 : 0.3	85.59	40.01	125.60	0.47
0.6 : 0.4	73.41	53.38	126.79	0.46
0.5 : 0.5	61.14	66.70	127.84	0.46
0.4 : 0.6	48.84	79.92	128.76	0.45
0.3 : 0.7	36.54	93.01	129.55	0.45
0.2 : 0.8	24.28	105.94	130.22	0.44
0.1 : 0.9	12.09	118.68	130.77	0.44
0 : 1	0	131.20	131.20	0.44
RMS			2.7 %	

Table 4.17: Systematic uncertainty table for χ_c ratios. The ratio of 50 % : 50 % of χ_{c1} and χ_{c2} is norminal setting. This table is for Run8pp South arm.

Ratio of χ_{c1} and χ_{c2} ($\chi_{c1} : \chi_{c2}$)	χ_{c1} (raw integral)	χ_{c2} (raw integral)	Sum of χ_{c1} and χ_{c2} (raw integral)	χ^2/NDF
1 : 0	179.29	0	179.29	1.44
0.9 : 0.1	159.89	19.38	179.27	1.44
0.8 : 0.2	140.66	38.36	179.02	1.44
0.7 : 0.3	121.66	56.88	178.53	1.44
0.6 : 0.4	102.96	74.87	177.81	1.44
0.5 : 0.5	84.59	92.28	176.87	1.45
0.4 : 0.6	66.66	109.08	175.74	1.45
0.3 : 0.7	49.20	125.23	174.43	1.45
0.2 : 0.8	32.29	140.89	173.17	1.46
0.1 : 0.9	15.88	155.95	171.83	1.46
0 : 1	0	169.99	169.99	1.46
RMS			1.9 %	

Table 4.18: Systematic uncertainty table for χ_c ratios. The ratio of 50 % : 50 % of χ_{c1} and χ_{c2} is norminal setting. This table is for Run8dAu North arm.

χ_c kinematics	Rapidity (flat)	Rapidity (Gaussian) ($\sigma : 1.5$)	Rapidity (Gaussian) ($\sigma : 1.9$)	Rapidity (Gaussian) ($\sigma : 2.3$)
$p_T(\exp(-x))$	$4.49 \pm 0.09 \%$	$4.04 \pm 0.09 \%$	$4.18 \pm 0.09 \%$	$4.34 \pm 0.09 \%$
$p_T(\exp(-2x))$	$4.68 \pm 0.09 \%$	$4.07 \pm 0.09 \%$	$4.27 \pm 0.09 \%$	$4.51 \pm 0.09 \%$
$p_T(\exp(-3x))$	$4.83 \pm 0.10 \%$	$4.30 \pm 0.09 \%$	$4.36 \pm 0.09 \%$	$4.58 \pm 0.10 \%$
RMS			1.9 %	

Table 4.19: Systematic uncertainty table from the MPC geometrical acceptance.

4.5.5 MUID, MUTR, BBC, Acceptance \times Efficiency.

We assign 4 % uncertainty due to MUID efficiency variation and 2 % due to MUTR efficiency variation similar to other muon arm analyses. For BBC efficiency, 10 % uncertainty is assigned for pp and 5.65 % for dAu as AN.396 calculated. We haven't studied the systematic uncertainty for acceptance \times efficiency, but the contribution from this is expected to be negligible compared to other sources since we are using only two rapidity bins, one for south arm and one for north arm. Thus we are not counting the uncertainty of acceptance \times efficiency for this analysis.

4.6 Summary of the systematic uncertainties

Total systematic uncertainties are summarized in Table 4.20. The table includes the statistical uncertainty also.

Types of Uncertainty	Run8pp North rms	Run8pp South rms	Run8dAu North rms
χ_c peak width	2 %	1.9 %	6.5 %
χ_c ratio	3.8 %	2.7 %	1.9 %
MPC energy cut	26 %	22 %	35 %
Muid efficiency	4 %	4 %	4 %
Mutr efficiency	2 %	2 %	2 %
Acc. \times Effi.	5 %	6 %	24 %
Normalization method	57 %	65 %	143 %
Geometrical MPC acceptance	6.3 %	6.3 %	6.3 %
Systematic Total (Quadratic sum)	63 %	69 %	150 %
BBC(Global)	10 %	10 %	5.65 %
Statistical uncertainty	58 %	43 %	63 %

Table 4.20: Total systematic and statistical uncertainty summary table.

Dataset	Lumi.	Signal	Acc. \times Eff.	MPC acceptance	dN/dy	$\text{BR}^* d\sigma_{J/\psi} / dy$ $1.2 < y < 2.2$
Run8pp North	4.24 pb^{-1}	69.14 ± 40.15 ± 43.56	1.27 %	4.3 %	$9.0 \text{e-}07 \pm 5.2 \text{e-}7$ $\pm 5.7 \text{e-}7$	$37.9 \pm 22.0 \text{ nb}$ $\pm 23.9 \text{ nb}$
Run8pp South	4.24 pb^{-1}	127.62 ± 54.78 ± 88.06	2.49 %	4.3 %	$8.5 \text{e-}7 \pm 3.6 \text{e-}7$ $\pm 5.9 \text{e-}7$	$35.7 \pm 15.3 \text{ nb}$ $\pm 24.6 \text{ nb}$
Run8dAu North	67.2 nb^{-1}	134.32 ± 84.92 ± 201.48	0.31 %	4.3 %	$7.1 \text{e-}06 \pm 4.5 \text{e-}06$ $\pm 1.1 \text{e-}5$	$16.0 \pm 10.1 \text{ ub}$ $\pm 24 \text{ ub}$

Table 4.21: χ_c decay J/ψ invariant yield and $\text{BR} \times$ cross section of Run8pp and Run8dAu dataset.

4.7 Results

4.7.1 Invariant yield and cross section

We calculate invariant yield and cross section using the equation below

$$B \frac{dN_{\chi_c}}{dy} = \frac{1}{\Delta y} \frac{N_{\chi_c}}{A \epsilon_{\chi_c} \epsilon_{\chi_c}^{BBC}} / \frac{N_{MB}^{BBC}}{\epsilon_{MB}^{BBC}}, \quad (4.9)$$

$$B \frac{d\sigma_{\chi_c}}{dy} = B \frac{dN_{dy}}{dy} \sigma_{Total} \quad (4.10)$$

Table 4.21 includes the invariant yield and $\text{BR} \times$ cross section of Run6pp and Run8dAu dataset. To get the σ_{χ_c} , the branching ratio of $\chi_c \rightarrow \mu^+ \mu^- \gamma$ is obtained from the PDG' 10 on the webpage at

<http://pdg.lbl.gov/>

The branching ratio is summarized in Table 4.22. With the branching ratio of Table 4.22, χ_c cross section at forward rapidity is caculated as

$$BR(J/\psi \rightarrow \mu^+ \mu^-) * \sigma_{\chi_c} = \sigma_{J/\psi} / BR(\chi_c \rightarrow J/\psi, \gamma) \quad (4.11)$$

BR ratios	χ_{c0} (3.41 GeV)	χ_{c1} (3.51 GeV)	χ_{c2} (3.56 GeV)	J/ψ (3.10 GeV)
$\chi_c \rightarrow J/\psi, \gamma$ $J/\psi \rightarrow \mu^+ \mu^-$	1.16 %	34.4 %	19.5 %	5.93 %

Table 4.22: $\chi_c \rightarrow \mu^+ \mu^- \gamma$ branching ratios. Values are obtained from PDG' 10

Data set	rapidity	$BR(J/\psi \rightarrow \mu^+ \mu^-) \times \sigma_{\chi_c} / dy$
Run8pp South	[-2.2,-1.2]	$107.5 \pm 46.2(\text{stat.}) \pm 33.3(\text{syst.}) \text{ nb}$
Run8pp North	[1.2,2.2]	$114.2 \pm 66.2(\text{stat.}) \pm 42.3(\text{syst.}) \text{ nb}$
Run8dAu North	[1.2,2.2]	$64.3 \pm 40.5(\text{stat.}) \pm 96.4(\text{syst.}) \text{ ub}$

Table 4.23: Extrapolated χ_c cross sections considering the effective branching ratios.

Table 4.23 has the $BR(J/\psi \rightarrow \mu^+ \mu^-) \times \sigma_{\chi_c} / dy$ for each data set. Figure 4.24 show the rapidity distribution of χ_c . R_{χ_c} , the ratio of χ_c decay into J/ψ over inclusive J/ψ is defined as

$$R_{\chi_c} = \frac{1}{\sigma_{J/\psi}} \sum_{J=0}^2 BR(\chi_{cJ} \rightarrow J/\psi, \gamma) \sigma_{\chi_{cJ}}, \quad (4.12)$$

where BR and σ are the branching ratio and cross section, respectively. The branching ratio of χ_{c0} is small and its contribution is usually neglected. Currently R_{χ_c} value has $1.3 \pm 0.7(\text{stat.}) \pm 0.8(\text{syst.})$. And the value has too big uncertainties. Future PHENIX data is expected to have more than 2 times integrated luminosity than this run. So with the increased luminosities, the uncertainty is expected to be lessened.

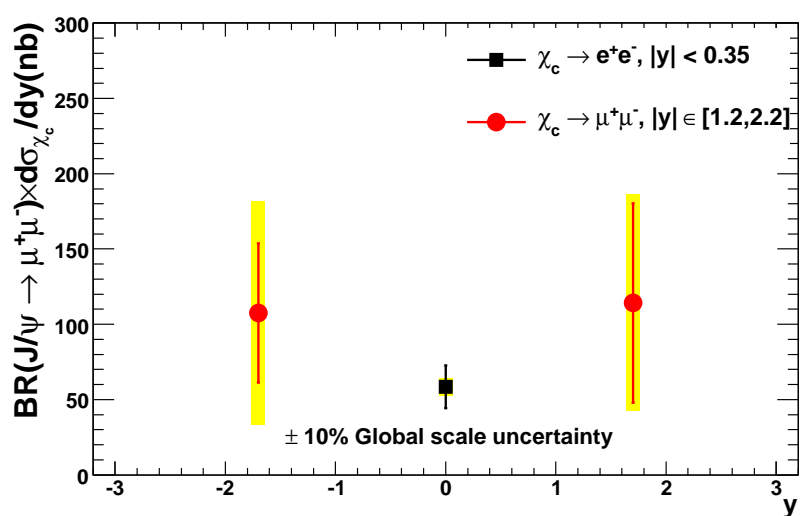


Figure 4.24: $\text{BR} \times \chi_c$ cross section of Run8pp. Backward data point is from Run8pp South arm and forward data point is from Run8pp South arm

Chapter 5

Conclusions

In this thesis, σ_{Υ} , R_{dA}^{Υ} , σ_{χ_c} and R_{χ_c} are investigated at forward rapidities in $\sqrt{s_{NN}} = 200$ GeV $p + p$ and $d + \text{Au}$ collisions. Combinatorial background is estimated by the event mixing. Especially, to extract Υ signal, another physical sources of Drell Yan process, open bottom correlation and open charm correlation are simulated and estimated. To estimate those contribution, they are generated by amount of their cross sections and integrated luminosities. And the estimations are used to fit the real data and get Υ signal. After preliminary result, NLO Drell Yan process calculation is got from Ivan Vitev. With the updates, more precise measurement is accomplished since the uncertainty by the LO pythia estimation has lessened.

The rapidity distribution of σ_{Υ} s of $p + p$ collision is compared to the theoretical estimation of Color Evaporation Model (CEM) with the preliminary σ^{Υ} at mid rapidity. When we scale down the CEM model calculation by a factor of 2, the model matches well to the data points. The agreement of the distribution shape with the CEM model estimation provides us a good constrain to understand the production mechanism of Υ .

In $d + \text{Au}$ collision, the Υ nuclear modification factor, R_{dA}^{Υ} is measured at forward rapidity in PHENIX experiment at first. Forward rapidity is estimated to have $< x >$, which is the momentum fraction of Au nucleus, ~ 0.01 . So that region corresponds to the shadowing region. And the R_{dA}^{Υ} shows the suppression in this region. Since $\sim 90\%$ of Υ is produced by the gluon fusion process, the shadowing of gluon can explain the Υ suppression. And another final state effect can suppress the Υ production. Besides this investigation, another Υ nuclear modification factor measurements are ongoing in $\sqrt{s_{NN}} = 200$ GeV. For example, STAR experiment is showing preliminary $R_{dA}^{\Upsilon} \sim 0.98$ at mid rapidity. PHENIX also has the preliminary $R_{AA}^{\Upsilon} < 0.64$ with 90 % confidence level at mid rapidity. With these measurement finalized, we expect to provide good constrain for understanding of matter created in the nuclear collision.

For the χ_c analysis, MPCs are used to detect χ_c decay photon as well as the muon

arms. To extract χ_c , three particle correlation of dimuon and photon is done and the mass difference between three particle correlation and dimuon is used to lessen the uncertainty from dimuon mass resolution. And the combinatorial background is estimated by the event mixing. Currently, σ_{χ_c} and R_{χ_c} are extracted but have large uncertainties due to the small MPC acceptance and statistical limitation. Another PHENIX R_{χ_c} measurement at mid rapidity shows < 0.42 with 90 % confidence level and the world average is ~ 0.3 for various data set and beam energy but has big fluctuation and large uncertainties. With the future PHENIX data taking, which has more integrated luminosity and improved resolution, more precise χ_c measurement will be possible so the uncertainty will lessen. That measurement will be important to understand the J/ψ production mechanism and decouple the cold nuclear matter effect and the thermal state of QGP.

Bibliography

- [1] F. Karsch, *Lattice QCD at high temperature and density*, Lecture Notes in Physics **583** (2002)209, Springer Germany.
- [2] F. Karsch, *arXiv: 0711.0656 [hep-lat]* (2007).
- [3] R.J. Glauber, in: *Lectures in theoretical physics*, ed. W.E. Brittin et al., (Interscience Publishers, New York, 1959) **vol. I**, p. 315.
- [4] T. Hashimoto, O. Miyamura, K. Hirose, and T. Kanki. *Phys. Rev. Lett.* **57**, 2123 (1986).
- [5] Jean-Yves Ollitrault *Phys. Rev.*, **D46**, 229-245 (1992).
- [6] A. Adare et al., *Phys. Rev. Lett.*, **103**, 082002 (2009).
- [7] K. Adcox et al.,(PHENIX) *Phys. Rev. Lett.* **88**, 022301 (2001).
- [8] T. Matsui and H. Satz. *Phys. Lett.*, **B178**:416, (1986).
- [9] E. Eichten et al., *Phys. Rev.*, **D21**:203, (1980).
- [10] H. Satz. *Rep. Prog. Phys.*, **63**:1511-1574, (2000).
- [11] M. J. Leitch. *Eur. Phys. J.*, **A19**:129, (2003).
- [12] D. Antreasyn et al. *Phys. Rev.*, **D19**:764, (1979).
- [13] K. Adcox et al. *Nucl.Phys.*, **A757**:184-283, (2005).
- [14] A. Adare et al., *Phys. Rev. C* **80**, 024908 (2009).
- [15] S. S. Adler et al. *Phys. Rev. Lett.*, **91**:172301, (2003).
- [16] J. Adams et al. *Phys. Rev. Lett.*, **91**:172304, (2003).
- [17] S. S. Adler et al. *Phys. Rev. Lett.*, **91**:182301, (2003).

- [18] J. Adams et al. *Phys. Rev.*, **C72**:014904, (2005).
- [19] P. Huovunen et al. *Phys. Lett.*, **B503**:58, (2001).
- [20] A. Adare et al. *Phys. Rev. Lett.*, **98**:162301, (2007).
- [21] J. Adams et al. *Phys. Rev. Lett.*, **92**:052302, (2004).
- [22] J. Adams et al. *Phys. Rev. Lett.*, **95**:122301, (2005).
- [23] A. Adare et al., *Phys. Rev. D* **81**, 012002 (2010).
- [24] R. L. Thews, M. Schroedter and J. Rafelski, *Phys. Rev.* **C63**, 054905 (2001).
- [25] A. Andronic, P. Braun-Munzinger, K. Redlich and J. Stachel, *Phys. Lett.* **B571**, 36-44 (2003).
- [26] M. C. Abreu et al. *Phys. Lett.*, **B477**:28-36, (2000).
- [27] Carlos Lourenco et al., *JHEP* **0902**:014,(2009).
- [28] A. Adare et al., *Phys. Rev. Lett.*, **103**, 012003 (2009).
- [29] N. Armesto, *J.Phys.* **G32**:R367-R394, (2006).
- [30] S. S. Adler et al. *Phys. Rev. Lett.* **96**, 012304(2006).
- [31] K. J. Eskola, H. Paukkunen, C. A. Salgado, *EPS09 - a New Generation of NLO and LO Nuclear Parton Distribution Functions*, *JHEP* **0904**:065, (2009).
- [32] M. Hirai, S. Kumano and T. H. Nagai, *arXiv*: **0709.3038** [hep-ph]
- [33] D. de Florian and R. Sassot, *Phys. Rev. D* **69** (2004) 074028 [arXiv:hep-ph/0311227].
- [34] K. J. Eskola, V. J. Kolhinen, and R. Vogt, *Nucl. Phys.* **A696**, 729 (2001).
- [35] D. deFlorian and R. Sassot, *Phys. Rev. D* **69**, 074028 (2004).
- [36] A. Adare et al., *Phys. Rev. D* **79**, 012003 (2009).
- [37] A. Adare et al.(PHENIX), *Phys. Rev.*, **C77**, 024912, (2008).
- [38] Jianwei Qiu et al., *Phys.Rev.Lett.* **88** 232301, (2002).
- [39] B.Z. Kopeliovich., *arXiv:1008.4272*, (2010).
- [40] A. Adare et al., *Phys. Rev. Lett.*, **101**, 162301 (2008).
- [41] R. Vogt, *Nucl. Phys.* **A 700**, 539, (2002).

- [42] Y. Maezawa et al., *PoS LAT2006*, 141, (2006).
- [43] B. Povh et al., *Phys. Rev. Lett.* **58**, 1612, (1987).
- [44] M.J. Leitch et al., *Phys. Rev. Lett.* **84**, 3256, (2000).
- [45] R. Vogt, *Acta. Phys. Hung.* **A 25**, 97, (2006).
- [46] J.W. Cronin et al., *Phys. Rev. D* **11**, 3105, (1975).
- [47] H. Satz, *Nucl.Phys.* **A783**:249-260, (2007).
- [48] F. Karsch et al., *Z. Phys. C* **37**, 617, (1988).
- [49] W.M. Yao et al., *Journal of Physics G* **33**, 1, (2006).
- [50] M. Harrison et al., *Nuclear Instruments and Methods in Physics Research A* **499 (2-3)**: 235(2003).
- [51] M. Harrison et al., *Annual Review of Nuclear and Particle Science* **52**: 425(2002).
- [52] E.D. Courant, *Annual Review of Nuclear and Particle Science* **53**: 1.(2003)
- [53] M. Riordan et al., *Scientific American* 10.1038/scientificamerican0506-34A (2006).
- [54] S. H. Aronson et al., *Nucl. Instrum. Meth.*, **A499** 480-488,(2003).
- [55] K. Adcox et al., *Nucl. Instrum. Meth.*, **A499** 489-507, (2003).
- [56] M. Aizawa et al., *Nucl. Instrum. Meth.*, **A499** 508-520, (2003).
- [57] L. Aphecetche et al., *Nucl. Instrum. Meth.*, **A499** 521-536, (2003).
- [58] A. Bazilevsky et al., *PHENIX Technical Note*: **386**.
- [59] G. David et al., *IEEE Trans. Nucl. Sci.*, **47** 1982-1986, (2000).
- [60] S. H. Aronson et al., *Nucl. Instr. and Meth. A*, **499** :593-602, (2003).
- [61] C. Amsler et al., Particle data group. *Phys. Lett.*, **B667**:1, (2008).
- [62] Melynda Brooks et al., Run 5 p-p J/ψ and Υ dimuon analysis, PHENIX AN 401, 2005.
- [63] L.A. Linden Levy et al., Nuclear modification factor for $J/\psi \rightarrow \mu^+\mu^-$ using Run-8 d+Au and Run-6 p+p at $\sqrt{S_{NN}} = 200$ GeV, PHENIX AN 739, 2008.
- [64] L.A. Linden Levy et al., $J/\psi \rightarrow \mu^+\mu^-$ Invariant yields using Run-6 p+p and Run-8 d+Au $\sqrt{S_{NN}} = 200$ GeV, PHENIX AN 794, 2009.

- [65] J.M. Burward-Hoy et al., Addendum to PPG038 Muon Analysis Note - Final run 3 J/ψ dimuon analysis, PHENIX AN 396, 2005.
- [66] J.M. Burward-Hoy et al., Final run 3 J/ψ dimuon analysis, PHENIX AN 393, 2005.
- [67] K.Lee et al., Quarkonium Production in p+p and d+Au collisions at $\sqrt{S}=200$ GeV with Run6 and Run8 data PHENIX AN 805, 2009.
- [68] The CDF Collaboration, Published Proceedings Les Rencontres de Physique de la Vallee d'Aoste, La Thuile, Italy, March 3-9, 1996. FERMILAB-CONF-96/110-E.
- [69] A. Adare et al., *Phys. Rev. Lett.* **105**, 142301 (2010).
- [70] A. Adare et al., *Phys. Rev. Lett.* **105**, 062301 (2010).
- [71] A. Adare et al., *Phys. Rev. C* **82**, 011902 (2010).
- [72] A. Adare et al., *Phys. Rev. D* **82**, 012001 (2010).
- [73] A. Adare et al., *Phys. Rev. Lett.* **104**, 252301 (2010).

Appendix A

Run8dAu QA

A.1 QA table

Zero Field Runs	246607 247219 249155 250709 250710 251493 252213 252778 252779 253576
BBC off (temperature sensor failure)	253542 253567
MuID HV Bad South	247054 247230 247609 248159 250847 252518 258949
MuID HV Bad North	247609 248159 248353 252517
MuTr HV Bad South	246212 252928 253156
Mutr HV Bad North	246212 246595 246606 246612 247387 257411 258950 259489
MuID South HV MF down	250849 250862 250864 250865 250866 250873 250875 250877 250878 250879 250883 250885 250886 250887 252514 252517 252520 252521 252524 252525 252526 252614 252616 252618 252622 252623 252625 252626 252632 252633 252634 252650 252654 252655 252656 252658 252660 252661
MuTr North LV failure	249612 250280 250281 250282 250306 250307 250308 250309 250310 250313 250318 250319 250321 250322 250324 250325 250327 250328 250336 250482 250483 250484
Runs with no dimuons in the MWGs South	248312 248353 250681 252517

Table A.1: QA of Run8dAu done by Mike Leitch (Part1)

Runs with no dimuons in the MWGs North	248312 250280 250281 250307 250308 250309 250310 250313 250319 250321 250322 250324 250325 250327 250328 250336 250482 250483 250484
Dead HV channels	246285 246296 246487 246502 246511 246593 246612 247174 247177 247183 247236 247387 247402 247418 247952 248051 248054 248784 249047 249071 249115 249127 249252 249485 249840 249846 249869 250005 250009 250094 250155 250170 250206 250210 250596 250680 250886 251333 251953 251971 252105 252119 252124 252148 252224 252525 252626 252654 252786 252928 252939 252952 252962 252980 253145 253156 253435 253462

Table A.2: QA of Run8dAu done by Mike Leitch (Part 2)